4-3-2008

Surface and Interface Magnetism in Nanostructures and Thin Films

Natalie A. Frey
University of South Florida

Surface and Interface Magnetism in Nanostructures and Thin Films

by

Natalie A. Frey

A dissertation submitted in partial fulfillment
of the requirements for the degree of
Doctor of Philosophy
Department of Physics
College of Arts and Sciences
University of South Florida

Major Professor: Hariharan Srikanth, Ph.D.
Wei Chen, Ph.D.
Arun Kumar, Ph.D.
Shyam Mohapatra, Ph.D.
David Rabson, Ph.D.
Sarath Witanachchi, Ph.D.

Date of Approval:
April 3, 2008

Keywords: transverse susceptibility, magnetic nanoparticles, multilayer thin films,
exchange bias, magnetic anistropy

DEDICATION

To my husband, Dean.

Thank you for being by my side no matter where life takes us.

ACKNOWLEDGMENTS

First I would like to thank Dr. Hariharan Srikanth for being my advisor and friend for the past six years. I am extremely grateful for the unwavering support and patience of my parents, family, friends, and of course my loving husband. Thank you to my IGERT co-advisors Dr. Shyam Mohapatra and Dr. Arun Kumar for working with me on this project the last two years, and also to my other committee members Dr. Wei Chen, Dr. David Rabson, and Dr. Sarath Witanachchi. Thank you to Dr. Vinay Gupta for taking time to chair my dissertation defense. I would like to thank Dr. Nancy Dudney of Oak Ridge National Laboratory and Dr. Harry Edelman of Seagate Technology for hosting me on my two summer internships and continuing to be influential to me. Thank you to all my co-workers and lab mates over the years, notably James Gass, Dr. Jeff Sanders, Dr. Pankaj Poddar, Dr. Ranko Heindl, Marienette Morales Vega, Melody Miner, and Dr. Manh-Huong Phan. A special thanks to Dr. Srinath Sanyadanam whose guidance while a part of our lab has been invaluable to me. I also would like to acknowledge my collaborators, especially Dr. Arunava Gupta from the University of Alabama MINT Center and Dr. Shouheng Sun from Brown University for providing me with excellent samples to measure for this dissertation. Thank you to all the USF Physics Department staff for their help during my time as a graduate student. I am very grateful for a 2-year NSF-IGERT fellowship from the USF SKINS program through NSF IGERT Grant No. DGE-0221681, and in particular thank you to Mr. Bernard Batson for his help during my two years as an IGERT fellow.

TABLE OF CONTENTS

LIST OF TABLES

LIST OF FIGURES

LIST OF ABBREVIATIONS

AC	Alternating Current
Au	Gold
B	Magnetic Inductance
BaM	Barium-Iron-Oxide, Barium-(Hexa)-Ferrite, BaFe12O19
BSTO	Barium-Strontium-Titanate (Ba0.5Sr0.5TiO3)
DC	Direct Current
emu	Magnetic Moment Unit (Electromagnetic Unit)
Fe_3O_4	Magnetite
H	Magnetic Field
H_K	Anisotropy Field
H_C	Coercive Field (Coercivity)
J	Joule
K	Kelvin
M	DC-Magnetization
M_R	Remanent Magnetization
M_S	Saturation Magnetization
M-H	Magnetization vs. Applied Magnetic Field
Oe	Oersted
PPMS	Physical Properties Measurement System
RF	Radio-Frequency
s	second
SEM	Scanning Electron Microscope

T	Tesla
TEM	Transmission Electron Microscope
XRD	X-Ray Diffraction
TS	Transverse Susceptibility

SURFACE AND INTERFACE MAGNETISM IN NANOSTRUCTURES AND THIN FILMS

Natalie A. Frey

ABSTRACT

Nanostructured systems composed of two or more technologically important materials are useful for device applications and intriguing for the new fundamental physics they may display. Magnetism at the nanoscale is dominated by size and surface effects which combined with other media lead to new spin dynamics and interfacial coupling phenomena. These new properties may prove to be useful for optimizing sensors and devices, increasing storage density for magnetic media, as well as for biomedical applications such as drug delivery, MRI contrast enhancement, and hyperthermia treatment for cancer. In this project we have examined the surface and interface magnetism of composite nanoparticles and multilayer thin films by using conventional DC magnetization and AC susceptibility as well as transverse susceptibility, a method for directly probing the magnetic anisotropy of materials. Au and Fe_3O_4 synthesized together into three different nanoparticle configurations and ranging in size for 60 nm down to 9nm are used to study how the size, shape, and interfaces affect the most fundamental properties of magnetism in the Au-Fe_3O_4 system. The findings have revealed ways in which the magnetic properties can be enhanced by tuning these parameters. We have shown that by changing the configurations of the Au and Fe_3O_4 particles, exotic behavior can be observed such as a large increase in anisotropy field (H_K ranging from 435 Oe to 1650 Oe) and the presence of exchange bias. Multilayer thin films have been studied as well which combine the important classes of ferromagnetic and ferroelectric materials. In one case, barium hexaferrite/barium strontium titanate thin films, the anisotropic behavior of the ferromagnet is shown to change due to the introduction of

the secondary material. In the other example, CrO_2/Cr_2O_3 bilayers, exchange coupling is observed as Cr_2O_3 is an antiferromagnet as well as a ferroelectric. This coupling is manifest as a uniaxial anisotropy rather than the unidirectional anisotropy associated with exchange biased bilayers. Not only will such multifunctional structures will be useful for technological applications, but the materials properties and configurations can be chosen and tuned to further enhance the desired functional properties.

CHAPTER 1

INTRODUCTION

Nanostructured systems containing two or more technologically important materials, referred to as "multifunctional" materials, are becoming increasingly popular as the trend towards device and sensor miniaturization continues. Spatial constraints are prompting scientists and engineers to think creatively about bringing multifunctionality to new electronic components as well as to exploit the properties that occur as a consequence of the interfaces that are formed by the direct contact of different materials.

In magnetic materials, shrinking one or more dimensions to the nanoscale has profound implications. For nanoparticles with diameters too small to form magnetic domains, thermal fluctuations can lead to destabilization of the magnetic state. This has forced the hard drive industry to look at ways of increasing the magnetic anisotropy of small particles so that storage densities can continue to increase without compromising the stability of the media. The most straightforward method of increasing the magnetic anisotropy is to use materials with exceedingly high magnetocrystalline anisotropy such as the $L1_0$ phase of FePt. While progress in making monodisperse, small particles with uniform magnetic properties has been slow, people are turning to other methods of increasing anisotropy such as using exchange coupled nanostructures or capitalizing on shape and surface anisotropy.

While superparamagnetism has become a hinderance in the hard drive industry, biomedical engineers have embraced the notion of high-response, remanence-free particles for external manipulation after injection into the human body. Applications for such nanoparticles include targeted drug delivery, MRI contrast enhancement and localized heating for killing cancerous cells. For these applications, the size of the particle must coincide with the ability of certain cells to allow passage through the cell membrane. Since this size is dependent

upon the part of the body targeted, the ability to tune particle size is crucial. For some of these applications, notably hyperthermia, tuning the magnetic properties such as blocking temperature and frequency as well as coercivity in the ferromagnetic state becomes important as well. Providing better functionality through the use of a metal coating allows for a larger variety of molecules to be delivered to specific sites and can also minimize inter-particle interactions.

In magnetic nanoparticles, the ability to tune the anisotropy to meet the needs of vastly different applications is a challenge. In this dissertation, it is demonstrated that the same two materials, namely Au and Fe_3O_4, can be synthesized in different configurations to achieve a broad range of magnetic characteristics. Au-Fe_3O_4 in the core-shell configuration is extremely useful for biomedical applications because the Fe_3O_4 component can be manipulated by external magnetic fields and the Au surface can be used for the attachment of a vast array of biological molecules. Here, we show how the size of the particles can be manipulated to meet the requirements for biocompatibility while simultaneously optimizing the properties for certain biomedical applications. This can be done by making sure the competition between the anisotropy energy of the particle and the thermal energy necessary to demagnetize the particle strike a precarious balance which allows one to use the frequency of the magnetic field to switch between the magnetic states. We show how this maximizes the functionality of the particle for several applications including drug delivery and hyperthermia.

Furthermore, we demonstrate how simply changing the arrangement of the Au and the Fe_3O_4 can drastically alter the functionality of the particle and give rise to novel magnetic behavior. When the Fe_3O_4 is grown on the surface of an Au particle, the result is a nanostructure made of two particles sharing one interface ("dumbbell" particle). The composite particle then has greater versatility as the Fe_3O_4 can still be manipulated externally, but now both surfaces are available for functionalization. When the Fe_3O_4 is allowed to grow on multiple facets of the Au particles via slightly different synthesis conditions, a different type of composite particle is formed ("flower" particle). This Fe_3O_4 cluster-type

geometry results in surprising magnetic properties including exchange bias, training effect, and anomalous relaxation behavior. Our studies point to complex and competing interactions between the Fe_3O_4 particles sharing the same Au particle. The significant increase in anisotropy achievable in these particles indicates that a cluster-type geometry of easily synthesized nanoparticles could be a viable path to beating the superparamagnetic limit in magnetic recording.

In magnetic thin film systems, as in nanoparticles, the magnetic properties are greatly influenced by surface and interface effects. The differences in magnetism between thin films and bulk materials are consequences of film thickness, substrate material and interfaces with other layers if the system is a bilayer or multilayer. In each of these cases, the anisotropy of the film is affected by interfacial strain as well as exchange coupling to the other materials present. Using exchange coupling to pin magnetic layers or to increase the coercivity has had a large impact on device applications from magnetic read and write heads to spin valves and sensors. Combining the effects of exchange coupling with magnetoelectric or multiferroic materials has only recently begun to be explored [9] and will likely play a role as people continue to maximize functionality in nanostructures.

The interfaces formed between magnetic thin films have been explored for many years, although surprisingly magnetism in the epitaxial interface between CrO_2 and its native oxide Cr_2O_3 has not earned much attention. These two materials are interesting technologically due to CrO_2 being a spin-polarized ferromagnet and Cr_2O_3 being a magnetoelectric antiferromagnet. In this dissertation we present evidence for interfacial coupling between the two materials, which is manifest in an enhanced anisotropy measured using transverse susceptibility. The anomalous anisotropy observed in this system is likely due to contributions from exchange coupling between the ferromagnetic and antiferromagnetic phases as well as strain present from both CrO_2 interfaces.

We also examine how the magnetic properties of polycrystalline barium hexaferrite, a magnetic material possessing very high magnetocrystalline anisotropy, change when grown as a multilayer with barium strontium titanate, a ferroelectric. We demonstrate how

the functional dependence of the coercivity with respect to temperature is altered by the presence of the barium strontium titanate, which could be useful for tuning the anisotropy of barium hexaferrite in multilayer thin films.

In all of the systems described above, it is clear that a solid understanding of the magnetic anisotropy from all contributions must be reached before materials can achieve their full potential. This means measuring the effective anisotropy of the system and figuring out how the surfaces and interfaces of nanoscale materials may affect the result. Transverse susceptibility has been shown over the years to be an excellent method of measuring the anisotropy in systems from thin films to nanoparticles [79, 12, 66, 67]. It is a direct measure of the anisotropy field in a sample and can be used to extract the effective anisotropy constant. While thus far minimal work has been done using transverse susceptibility to measure the exchange coupling in multilayer thin films [80], one of the most important outcomes of this dissertation is to show that it is quite a valuable technique for understanding the complex magnetic behavior exhibited in multifunctional materials.

1.1 Literature Review

1.1.1 Magnetic Nanoparticles for Biomedical Applications

Pankhurst *et al.* [62] and Berry *et al.* [7] provided recent topical reviews of applications of magnetic nanoparticles in biomedicine though both works stopped short of invoking the special need for fine-tuning the size and magnetic properties of nanoparticles. While functionalization of Fe_3O_4 was discussed, the use of Au as a coating was not covered in detail. Since then, there have appeared several articles outlining the synthesis and characterization of Au-Fe_3O_4 nanoparticles for biomedical applications including but not limited to Mandal *et al.* [49], Lyon *et al.* [46], Gangopadhyay *et al.* [20], and Lu *et al.* [44]. These studies focus mainly on the synthesis and DC properties but fail to directly examine how the Au-coating reduced inter-particle interactions. In chapter 5 we provide direct evidence of the decrease in inter-particle interactions when Au is used as a coating.

One of these studies [20] proposed Au as a catalyst for laser-induced hyperthermia. Hyperthemia using just Fe_3O_4 or γ-Fe_2O_3 nanoparticles has received attention in several publications [5, 20, 61, 17]. These publications address the need to tap into both relaxation processes (Néel and Brownian), but only the recently published Eggeman *et al.* [17] suggests tuning the blocking frequency to utilize hysteretic losses in DC superparamagnetic particles. While we are unable to measure the AC hysteresis loops of our Au-Fe_3O_4 particles, we showed that these particles, while superparamagnetic in DC fields, display a transverse susceptibility signal consistent with ferromagnetic particles. This would imply that in AC fields of high enough frequency, hysteretic losses can contribute to particle heating in our samples.

1.1.2 Au-Fe_3O_4 Composite Particles

The synthesis of "dumbbell"-shaped Au-Fe_3O_4 particles was reported by our collaborators at Brown University [93] for the purpose of using the Au and Fe_3O_4 surfaces simultaneously for biomedical applications. To our knowledge this is the only such instance of suggesting a composite particle with more than one surface for drug delivery. This same paper also referenced the synthesis of novel "flower"-shaped Au-Fe_3O_4 particles as the result of slight changes in solvent pH. In this dissertation we perform a wide array of magnetic measurements on these particles to compare and contrast how the geometrical configuration and interfaces affect the magnetic properties. These differences result in fascinating magnetic properties associated with the flower particles, which can be attributed to increased intra-particle interaction and magnetic frustration. Though the Au at the center of these clusters may be difficult to functionalize for some biomedical applications, the anisotropy associated with these particles and the ability to tune the size of each component could make them attractive for hyperthermia.

The increased anisotropy of the flower particles could also be viewed in light of finding ways to overcome the superparamagnetic limit in magnetic recording. The discussion of novel-shaped particles and their surfaces for this purpose is fairly limited, though Albrecht

et al. [3, 48] have made some recent advances in this regards by capping polystyrene nanoparticles with Co/Pt multilayers so that the magnetic nanocaps have novel shape and interface anisotropy. Other lithographically patterned exchange-biased nanostructures are described in Nogués *et al.*'s topical review of exchange bias in nanostructures [60]. While such patterned media by lithography is getting attention for magnetic recording, chemical synthesis of novel anisotropic particles should not be ruled out because of its ease and cost-effectiveness.

From a fundamental physics point of view, surface anisotropy in nanoparticles has been explored in several publications, most notably Kodama *et al.*'s work on $NiFe_2O_4$ [38]. Since then, the issues of exchange bias from surface disorder has been explored for Fe_3O_4 [92, 22] and γ-Fe_2O_3 as well as modeled by Kachkachi and Dimian [37] and Bødker *et al.* [8]. However, exchange bias behavior in cluster-type nanoparticles with competing interactions contributing to the effective anisotropy including spin frustration and multiple interfaces is a topic that has not yet been addressed in the magnetism community.

1.1.3 CrO_2 Epitaxial Thin Films and Bilayer Cr_2O_3 Thin Films

Exchange bias in thin films has been observed in several systems dating back over 50 years to Meiklejohn and Bean [53], although there is still no comprehensive theory that can explain all of the aspects associated with it. The phenomenon of a uniaxial exchange anisotropy without a unidirectional anisotropy between an antiferromagnet and a ferromagnet has been reported in recent years by Leighton *et al.* [42, 41], and the spin-flop explanation for it was proposed by Shulthess and Butler [72]. The CrO_2/Cr_2O_3 system itself has been studied only minimally in thin film form for the purpose of measuring the oxide layer as a tunnel barrier [14] and in nanoparticle form for exchange bias effects [95]. The closest comparable work to the CrO_2/Cr_2O_3 system is the $[Co/Pt]_5/Cr_2O_3$ bilayer system published by Borisov *et al.* [9], in which the magnetoelectric properties of Cr_2O_3 were used to switch the sign of the exchange bias of the multilayers. Exchange coupling between CrO_2 and Cr_2O_3 in thin film form has not been reported, and our use

of transverse susceptibility to measure this system is a contribution to the understanding of uniaxial exchange anisotropy in ferromagnetic/antiferromagnetic bilayers and the first such measurement of a ferromagnetic/magnetoelectric bilayer.

1.1.4 Barium Hexaferrite/Barium Strontium Titanate Multilayer Thin Films

Finally, most of the work that has been done on the BaM/BSTO system has been reported since the completion of the author's master's thesis. This has come from work done by Dr. Ranko Heindl, who received his Ph.D. as a result of his work on epitaxial BaM/BSTO bilayers [29]. He was able to demonstrate the dual tunability of the permittivity and permeability of this system for radio frequency applications. The growth optimization and magnetic characterization of polycrystalline BaM/BSTO multilayer films was an important advancement towards the high-quality films that have been grown since this work was originally performed and published.

1.2 Dissertation Outline

- Chapter two gives a brief overview of magnetism in materials which serves as a foundation for the magnetic properties discussed throughout the dissertation. Besides addressing the main types of magnetism found in materials we discuss the phenomenon of superparamagnetism as well as the exchange coupling that can exist at the interface of ferromagnetic and antiferromagnetic materials.

- Chapters three and four describe the measurement techniques used in this work. Chapter three discusses the traditional measurement techniques used in the magnetism community. Chapter four discusses the method of transverse susceptibility, a lesser-known technique which is a direct measurement of the anisotropy field of a material. Special attention is paid to this method as it is an integral measurement used for the dissertation.

- Chapters five and six contain measurement results for Au-Fe_3O_4 nanoparticles in different configurations. Chapter five is dedicated specifically to core-shell Au-Fe_3O_4 nanoparticles for biomedical applications and includes work done in conjunction with the USF College of Medicine in fulfillment of the requirements of the National Science Foundation Integrated Graduate Education Research and Traineeship (IGERT) Fellowship. Chapter six explores two other geometrical configurations of the Au-Fe_3O_4 system, the "dumbbell" and "flower" configuration which are interesting for fundamental physics and a variety of technological applications from biomedicine to magnetic storage.

- Chapter seven focuses on the magnetic anisotropy of CrO_2/Cr_2O_3 thin films, a multifunctional system composed of a ferromagnet and an antiferromagnet which is also a magnetoelectric material. This chapter discusses in detail the properties of CrO_2 single layer thin films as well.

- Chapter eight is a summary of the author's work for her master's thesis which is the growth and characterization of barium hexaferrite/barium strontium titanate multilayer thin films.

- Chapter nine concludes the dissertation and proposes new directions for the future of this research.

CHAPTER 2

A REVIEW OF MAGNETISM IN MATERIALS

2.1 Nomenclature

Every material which is subject to a magnetic field, **H**, acquires a magnetic moment. The magnetic moment of an atom has three sources: electron spin, electron orbital momentum about the nucleus, and the change in the orbital momentum induced by an applied magnetic field. The dipole moment per unit volume is defined as the magnetization, **M**. In most materials, **M** is proportional to the applied field **H**, such that

$$\mathbf{M} = \chi \mathbf{H} \tag{2.1}$$

where χ is the magnetic susceptibility. The susceptibility indicates how responsive a material is to an applied magnetic field.

The magnetic induction is usually what is presented in Maxwell's equations and is related to **M** and **H** by the following

$$\mathbf{B} = \mu_0(\mathbf{H} + \gamma \mathbf{M}) \tag{2.2}$$

where μ_0 is permeability of free space. Here γ is a a constant that depends upon which system of units is being used. In SI units, $\gamma = 1$, in Gaussian and cgs units, $\gamma = 4\pi$. This dissertation will use cgs units for which $\mu_0 = 1$. **B** is the same as the density of magnetic flux inside the material. If the relationship between **M** and **H** is linear, then **B** can also be written as

$$\mathbf{B} = \mu \mathbf{H} \tag{2.3}$$

where

$$\mu = \mu_0(1 + \gamma\chi) = \mu_0\mu_r \tag{2.4}$$

is known as the magnetic permeability.

For materials that have a linear relationship between **M** and **H**, their magnetic behavior can be classified in terms of χ and μ_r. However, some materials do not have a linear relationship between **M** and **H**, and in fact **M** may not even be a single-valued function of **H** but may instead depend on the history of the applied field. This point will be discussed much more extensively in later sections.

2.2 Diamagnetism

All materials exhibit diamagnetism. It is a very weak effect, and if this is the only magnetic response they display, they are referred to as diamagnets. In diamagnetic materials, $\chi < 0$ and $\mu_r < 1$. This indicates that the magnetic flux inside of a diamagnet is less than the flux outside, and the magnetization of a diamagnet decreases in magnitude in response to the applied field.

Diamagnetism arises from the change in orbital motion of electrons in a material in response to an applied field. While orbital motion of electrons can only be correctly described using quantum mechanics, diamagnetism is often derived using a semi-classical approach which yields the same result. If we consider an electron moving in a circular orbit, it feels a centripetal force due to the Coulomb attraction to the nucleus. We can explain diamagnetism as occurring from the change in velocity of the electron that arises once the Lorentz force from the magnetic field, $(e/c)\mathbf{v} \times \mathbf{B}$, is added to the the centripetal force already acting on the electron. This force decreases the velocity, which in turn decreases the current caused by the orbiting charge, and the result is a decreased magnetic moment. It is the decrease in magnetic moment that is observed as the diamagnetic effect. This explanation is semi-classical in that it assumes a circular orbit using the results of

quantum mechanics, which explain how electrons are able to effectively move about the nucleus. [1]

2.3 Paramagnetism

While diamagnetism is a result of electron orbital motion, paramagnetism is the result of electron spins interacting with an applied magnetic field. Paramagnetism is characterized by a positive susceptibility ($\chi > 0$) and a magnetic permeability (μ_r) greater than 1. It corresponds to the magnetic behavior found in materials in which localized magnetic moments are present but in which no net macroscopic magnetization exists in zero applied field. This is because the magnetic moments are only weakly coupled to each other, so thermal energy causes random alignment of the moments. When a magnetic field is applied, the moments start to align, but only a small fraction is deflected into the field direction for practical field strengths. A schematic of the magnetic spins in a paramagnetic material is shown in figure 2.1.

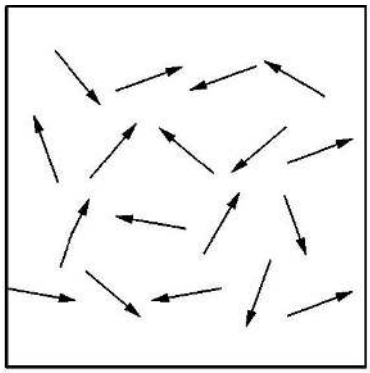

Figure 2.1. The spins in a paramagnet in the absence of a magnetic field. Figure adapted from reference [30].

2.4 Magnetic Ordering

Magnetic ordering comes about when spins of the atoms in a material are allowed to interact with one another via exchange interactions. These interactions occur between the

spins of the ions at the lattice sites and are caused by the overlap of the electronic wave functions.

If we consider a simple model with two electrons which have spatial coordinates $\mathbf{r}_1$ and $\mathbf{r}_2$, then the wave function for the system can be written as a product of the single electron states. If the first electron is in state $\psi_a(\mathbf{r}_1)$ and the second electron state is in state $\psi_b(\mathbf{r}_2)$, then the joint wave function is $\psi_a(\mathbf{r}_1)\psi_b(\mathbf{r}_2)$. This product state does not obey exchange symmetry since interchanging the two electrons yields $\psi_a(\mathbf{r}_2)\psi_b(\mathbf{r}_1)$ which is not a multiple of the original wave function. The only states allowed are symmetrized or antisymmetrized product states.

For electrons the overall wave function must be antisymmetric so the spin part of the wave function must either be an antisymmetric singlet state χ_S (S = 0) or a symmetric triplet state χ_T (S = 1). For the wave function in the singlet case

$$\Psi_S = \frac{1}{\sqrt{2}}[\psi_a(\mathbf{r}_1)\psi_b(\mathbf{r}_2) + \psi_a(\mathbf{r}_2)\psi_b(\mathbf{r}_1)]\chi_S \tag{2.5}$$

and in the triplet case

$$\Psi_T = \frac{1}{\sqrt{2}}[\psi_a(\mathbf{r}_1)\psi_b(\mathbf{r}_2) - \psi_a(\mathbf{r}_2)\psi_b(\mathbf{r}_1)]\chi_T \tag{2.6}$$

The energies of the two possible states are

$$E_S = \int \Psi_S^* \mathcal{H} \Psi_S d\mathbf{r}_1 d\mathbf{r}_2 \tag{2.7}$$

and

$$E_T = \int \Psi_T^* \mathcal{H} \Psi_T d\mathbf{r}_1 d\mathbf{r}_2 \tag{2.8}$$

The energy difference between the states can then be expressed as

$$E_S - E_T = 2 \int \psi_a^*(\mathbf{r}_1)\psi_b^*(\mathbf{r}_2)\mathcal{H}\psi_a(\mathbf{r}_2)\psi_b(\mathbf{r}_1)d\mathbf{r}_1 d\mathbf{r}_2 \tag{2.9}$$

The Hamiltonian of two interacting spins is usually expressed as

$$\mathbf{S}_1 \cdot \mathbf{S}_2 \tag{2.10}$$

where $\mathbf{S}_1$ and $\mathbf{S}_2$ are the spin operators. For the singlet state $\mathbf{S}_1 \cdot \mathbf{S}_2 = -3/4$ while for the triplet state $\mathbf{S}_1 \cdot \mathbf{S}_2 = 1/4$. The Hamiltonian can be written as an 'effective Hamiltonian'

$$\mathcal{H} = \frac{1}{4}(E_S + 3E_T) - (E_S - E_T)\mathbf{S}_1 \cdot \mathbf{S}_2 \tag{2.11}$$

The first term is a constant, but the second term appears in equation 2.9. The integral part of equation 2.9 is the exchange integral and can be defined as

$$\mathbf{J} = \frac{E_S - E_T}{2} = \int \psi_a^*(\mathbf{r}_1)\psi_b^*(\mathbf{r}_2)\mathcal{H}\psi_a(\mathbf{r}_2)\psi_b(\mathbf{r}_1)d\mathbf{r}_1 d\mathbf{r}_2 \tag{2.12}$$

So the spin-dependent term in the effective Hamiltonian can be written as

$$\mathcal{H}^{spin} = -2\mathbf{J}\mathbf{S}_1 \cdot \mathbf{S}_2 \tag{2.13}$$

If $\mathbf{J} > 0$, $\mathrm{E}_S > \mathrm{E}_T$, and the triplet state S = 1 is favored. If $\mathbf{J} < 0$, $\mathrm{E}_S < \mathrm{E}_T$, and the singlet state S = 0 is favored.

Generalizing the exchange interaction between two electrons to a many-bodied system is quite a complex problem. We can nevertheless describe a simplified situation in which neighboring atoms experience the exchange interaction as

$$\mathcal{H} = -\sum_{ij} \mathbf{J}_{ij}\mathbf{S}_i \cdot \mathbf{S}_j \tag{2.14}$$

This is the Heisenberg model of neighboring electrons where $\mathbf{J}$ is the exchange constant between the i^{th} and j^{th} spins. The factor of 2 is not necessary, because the summation includes each pair of spins twice.

A positive exchange interaction causes spins to align parallel to each other, leading to ferromagnetism. A negative exchange interaction causes spins to align antiparallel to each other and leads to antiferromagnetism. These exchange interactions are what cause spontaneous magnetic moments in materials which in turn result in the complicated nonlinear and multi-valued relationships between **M** and **H**.

2.4.1 Ferromagnetism

When the exchange interaction between two neighboring spins is positive, they align in the same direction regardless of whether there is an external field or not, and this gives rise to a spontaneous magnetization (figure 2.2). This type of long-range magnetic ordering is known as ferromagnetism. However, most macroscopic ferromagnetic samples are not magnetized (possessing a net magnetization) unless an external magnetic field is applied. This is because it is more energetically favorable for the coupled spins to break into magnetic domains, or small regions where the spins are aligned. Each domain can have a magnetic moment which is oriented in a different direction from that of its neighbor. While the exchange energy favors the alignment of neighboring spins, the magnetostatic energy is highest (and therefore unfavorable) when a macroscopic sample has all of its spins aligned. Thus, the lowest energy state of a ferromagnet is one made up of domains whose magnetization vectors are pointing in different directions and the domains themselves are made of strongly coupled spins aligned in the same direction.

Applying an external magnetic field to a ferromagnet causes the domains to orient in the same direction and a net magnetization to arise. This response is nonlinear and is one of the main characteristics of ferromagnets. The magnetization rapidly increases with applied field until the ferromagnet is saturated, i.e. the domains are all aligned in the direction of the magnetic field. This maximum magnetization in response to an applied field is referred to as the saturation magnetization (M_S). When the field is decreased back to zero, the magnetization as a function of field does not follow the same path as it did with increasing field. In fact, when the field goes all the way back to zero, there

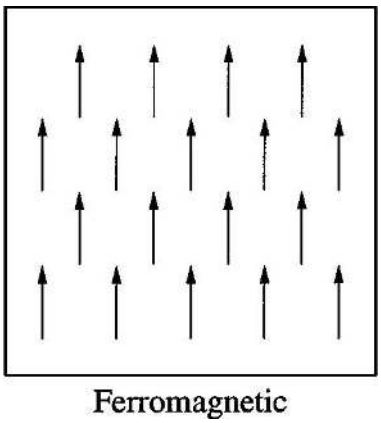

Figure 2.2. Magnetic ordering in a ferromagnet. Figure adapted from reference [30].

remains a net magnetic moment called the remanent magnetization, M_R. In order for the material to return back to zero net magnetic moment, i.e. the moments of the domains to be randomized, a magnetic field needs to be applied in the opposite direction. The magnetic field needed to accomplish this is called the coercive field, H_C, or coercivity. The coercivity of a material is a very important property whose value is heavily dependent on the crystal structure and growth conditions of the sample. These factors will be discussed further in section 2.5.

If the field is decreased even further, the domains will reorient in the opposite direction and align at the negative saturation magnetization. There is also a negative remanent magnetization and coercive field when bringing the applied field back to zero and upon increasing it again in the positive direction. One full cycle of this magnetization versus field (from zero to positive saturation to negative saturation and back to positive saturation) is called an M-H curve or a hysteresis loop. It is presented schematically labeled with M_S, M_R and H_C in figure 2.3.

Ferromagnets undergo a phase transition at a critical temperature called the Curie temperature, T_C. This temperature is different for every material and depends upon the strength of the exchange interaction between spins. When the thermal energy is high enough to overcome the exchange energy, the spins are no longer coupled to each other over a long range, and the material effectively becomes paramagnetic.

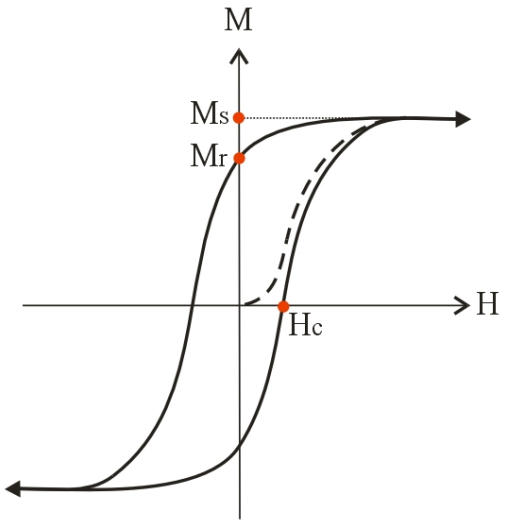

Figure 2.3. Diagram of a magnetization versus field (M-H) curve of a ferromagnetic material. The characteristics to note are saturation magnetization (M_S), remanent magnetization (M_R) and coercivity (H_C). Figure adapted from reference [28].

2.4.2 Antiferromagnetism

In antiferromagnetic materials, the exchange interaction is negative and aligns the spins antiparallel to each other. Antiferromagnets can be thought of as containing two interpenetrating and identical sublattices of magnetic ions. Although one set of magnetic ions is spontaneously magnetized below some critical temperature (in this case called the Néel temperature) the second set is spontaneously magnetized by the same amount in the opposite direction (figure 2.4). As a result, antiferromagnets have no net magnetization, and their response to external fields is similar to that of paramagnetic materials - the magnetization is linear in the applied field and the susceptibility is small and positive.

2.4.3 Ferrimagnetism and Ferrites

Ferrimagnets are a special class of antiferromagnets in that the exchange coupling between adjacent magnetic ions leads to antiparallel alignment but they have a net spontaneous magnetic moment similar to ferromagnets. This net moment occurs because the

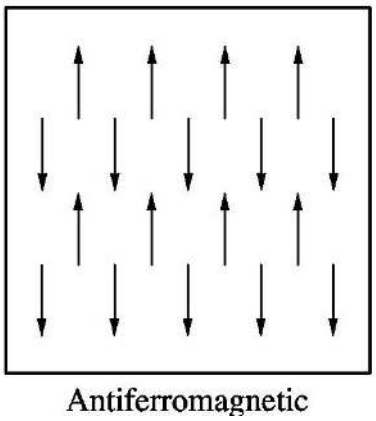

Figure 2.4. Magnetic ordering in an antiferromagnet. Figure adapted from reference [30].

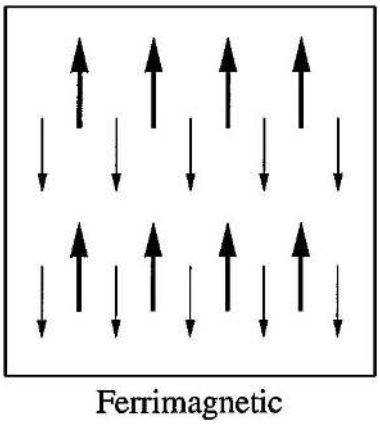

Figure 2.5. Magnetic ordering in a ferrimagnet. Figure adapted from reference [30].

magnetization of one sublattice is greater than that of the oppositely oriented sublattice (figure 2.5).

The most technologically important class of ferrimagnets are ferrites, which are mixed metal oxides containing the compound Fe_2O_3. Two classes of ferrites, cubic (spinel) ferrites and hexagonal ferrites, are the subject of much of the research presented in this dissertation. Cubic ferrites have the general formula $MO{\cdot}Fe_2O_3$, and hexagonal ferrites have the general formula $MO{\cdot}6(Fe_2O_3)$. M can be a divalent ion such as Mn, Ni, Zn, Co, Mg in the case of cubic ferrites; in hexagonal ferrites M is usually Ba or Sr. Chapters 5 and 6 focus on magnetite, Fe_3O_4 (or $FeO{\cdot}Fe_2O_3$) and chapter 8 discusses $BaFe_{12}O_{19}$ (or $BaO{\cdot}6(Fe_2O_3)$).

Ferrites are electrically insulating and find applications in situations where the electrical conductivity present in most ferromagnetic materials would be detrimental. They are widely used in high frequency applications, because an AC field does not produce undesirable eddy currents in an insulating material.

2.5 Magnetic Anisotropy

Magnetic anisotropy refers to the dependence of the magnetic properties on the direction in which they are measured. The magnitude and type of anisotropy affect many properties of the material including coercivity and blocking temperature in nanoparticles. As a result, studying the anisotropy and determining what factors contribute to increased or decreased anisotropy leads to creating better materials for a particular application. Magnetic anisotropy is a topic that will be discussed frequently throughout this dissertation and this section describes a few of the sources of anisotropy encountered in the subsequent chapters.

2.5.1 Magnetocrystalline Anisotropy

Magnetocrystalline anisotropy is the tendency of the magnetization in a material to align itself along a preferred cystallographic direction. The preferred directions are called the "easy" axes since it is easiest to magnetize and demagnetize a sample to saturation if the external field is applied along a preferred direction. When examining hysteresis loops with the field applied along easy and hard axes, a couple of differences can be seen. When the field is applied in the easy direction, the rise of the magnetization to saturation is more rapid and M_S is reached at a much lower field. This indicates that a smaller field was required to align the spins along the field direction. Also, when the sample is magnetized along an easy axis, it retains more of its magnetization when the field is removed: M_R is higher. The squareness ratio of a curve, defined as $S = M_R/M_S$, is a measure of how effective a material is at staying magnetized in the absence of a field. For materials magnetized in their easy direction, S is maximized. Along the hard axis of magnetization, it takes a much

larger field to reach M_S. When the field is reversed the magnetization does not go back to the remanent magnetization that it would along the easy axis. For many materials, the magnetization is completely unstable along the hard axis and returns to zero once the field is removed. The squareness, S, is minimized for loops taken along the the hard axis, because M_R has been minimized. The saturation magnetization remains the same independent of field direction, even though the field required to reach it is different.

The anisotropy energy is the energy required to rotate a spin system of a domain away from the easy direction. This is actually just the energy required to overcome the spin-orbit coupling, because reorienting the spin also requires reorientation of the electron orbit. The orbit is strongly coupled to the lattice, which is where most of the resistance to rotation originates. Therefore the strength of the spin-orbit coupling in a material determines the magnetocrystalline anisotropy.

For cubic structures, the magnetocrystalline anisotropy is expressed as a series expansion of the direction cosines α_i of the saturation magnetization relative to the crystal axes[1]:

$$E = K_1(\alpha_1^2\alpha_2^2 + \alpha_2^2\alpha_3^2 + \alpha_3^2\alpha_1^2) + K_2(\alpha_1^2\alpha_2^2\alpha_3^2) + ... \tag{2.15}$$

where K_1, K_2, etc. are the anisotropy constants. This type of magnetocrystalline anisotropy is called cubic anisotropy.

For hexagonal structures, the anisotropy is said to be uniaxial because the there is just one easy axis of magnetization, and so the anisotropy is defined only by the angle of the applied field with the easy axis. The expression for uniaxial anisotropy is [1]

$$E = K_1 \sin^2\theta + K_2 \sin^4\theta + ... \tag{2.16}$$

It is important to remember that the anisotropy constants are temperature dependent and decrease with increasing temperature due to the thermal energy contribution.

2.5.2 Shape Anisotropy

If a sample is polycrystalline, then it will show no net crystalline anisotropy because there will be crystallites pointed in all directions. However only if the sample is exactly spherical will the same field magnetize it to the same extent in every direction. If the sample is not spherical, then it will be easier to magnetize it along a long axis. This is known as shape anisotropy. The origin of shape anisotropy is the demagnetizing field. When a sample is magnetized it will produce magnetic charges or poles at the surface. This surface charge distribution is itself another source of a magnetic field, called the demagnetizing field and it acts in opposition to the magnetization that produces it. Demagnetizing fields are complicated to calculate and are solely a function of the shape of the sample. The demagnetizing field and thus shape anisotropy constant increases as the aspect ratio of the sample or particle increases.

2.5.3 Surface Anisotropy

The last type of anisotropy to be discussed is surface anisotropy. A spin on the surface of a sample or particle has a nearest neighbor on one side of it, but not the other. Therefore the exchange energy at the surface cannot be the same as in the bulk. In macroscopic samples, the role of the surface spins is negligible compared to the bulk behavior. However, as the surface-area-to-volume ratio increases for nanoparticles, a larger percentage of the spins reside on the surface, contributing a larger amount to the overall magnetic response. The result is a larger coercivity as a larger field is needed to reverse the surface spins, which in a nanoparticle point radially outwards instead of aligning with the interior spins [8].

While surface spins have missing nearest neighbors, spins at the interface of two materials also have environments that are different from the bulk. This interface anisotropy becomes more important as thin film nanostructures and nanocomposites become more prevalent in device applications. The interface between a ferromagnet and an antiferromagnet leads to exchange coupling, which is discussed in a later section.

2.6 Magnetic Nanoparticles and Superparamagnetism

When the size of a magnetic particle is small enough that the formation of domains is not favorable, the particle is said to be single domain. This usually occurs on the nanometer scale, and the realization of magnetic nanoparticles has profound consequences for all sorts of technological applications from drug delivery to magnetic recording. In general, magnetic nanoparticles show superior magnetic properties, such as an enhanced saturation magnetization and remanent magnetization. When the particle is in the ferromagnetic state, the coercivity is much larger as well.

When a particle's size is on the single domain scale, a phenomenon known as superparamagnetism is possible. This occurs when the thermal energy is enough to demagnetize the particle in the absence of an applied field. For an array of particles, it means that the net moment associated with each particle easily aligns with an applied field but is free to rotate once the field is removed. This situation is analogous to a paramagnet, only instead of each individual spin aligning with the field and then randomizing after the field is removed, there are particles composed of roughly 10^5 spins that can align with the field. This results in a much higher susceptibility and better magnetic response than a traditional paramagnet, but there is no coercivity or remanent magnetization.

Magnetic nanoparticles can exhibit superparamagnetism only when the temperature is high enough to cause demagnetization by overcoming the anisotropy energy in the absence of a field. When the temperature is lowered and the thermal energy is not enough to demagnetize the particles, they again behave as single domain particles with magnetic hysteresis. This critical temperature is called the blocking temperature (T_B), and it depends on the particle's intrinsic properties and size.

The conditions given above for superparamagnetism all assume that the particles demagnetize due to thermal energy simultaneously with the removal of a field, and on the timescale of most DC measurements this appears to be true. However, there is a finite timescale for the particles to demagnetize, and when the magnetic properties are probed

with an AC field, the blocking temperature can increase. Thus measurement frequency is also a factor when describing the blocking behavior of a superparamagnetic system.

Superparamagnetic particles can be very useful for many applications. Because they do not maintain a permanent moment, they don't agglomerate, so they are useful for suspending in magnetic fluids (or ferrofluids) that are used for biomedical imaging and targeted drug delivery. Their lack of coercivity means they have no magnetic losses, which makes them ideal for AC applications like transformers. However, their lack of coercivity and stability makes it impossible to use superparamagnetic nanoparticles for magnetic storage. In fact, "beating the superparamagnetic limit" has become a priority for hard drive companies who want greater areal density while still maintaining magnetic stability.

2.7 Exchange Coupling in Nanostructures

When materials with ferromagnetic-antiferromagnetic interfaces are cooled through the Néel temperature of the antiferromagnet, an exchange anisotropy is induced in the ferromagnet. This type of anisotropy was discovered in 1956 by Meiklejohn and Bean while studying Co particles embedded in a CoO matrix [53]. Exchange anisotropy is due to the coupling of the interface spins and can be observed in antiferromagnetic/ferromagnetic thin films, core-shell nanoparticles, and antiferromagnetic/ferromagnetic composites of particles in a matrix.

After cooling an exchange-coupled sample from above T_N (but below the T_C of the ferromagnet), the hysteresis loop of the antiferromagnet/ferromagnet system can be shifted along the field axis generally in the direction opposite ('negative') to the cooling field. This results in the absolute value of the coercive field being different for the increasing and decreasing fields. This phenomenon is known as exchange bias, H_E. The hysteresis loops will also have an increased coercivity H_C which, along with H_E, disappears at or near T_N, confirming that it is the antiferromagnet that is responsible for this behavior. Figure 2.6 is a diagram summarizing exchange-biased materials and the modified hysteresis loop due to exchange anisotropy.

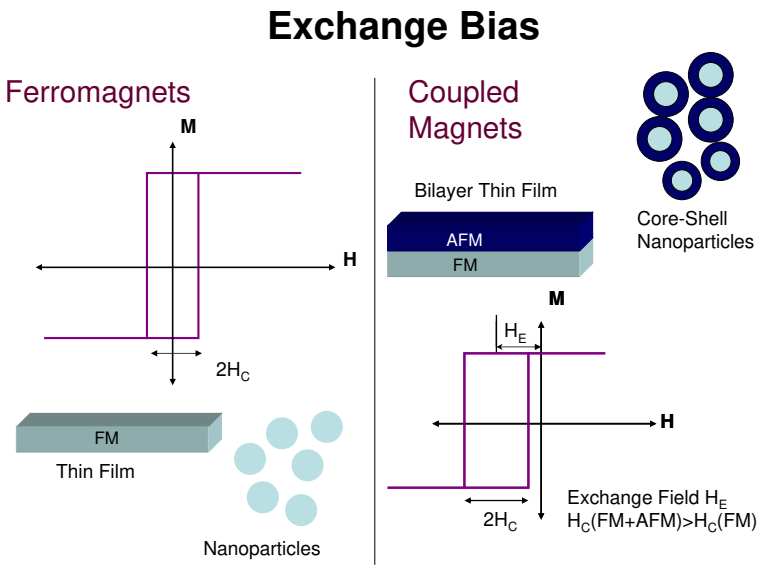

Figure 2.6. Exchange bias systems and associated phenomena.

The shift in hysteresis loop can be qualitatively explained by the antiferromagnetic interface spins inducing a unidirectional anisotropy in the ferromagnet. When a field is applied above T_N, the ferromagnetic spins line up with the field, while the antiferromagnetic spins remain randomized (figure 2.7(i)). When cooling through T_N in the presence of a field due to the interaction at the interface, the antiferromagnetic spins next to the ferromagnetic spins align ferromagnetically. The other spin planes in the antiferromagnet remain aligned antiferromagnetically so the antiferromagnet still has no net moment (figure 2.7(ii)). When the field is reversed, the ferromagnetic spins begin to rotate. For sufficiently large antiferromagnetic anisotropy, the antiferromagnetic spins do not rotate (figure 2.7(iii)). The antiferromagnetic spins at the interface exert a torque on the ferromagnetic spins to keep them in their original position. Therefore, the ferromagnetic spins have one stable configuration, i.e. the anisotropy is unidirectional. The field needed to completely reverse the ferromagnetic layer will be larger, because a larger field is needed to overcome the torque. However, once the field is rotated back to its original direction, the ferromagnetic spins will start to rotate at a smaller field due to the influence of the antiferromagnetic spins which now exert a torque in the same direction as the field (figure

2.7(v)). The material in effect acts as if there were an internal biasing field, hence the term "exchange bias".

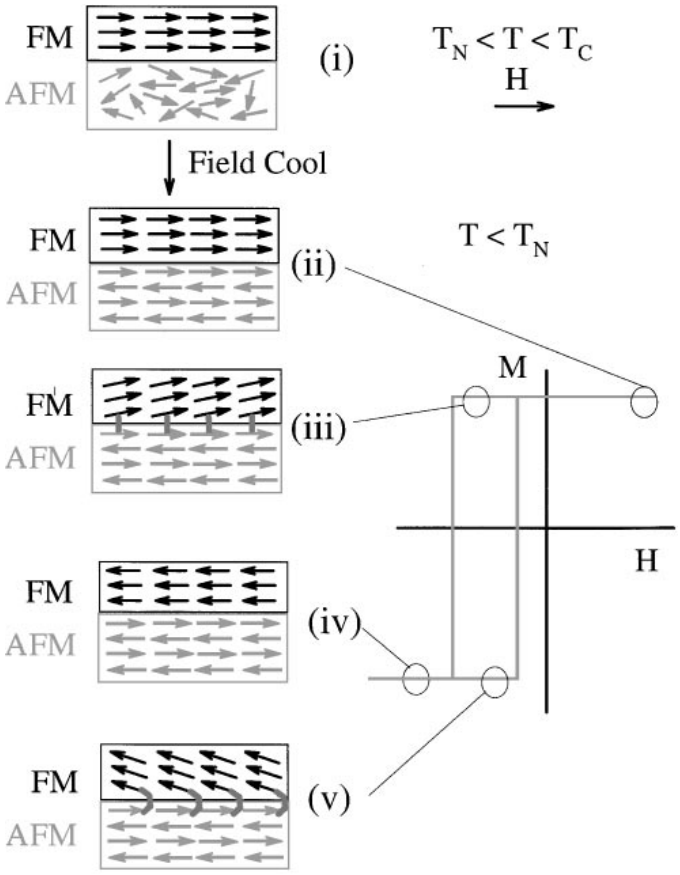

Figure 2.7. Schematic diagram of the spin configuration of an antiferromagnet/ferromagnet bilayer at different stages (i)-(v) of an exchange biased hysteresis loop. Figure adapted from reference [59].

There are some exchange-coupled systems for which an increase in coercivity is observed after field-cooling, but there is no shift in hysteresis loop. In such a situation, the antiferromagnetic anisotropy is too low to create a unidirectional anisotropy in the ferromagnet. After saturation of the ferromagnetic spins when the field is reversed, the antiferromagnetic spins can be dragged by the spins in the ferromagnet. It is energetically favorable that the spins in both the ferromagnet and the antiferromagnet rotate together. The result of dragging the antiferromagnet spins in both directions results in a uniaxial anisotropy and an increase in coercivity, H_C.

Exchange coupled thin films are used in numerous technological applications such as spin-valve sensors, magnetic tunnel junction read heads for hard disk drives, and magnetic random access memory [48]. The enhanced coercivity and anisotropy that are observed in these types of systems have led to exchange-coupled nanoparticles and lithographically patterned structures being proposed to beat the superparamagnetic limit in magnetic media.

CHAPTER 3

MEASUREMENT TECHNIQUES

All of the measurement techniques described in this chapter were performed using a commercial Physical Properties Measurement System (PPMS) from Quantum Design. The PPMS consists of a liquid helium dewar with a 7 Tesla longitudinal superconducting magnet and a temperature controller in the range 2K to 350K (figure 3.1). Magnetization versus field, magnetization versus temperature, and AC susceptibility measurements were all performed using the AC/DC Magnetometry System (ACMS), a feature of the PPMS. The transverse susceptibility measurements were performed using a modified Quantum Design Multifunctional Probe.

Figure 3.1. Physical Properties Measurement System (PPMS).

3.1 DC Magnetization Measurements

The most common DC magnetic measurement is the magnetization versus field (M-H) curve, which was discussed in great detail in chapter 2. This measurement yields the saturation magnetization M_S, remanent magnetization M_R, and coercive field H_C. It can be an indicator of anisotropy because the shape and squareness ratio is different when H is applied along the easy and hard axes of magnetization. Lastly, when taken after cooling in a field, a shift along the horizontal axis along with an increase in H_C is an indication of exchange coupling.

This section discusses magnetization versus temperature measurements which are often used to characterize magnetic materials. This is usually done by taking zero field cooled (ZFC) and field cooled (FC) magnetization curves. $M_{ZFC}(T)$ is determined by cooling a sample with $H = 0$ to low temperature, so that the magnetic moments of the particles have random orientations. A small, constant field (typically around 100 Oe) is applied so that there is a measurable magnetization as the temperature is increased. M_{ZFC} increases as the thermal energy is raised, and there is sufficient energy to align the particle moments parallel to the field. M_{ZFC} drops again at high temperature when thermal fluctuations are able to demagnetize the sample and a sharp drop off is seen at the Curie temperature, T_C, when the magnetization is destabilized due to thermal fluctuations. For magnetic nanoparticles, the ZFC measurement is especially useful for determining the average blocking temperature, T_B. In the ZFC initial state at low temperature, the net magnetization is ideally zero. When a field is applied, and the magnetization measured as the temperature is raised, only particles with T_B less than the measuring temperature contribute. Therefore, the average blocking temperature for the array of particles is seen as a maximum in the ZFC curve.

The FC magnetization, $M_{FC}(T)$, is measured by first applying a small field (again around 100 Oe) at room temperature. As the sample is cooled, the magnetization rises as thermal fluctuations become less important. Unlike M_{ZFC}, the FC magnetization saturates at low temperature. The point where the ZFC and FC curves meet is often referred to as the freezing temperature (T_F), and indicates the onset of irreversible magnetization at the

field in which the measurement is taken. For magnetic nanoparticles, this often coincides with the blocking temperature, T_B.

A sample graph of a ZFC curve plotted along with an FC curve (this is the typical representation) for a sample of $NiFe_2O_4$ nanoparticles is shown in figure 3.2. These particles were made by another graduate student in the lab and the magnetic properties were studied extensively [21].

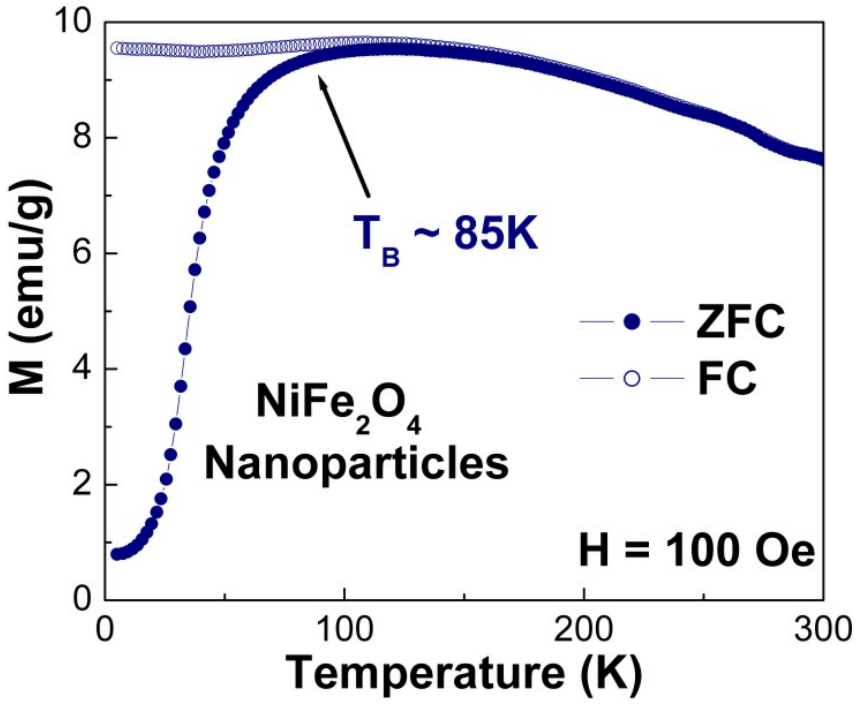

Figure 3.2. Zero field cooled (ZFC) and field cooled (FC) magnetization versus temperature curves for $NiFe_2O_4$ nanoparticles.

3.2 AC Susceptibility

While DC magnetic measurements generally measure the equilibrium magnetic properties of a sample, AC magnetic measurements can probe the timescale at which many magnetization processes occur, and provide valuable information about particle interactions, spin dynamics, and the presence of magnetic transitions. Instead of applying a

large DC magnetic field, a small AC magnetic field is used, which causes a time-dependent moment in the sample.

At low frequencies, where the measurement is most similar to a DC measurement, the magnetic moment of the sample follows the M(H) curve that would be measured in a DC experiment. As long as the AC field is small, the induced AC moment is

$$M_{AC} = \chi \times H_{AC} \sin(\omega t) \tag{3.1}$$

where H_{AC} is the amplitude of the driving field, and ω is the driving frequency. $\chi = dM/dH$ is the susceptibility as well as the slope of the M(H) curve at very small fields where the magnetization is still reversible (i.e. hysteresis has not yet set in). H_{AC} is usually around 10 Oe where the linear susceptibility assumption is still valid. One advantage of AC susceptibility is that the measurement is very sensitive to small changes in magnetization. Since the AC measurement is sensitive to the slope of M(H), and not to the absolute value, small magnetic shifts can be detected even when the total moment is large.

At higher frequencies, the AC moment of the sample does not follow along the reversible part of the DC magnetization curve due to dynamic effects in the sample. Essentially, the rotation of the magnetic moment cannot keep up with the alternating magnetic field. In this higher frequency case, the magnetization of the sample may lag behind the drive field, an effect that is detected by the PPMS. Thus, the AC magnetic susceptibility measurement yields two quantities: the magnitude of the susceptibility, χ, and the phase shift, ϕ, relative to the drive signal. Alternatively, one can think of the susceptibility as having an in-phase, or real, component $\chi\prime$ and an out-of-phase, or imaginary, component $\chi\prime\prime$. The two representations are related by

$$\chi\prime = \chi \cos\phi \tag{3.2}$$

$$\chi\prime\prime = \chi \sin\phi \tag{3.3}$$

$$\chi = \sqrt{\chi\prime^2 + \chi\prime\prime^2} \tag{3.4}$$

In the limit of low frequency, where the AC measurement is most similar to the DC measurement, the real component $\chi\prime \approx \chi$ as discussed above. The imaginary component, $\chi\prime\prime$, indicates dissipative processes in the sample. In conductive samples, the dissipation is due to eddy currents. In ferromagnets, a nonzero imaginary susceptibility can indicate irreversible domain wall movement, or absorption due to a permanent moment. Also, both $\chi\prime$ and $\chi\prime\prime$ are very sensitive to thermodynamic phase changes, and are often used to measure transition temperatures. In this dissertation, we use the fact that relaxation in superparamagnetic particles gives rise to a nonzero $\chi\prime\prime$.

Graphs of both $\chi\prime$ and $\chi\prime\prime$ show maxima at the blocking temperature for the transition from ferromagnetism to superparamagnetism. Recall that T_B depends on the timescale of the measurement. AC susceptibility is a powerful tool because it uses a timescale where this effect can be clearly seen as a shift in T_B with frequency. The Néel-Arrhenius relation describes the magnetization reversal of a non-interacting single domain particle in a local minimum over an anisotropy barrier, E_a

$$\tau^{-1} = \tau_0^{-1} \exp(E_a/k_B T) \tag{3.5}$$

where τ is the reversal rate, T is the temperature and k_B is Boltzmann's constant. Here, τ_0 is the attempt frequency and is comparable to the Larmor precession frequency [47]. Generally this values falls in the range $10^{-10} - 10^{-9}$s.

By making a plot of $1/T_B$ versus ln (f), the Néel-Arrhenius relation can be used to extract the attempt frequency (y-intercept of the plot) and the anisotropy energy barrier (slope of the plot). However, as mentioned before, this relation is only valid for non-interacting nanoparticle systems, and at times unphysical values of each or both of these parameters may obtained. In that case, the Vogel-Fulcher relation

$$\tau^{-1} = \tau_0^{-1} \exp(E_a/k_B (T - T_0)) \tag{3.6}$$

must be used which accounts for weak (dipolar) interactions between particles by the use of a third parameter, T_0. The result of dipolar interactions is to slow down the magnetic response because the particles must also overcome the local energy present from neighboring particles.

CHAPTER 4

TRANSVERSE SUSCEPTIBILITY

Transverse susceptibility (χ_T) is a measure of the magnetic susceptibility in one direction, while an external magnetic field is applied perpendicular to the direction of measurement. In a seminal 1957 paper [2], Aharoni *et al.* calculated χ_T as a function of H_{DC} for a collection of Stoner-Wohlfarth particles [86]. These are ellipsoid, single domain, ferromagnetic particles with uniaxial anisotropy. According to Aharoni's theory, measurement of χ_T with respect to H_{DC} applied along the hard axis of magnetization should yield peaks at the positive and negative anisotropy fields, $\pm H_K$. The anisotropy field of a material is the field needed to saturate the magnetization of a material in the hard direction and is related to the effective anisotropy K_{eff} via the following:

$$H_K = 2K_{\text{eff}}/M_S \tag{4.1}$$

Thus it can already be seen that directly measuring the anisotropy field of a materials gives valuable information about the effective anisotropy of a sample.

4.1 Theory and Historical Background

Transverse susceptibility along with the parallel susceptibility are actually the diagonal components of the 3×3 reversible susceptibility tensor. The parallel susceptibility is the susceptibility as a function of H_{DC} measured in the direction of the applied field, and the transverse susceptibility components correspond to the susceptibility with H_{DC} applied along either of the two directions transverse to the measurement. For H_{DC} along the

z-direction, the transverse susceptibility is written as

$$\chi_T = \left(\frac{dM_x}{dH_z}\right)_{H_x=0}, \quad H_y = 0 \tag{4.2}$$

Expressing susceptibility as a second rank tensor allows for the response of a sample to be measured in a direction different from the field. As a result, two fields are required to do a transverse susceptibility measurement: a small AC magnetic field (H_{AC}), for which variation with sample magnetization can be related to the susceptibility, and an external DC magnetic field (H_{DC}) that can be varied over a large range. Figure 4.1 shows the geometry involved in a transverse susceptibility measurement.

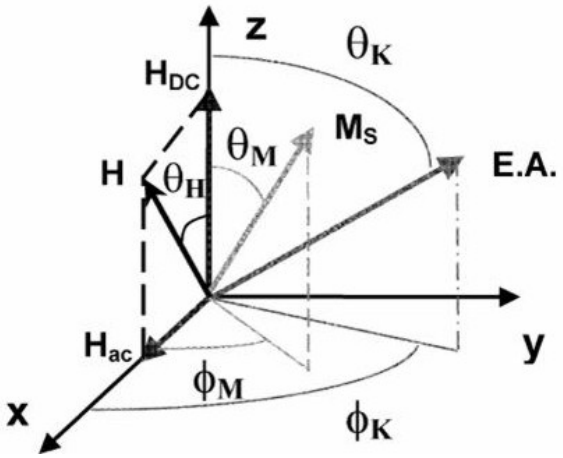

Figure 4.1. Geometrical construct of a transverse susceptibility measurement including the DC field (H_{DC}), the AC field (H_{AC}), the magnetization vector M, and the easy axis (E.A.). Also included are the relevant angles used in the transverse susceptibility calculation. Figure adapted from reference [81].

Here, the axis of anisotropy, K, is denoted E.A. (for easy axis), and defined by the spherical polar angles θ_K and ϕ_K. Similarly, the magnetization vector, M, has coordinates θ_M and ϕ_M. The applied field H_{DC} is aligned along the z-axis. Choosing the coordinate system so that

$$\phi_H = 0$$

then

$$H_x = H \sin\theta_H$$

$$H_z = H \cos\theta_H$$

$$M_x = M_S \sin\theta_M \cos\phi_M$$

Using the expression for χ_T (equation 4.2) it follows that

$$\chi_T = \frac{3}{2}\chi_0 \lim_{\theta_K \to 0} \frac{d(\sin\theta_M \cos\phi_M)}{d(H \sin\theta_H)} \tag{4.3}$$

where $\chi_0 = M_s^2/3K$. For the magnetic moment to lie in an energy minimum, it is necessary to impose the following conditions:

$$\frac{\delta E}{\delta \theta_M} = 0, \quad \frac{\delta E}{\delta \phi_M} = 0 \tag{4.4}$$

For a Stoner-Wohlfarth particle, the energy is given by the sum of the anisotropy energy and the energy of interaction with the applied magnetic field (Zeeman energy) [86]

$$E = E_K + E_H \tag{4.5}$$

In terms of the spherical coordinate system defined above, equation 4.5 becomes

$$\begin{aligned} E = &- K(\sin\theta_K \cos\phi_K \sin\theta_M \cos\phi_M \\ &+ \sin\theta_K \sin\phi_K \sin\theta_M \sin\phi_M + \cos\theta_K \cos\theta_M)^2 \\ &- HM_S(\sin\theta_H \sin\theta_M \cos\phi_M + \cos\theta_H \cos\theta_M) \\ &- HM_S \cos\theta_M \end{aligned} \tag{4.6}$$

Using these expressions, Aharoni *et al.* [2] arrived at the expression for the field-dependent transverse susceptibility of a single Stoner-Wohlfarth particle by minimizing equation 4.6

using the constraints given by equation 4.4

$$\chi_T = \frac{3}{2}\chi_0 \left(\cos^2 \phi_K \frac{\cos^2 \theta_M}{h \cos \theta_M + \cos 2(\theta_M - \theta_K)} + \sin^2 \frac{\sin(\theta_K - \theta_M)}{h \sin \theta_K} \right) \tag{4.7}$$

where h is the reduced field, H_K/H_{DC}.

For an array of particles with randomly oriented anisotropy axes, assuming the particles are identical and that inter-particle interactions are negligible, the average χ_T becomes

$$\bar{\chi_T} = (1/2\pi) \int_0^{2\pi} \int_0^{\pi/2} \chi_T \sin \theta_K d\theta_K d\phi_K \tag{4.8}$$

After integrating over ϕ_K and substituting back equation 4.7, we arrive at the expression

$$\bar{\chi_T} = \frac{3}{4}\chi_0 \int_0^{\pi/2} \left[\frac{\cos^2 \theta_M}{h \cos \theta_M + \cos 2(\theta_K - \theta_M)} + \frac{\sin(\theta_K - \theta_M)}{h \sin \theta_K} \right] \sin \theta_K d\theta_K \tag{4.9}$$

Using this relation, along with the one for the parallel susceptibility

$$\bar{\chi_P} = \frac{3}{2}\chi_0 \int_0^{\pi/2} \left[\frac{\sin^2 \theta \sin \theta_K}{h \cos \theta + \cos 2(\theta - \theta_K)} \right] d\theta_K \tag{4.10}$$

Aharoni *et al.* calculated several values of χ_T and χ_P for various values of reduced field (h), and made a plot of how χ_T and χ_P should behave after reducing the field from saturation (figure 4.2). They predicted that χ_P should diverge at the switching field, H_S, and that χ_T should show three cusps: two at the positive and negative H_K values, and one at H_S. The shape of the transverse susceptibility curve is heavily influenced by those particles whose easy axis is aligned at 90° to H_{DC}.

The first experimental confirmation of this theory was in 1987 by Pareti and Turilli [63] who showed the presence of the peaks at $\pm H_K$ and H_S. Their experiment, on barium ferrite particles, resulted in peaks rather than cusps. This was attributed to the inhomogeneities in particle shape and dimensions resulting in distributions of H_K and H_S.

Over the years, transverse susceptibility has attracted experimental interest largely from the magnetic storage community, who have measured transverse susceptibility on

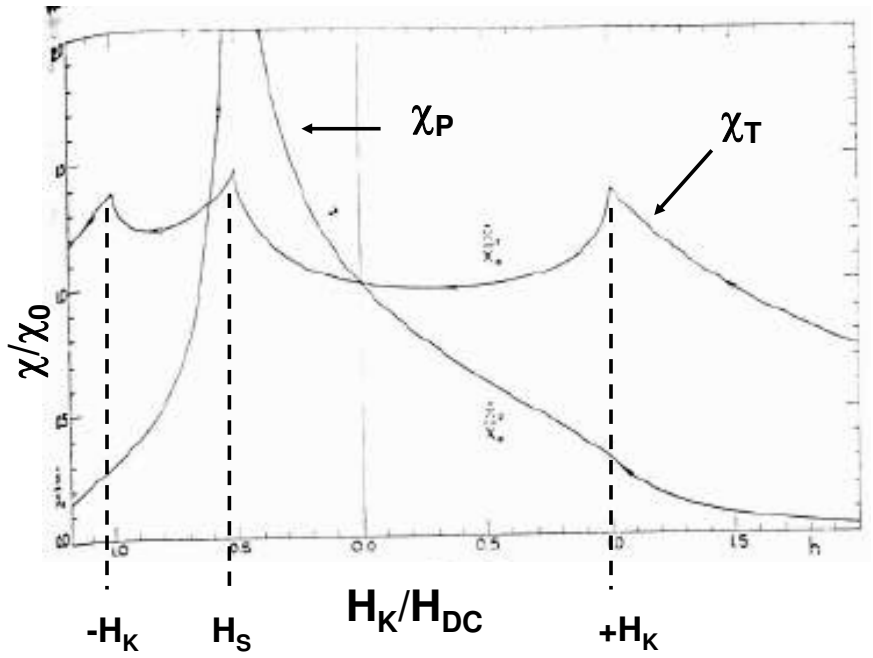

Figure 4.2. Theoretical transverse susceptibility (χ_T) and parallel susceptibility (χ_P) curves as a function of reduced field h (h = H_K/H_{DC}) as calculated by Aharoni *et al.* Figure adapted from reference [2].

particulate recording media [31, 69, 13]. The performance of magnetic media is heavily dependent on the anisotropic properties, and transverse susceptibility as a direct probe of H_K has become an invaluable tool for assessing new materials.

However, due to the limiting assumptions of the Stoner-Wohlfarth model, some modifications have been made to Aharoni's original theory. Notably, Hoare *et al.* [31] added a weighted anisotropy axis distribution function to account for textured media, i.e. 2-dimensional arrays of particles that are preferentially aligned with their easy axes in the plane of the array, an addition useful for recording tape.

A big advance in transverse susceptibility theory was made by Spinu *et al.* [82] when they were able to use micromagnetic simulations to model transverse susceptibility using the Landau-Lifshitz-Gilbert approach, which allowed them to account for the second order anisotropy constant (K_2). For many materials, the value of K_2 is appreciable or even negative (as is the case for Co), and neglecting this term can lead to inaccuracy in K_1. Later,

the LLG approach was used by Stancu and Spinu to calculate the transverse susceptibility for a single domain particle with cubic anisotropy [85].

In 2006, Matarranz *et al.* [51] returned to the Stoner-Wohlfarth model in a bid to incorporate inter-particle interactions into transverse susceptibility theory. Like Hoare *et al.* [31], they too tried to account for particle texturing by introducing a double-Gaussian distribution function of easy axes. To model the dipolar interactions, they used the mean-field model replacing the reduced field h (recall $\mathrm{h} = \mathrm{H}_K/\mathrm{H}_{DC}$) by $h_{\mathrm{eff}} = h + \epsilon m$. Here $\mathrm{m} = \mathrm{M}/\mathrm{M}_S$ is the reduced magnetization, and ϵ is an inter-particle interaction parameter. The most important thing about this modification of the Stoner-Wohlfarth model is the ability to reproduce some of the features seen in physical nanoparticle transverse susceptibility measurements such as broadened peaks located asymmetrically around $\mathrm{H}_{DC} = 0$, the merging of the H_S peak with the -H_K peak, and a prominent asymmetry in peak heights. The experimental existence of these phenomena will be addressed in the next section.

In the past few years, focus in transverse susceptibility theory has turned to the complex transverse susceptibility [16, 15, 36]. Like traditional AC susceptibility, transverse susceptibility also has an out-of-phase component. An analysis of the in-phase and out-of-phase transverse susceptibility, undertaken by Papusoi [36] in 2000, revealed some very important conclusions about complex transverse susceptibility. First, when the DC field is decreased from H_K down to zero, the particle relaxation time distribution shifts from zero to very high values. In the DC field range where the particle relaxation time becomes of the same order of magnitude as the reciprocal of the AC field frequency, the transverse susceptibility is strongly influenced by the particle volume distribution. This implies that the H_{DC} in complex transverse susceptibility measurements plays an analogous role to the temperature in AC susceptibility measurements. This work prompted Cimpoesu *et al.* [16, 15] to develop a micromagnetic model that accounts for the frequency of the perturbing AC field, which until then had been neglected. It was found that the complex transverse susceptibility with respect to H_{DC} contains multiple peaks, which can be correlated with anisotropy and volume distributions.

Finally, in 2006, it was reported that a new transverse susceptibility theory based on magnetization vector dynamics as described by the Landau-Lifshitz equation of motion led to the conclusion that what we measure as transverse susceptibility is actually the zero frequency limit of ferromagnetic resonance [78].

It can easily be said that the widespread use of micromagnetic simulations with better and faster computers in recent years has allowed transverse susceptibility theory to evolve from the simplified view of Aharoni over 50 years ago to a sophisticated series of calculations used to gain invaluable information on the anisotropy of magnetic materials, and explain the rich variety of behavior observed in physical transverse susceptibility measurements.

4.2 Measuring the Transverse Susceptibility Using a Tunnel Diode Oscillator

All of the transverse susceptibility data presented in this dissertation were taken not with a traditional susceptometer, but with a self-resonant tunnel diode oscillator (TDO). Resonant methods have the advantage of precision and high sensitivity when it comes to detecting changes in the physical properties of materials as a function of temperature and magnetic field. This is due to the fact that frequency can be measured with a high degree of accuracy. In a typical resonant technique based on an LC tank circuit, the capacitor or inductor couples to the material under study, and acts as a transducer of physical parameters. Any change in material properties will induce a change in the capacitance or inductance, which in turn results in a shift in the resonant frequency. Thus, measurement of the frequency shift translates to directly probing the electronic, dielectric, or magnetic response of the material to the oscillating signal. Tunnel diode oscillators which operate based on this principle have been used in the past to study a wide variety of material properties [83].

The principle of the TDO can be explained as follows. An LC tank circuit is maintained at a constant amplitude resonance by supplying the circuit with external power to compensate for dissipation. This power is provided by a tunnel diode that is forward-biased with a voltage in the region of negative slope of its current-voltage (I-V) curve, or

"negative resistance region". Such an arrangement makes it a self-resonant circuit as the power supplied by the diode maintains continuous oscillation of the LC tank operating at a frequency given by the expression

$$\omega = \frac{1}{\sqrt{LC}} \tag{4.11}$$

When a sample is inserted into the oscillator tank coil, there is a small change in the coil inductance ΔL. If ΔL/L <<1, one can differentiate equation 4.11 and obtain the expression

$$\frac{\Delta\omega}{\omega} \approx -\frac{\Delta L}{2L} \tag{4.12}$$

The inductance change is related to material properties. In the case of a magnetic material, this is proportional to the real part, $\mu\prime$, of the complex permeability

$$\mu = \mu' - i\mu'' \tag{4.13}$$

The inductance coil in this experimental setup serves as the sample space in which a gel cap containing the sample can fit. This entire coil is inserted into the sample chamber of our PPMS using a customized radio frequency (RF) co-axial probe (figure 4.3). The DC magnetic field (H_{DC}) is varied using the PPMS. The oscillating RF field, H_{RF}, produced by the RF current flowing in the coil windings, is oriented perpendicular to H_{DC}, and this arrangement sets up the transverse geometry described in the previous section. When H_{RF} is perpendicular to the varying H_{DC}, the change in inductance is actually determined by the change in transverse permeability, μ_T, of the sample. Thus, we can derive an absolute value for the transverse susceptibility:

$$\chi_T = \mu_T - 1 \tag{4.14}$$

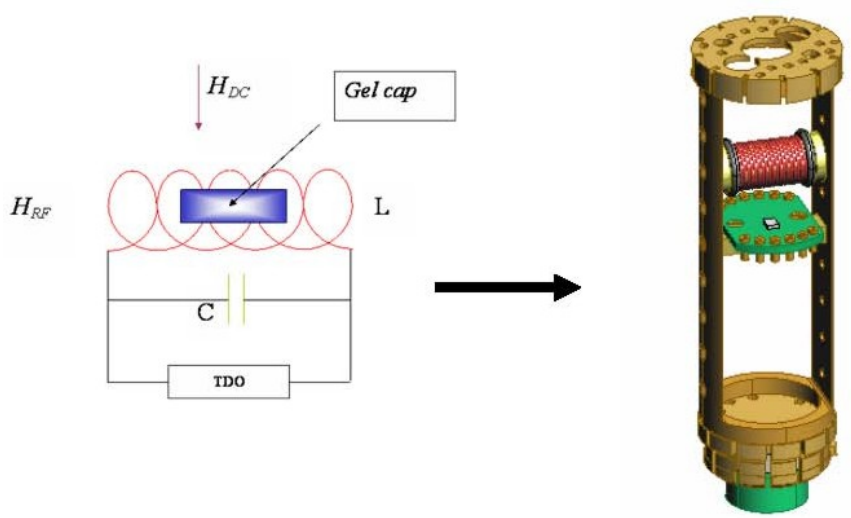

Figure 4.3. Schematic of the TDO circuit and sample space (left) and CAD drawing of the inductance coil which serves as the sample holder (right).

The percent change in transverse susceptibility then can be defined as

$$\frac{\Delta\chi_T}{\chi_T}(\%) = \frac{|\Delta\chi_T(H) - \chi_T^{sat}|}{\chi_T^{sat}} \times 100 \tag{4.15}$$

where χ_T^{sat} is the transverse susceptibility at the saturating field H_{sat}. This quantity, which represents a figure of merit, does not depend on geometrical parameters and is useful for comparing the transverse susceptibility data for different samples, or for the same sample under different conditions. Despite the fact that this technique only gives you the percent change in transverse susceptibility, the most important features of transverse susceptibility with respect to temperature, namely the $\pm H_K$ and H_S peaks, are still present, which allow us to draw important conclusions about the sample's anisotropy. Moreover, since this is a resonant method, we are able to use the high degree of sensitivity ($\delta\chi \approx 10$ Hz in 10 Mhz) to look at very small samples that often times do not have a high enough moment to be picked up by the magnetometer in the PPMS. This feature will be highlighted in chapter 5, where we discuss the use of the TDO method to sense nanoparticles inside of human cells.

Figure 4.4 is a sample transverse susceptibility scan of $NiFe_2O_4$ nanoparticles taken from positive saturation to negative saturation. Henceforth, this type of scan will be referred to as a unipolar scan, and one going from positive to negative saturation and then back to positive will be referred to as a bipolar scan. Figure 4.5 is a detailed view of a bipolar scan of the same $NiFe_2O_4$ sample. The arrows correspond to the measurement sequence so that the sets of peaks arising from the positive to negative scan can be easily distinguished from the negative to positive scan. A couple of features can be seen in these figures that are different from Aharoni's theoretical curve (figure 4.2). First, there are peaks seen at the anisotropy fields, but in this case $+H_K \neq -H_K$. In the unipolar scan, the $+H_K$ value is 365 Oe and the $-H_K$ value is -390 Oe. In other nanoparticle systems, the two H_K values can diverge by quite a bit more, as will be seen in chapters 5 and 6, and indeed in the bipolar scan, the disparity is a little more apparent. In almost every case, the peak closest to saturation has a smaller H_K value than the one that occurs after passing through $H = 0$. Second, there is no peak corresponding to H_S. Lastly, there is a difference in peak height between $+H_K$ and $-H_K$, with the peaks nearest to saturation being higher in amplitude. Thus, $+H_K$ is higher in amplitude and smaller in value, and $-H_K$ is smaller in amplitude and larger in value coming from positive saturation going to negative saturation. Conversely, from negative saturation, the $-H_K$ peak is higher in amplitude and smaller in value, while the $+H_K$ peak is smaller in amplitude and larger in value. For the remainder of this dissertation, we will distinguish the two sets of peaks with the terminology H_{K1} and H_{K2}, where H_{K1} is always the first peak that occurs after saturation in either direction. Note that $|H_{K1}| < |H_{K2}|$. Also, it should be explicitly clarified that the subscripts K1 and K2 refer only to the locations of the anisotropy peaks, and do not correspond specifically to the first and second anisotropy constants.

The features in the physical transverse susceptibility graphs that deviate from the theoretical curve calculated by Aharoni *et al.* actually show some resemblance to the curves theorized by Matarranz *et al.* [51]. Their paper postulated that particle size dispersion, inter-particle interactions, and texturing all contribute to the phenomena, and this is mod-

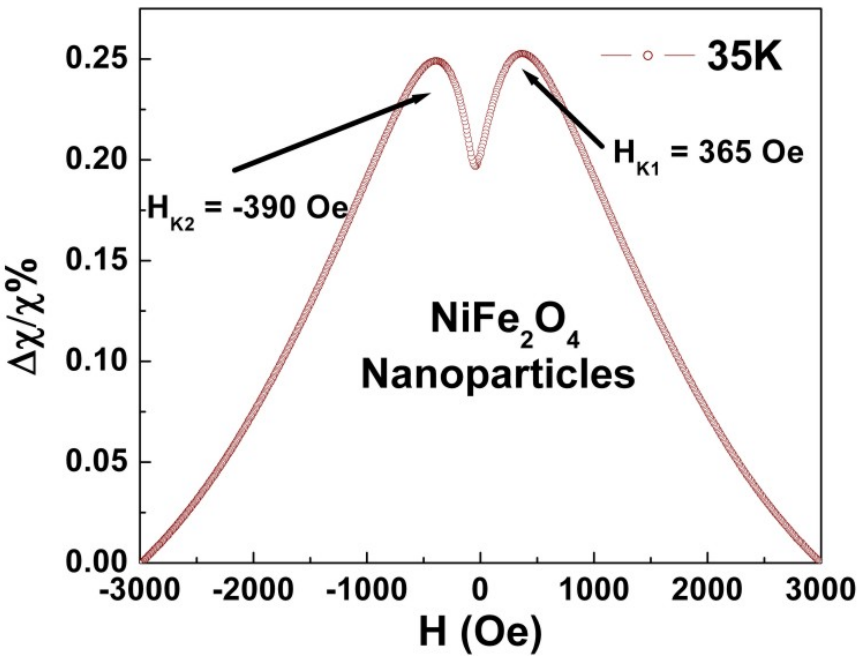

Figure 4.4. Unipolar transverse susceptibility scan (from positive saturation to negative saturation) of $NiFe_2O_4$ nanoparticles.

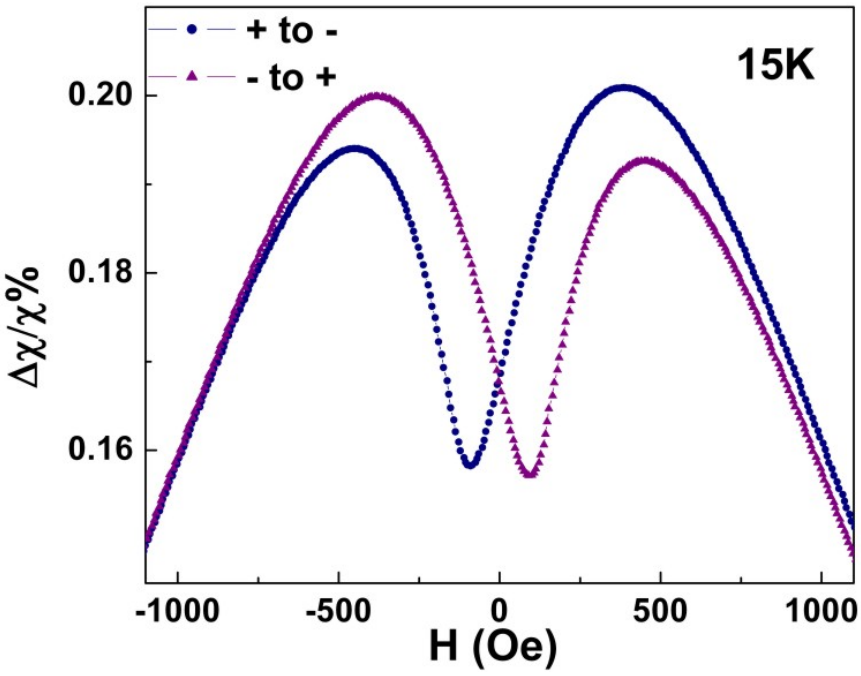

Figure 4.5. Detailed bipolar transverse susceptibility scan (from positive to negative saturation and back to positive saturation) of $NiFe_2O_4$ nanoparticles.

eled by introducing an orientation distribution function and a modified reduced field. While none of the nanoparticles we measured should possess texturing (i.e. the moments are completely randomly aligned), size dispersion and inter-particle interactions should both have important contributions to transverse susceptibility measurements. Size dispersion, which also will lead to an H_K dispersion, can explain why we see peaks instead of the cusps seen in figure 4.2.

When it comes to inter-particle interactions, we feel that qualitatively the deviations from theory can be explained more effectively by considering the energy landscape of the particles contributing to the transverse susceptibility at different values of H_{DC}. For instance, H_{K1} always occurs after saturation, when the Zeeman energy (the energy associated with the moments aligning with the field) is highest. Since the particles are being heavily influenced by the changing field, the rotation of the moments is more coherent causing a sharper peak with a higher magnitude at H_{K1}. At the transverse susceptibility minimum (occurring after $H = 0$), the moments have essentially randomized and are no longer aligned with the field, consistent with a minimizing of Zeeman energy. At this point, the inter-particle interactions are dominating the magnetic response. Strong interactions should lead to H_{K2} being closer to symmetric with H_{K1}, since the field each particle experiences from its neighbors should have a similar response to an applied field. Thus, minimizing the Zeeman energy should not have as large an effect on the collective response of the system. If the inter-particle interactions are weak, then the overall magnetic response of the particles in the randomized state to an increasing field will be much smaller, leading to peaks with smaller height than those occurring after saturation. We believe that is why in thin films, the peaks are symmetric. We can think of thin films as being the "highly interacting" limit of the picture described above, where instead of dipolar interactions producing a field internal to the system, the exchange interaction between spins causing the crystal field is responsible for the similar behavior on each side of $H = 0$. In nanoparticles, we usually see the complete disappearance of the peak associated with the switching. This is likely due to the dispersion in H_K and H_S associated with a distribution in particle sizes. These

dispersions likely overlap leading to a single, broadened peak which is also consistent with the value of H_{K2} being larger than H_{K1}.

Because of the varying interactions and dispersions in H_K and H_S, the H_{K2} peak can vary greatly in height and field value. For these reasons, K_{eff} is always calculated using $H_K = H_{K1}$, though often both H_K values will be plotted versus temperature to examine the anisotropy evolution in a material. And finally, when the K_{eff} values are calculated from transverse susceptibility using equation 4.1, we are actually calculating K_1. In chapter 2 the anisotropy energy was often expressed as a series expansion, where only the first two terms were used containing the first and second order anisotropy constants. In calculating K_{eff}, we are neglecting the second order and higher terms, keeping only K_1. While K_2 is non-negligible and even negative in some materials, we have found that for our purposes, namely probing nanoparticles dominated by uniaxial anisotropy and surface effects, calculating K_1 only captures the main physics of the systems to a satisfactory degree.

CHAPTER 5

Fe_3O_4 AND Au-Fe_3O_4 NANOPARTICLES FOR BIOMEDICAL APPLICATIONS

In the spring of 2006, the author was awarded a National Science Foundation Integrative Graduate Education Research and Traineeship (IGERT) fellowship. The IGERT program was developed to educate Ph.D. scientists with interdisciplinary backgrounds, deeper knowledge in chosen disciplines, and technical, professional, and personal skills to meet the needs of a changing scientific landscape. The IGERT research performed by the author was in collaboration with Professor Shyam Mohapatra and Dr. Arun Kumar of the University of South Florida College of Medicine. Prof. Mohapatra and Dr. Kumar have research interests in magnetic nanoparticles for biomedical applications. This research was undertaken in order to help characterize, as well as optimize the magnetic properties of the nanoparticles they use for cell transfection, in line with the goals of the IGERT program.

5.1 Introduction

In recent years, magnetic nanoparticles have become a topic of interest for a wide range of medical applications due to their dimensions being smaller than or comparable to several biological entities such as cells (10-100 μm), viruses (20-450 nm), and proteins (5-50 nm) [62]. The ability of magnetic particles to be manipulated by an external magnetic field make them especially attractive for localized treatment options such as targeted drug delivery and hyperthermia, as well as diagnostics like enhancing existing MRI techniques and sensors based on the detection of a magnetic signal. In this section, we describe these treatment and diagnostic applications, as well as propose how transverse susceptibility

could be used for cancer cell detection. The rest of the chapter describes the magnetic properties of Fe_3O_4 and Au-Fe_3O_4 particles synthesized specifically for these applications.

5.1.1 Targeted Drug Delivery

The biggest problem associated with systemic drug administration is that a pharmaceutical becomes evenly distributed throughout the body, which results in a lack of specificity for the area of interest [7]. Therefore, high levels of a drug must be administered to achieve the desired concentration in the afflicted area. Both non-specificity and the toxic levels needed to treat illness often lead to unwanted and harmful side-affects. No where is this currently more evident than in chemotherapy, where significant damage is done to the entire body in the hopes of killing often localized cancer cells.

Targeted drug delivery aims to alleviate these issues by immobilizing a drug onto a biocompatible magnetic nanoparticle, which acts as a carrier. The drug/carrier complexes, which are usually in the form of a suspension of nanoparticles (ferrofluid) in a biocompatible liquid, can be injected into the patient via the circulatory system. After the particles enter the bloodstream, external, high-gradient magnetic fields can be used to concentrate the complex at a specific target site within the body. Once the drug/carrier is concentrated at the target, the drug can be released either via enzymatic activity, or changes in physiological conditions such as pH, osmolality, or temperature.

Fe_3O_4 superparamagnetic nanoparticles have been examined for targeted drug delivery due to their biocompatibility, magnetic properties (high saturation magnetization), and their ability to be functionalized [25, 24, 58]. However, if the surface is left untreated, agglomeration can occur, and the natural hydrophobicity of the surface causes the particles to be taken up by the body's systems, mainly the kupffer cells in the liver [25]. Usually, Fe_3O_4 particles must first be coated with an amphiphilic polymeric surfactant such as poly(ethylene glycol) (PEG) to keep them from agglomerating, and to minimize unwanted protein adsorption onto nanoparticles. The subsequent coating can then be functionalized by attaching carboxyl groups or other molecules.

Coating the Fe_3O_4 particles with a noble metal, such as gold (Au), can serve a similar purpose, but in this case "linker" molecules with functionalities at both ends and an affinity for Au can be used to aid in functionalization. A well-known example is thiol adsorption, in which alkanedithiols are covalently attached to the Au surface [56]. This opens up a greater realm of possibilities as thiols can be bonded with proteins, peptides, carbohydrates, lipids, and DNA [49]. It is widely thought that greater functionality of Fe_3O_4 nanoparticles can be achieved through coating them with Au and exploiting Au-thiol chemistry.

5.1.2 Hyperthermia Treatment for Malignant Cells

The preferential killing of cancer cells without damaging normal tissue has been one of the main goals of cancer therapy for many years [7]. The potential of hyperthermia (localized heating) as a treatment for cancer was first predicted following observations that several types of cancer cells were more sensitive to temperatures in excess of 41°C than their normal counterparts [35]. The use of magnetic nanoparticles for hyperthermia involves dispersing the particles throughout the target tissue, and then applying an AC magnetic field of sufficient amplitude and frequency to cause the particles to heat. This heat conducts into the immediately surrounding diseased tissue whereby, if the temperature can be maintained at the threshold of 41°C for 30 minutes or more, the cancerous cell is destroyed. Magnetic nanoparticles in a suspension can be heated via four different mechanisms: Brownian rotation, Néel relaxation losses, eddy current losses (if the particle is also conducting), and hysteretic losses. No matter what type(s) of losses contribute to the heating, it has been suggested that the product of the frequency and magnitude of the applied field not exceed $\mathbf{H}f = 6 \times 10^6$ Oe Hz [5].

Brownian rotation and Néel relaxation losses both occur as a consequence of a magnetic particle exposed to an AC magnetic field. Brownian rotation refers to the physical rotation of the particle in suspension and depends on the particle size and viscosity of the fluid. It is the dominant mode of relaxation at lower frequencies (f in the kHz range). Néel relaxation refers to the movement of the magnetic moment in response to the magnetic

field and dominates at higher frequencies. Both types of relaxation can be probed by AC susceptibility measurements (section 2.2). Generally, the use of frequencies in the range $f = 0.05 - 1.2$ MHz is considered safe for humans [62], so in principle both relaxation modes could be used to contribute to heating.

If the magnetic particle is also conducting, eddy currents can form within the particle, and contribute inductive heating. However, Fe_3O_4, which is an insulator, has been looked at the most for hyperthermia because the magnetic properties and biocompatibility far outweigh the benefits of heating via eddy currents in hyperthermia. Metallic nanoparticles, such as Fe, are often toxic and highly pyrophoric, and special care needs to be taken to safely coat the surface. Using an already safe material with high saturation magnetization, like Fe_3O_4, and coating it with Au as proposed in the previous subsection, would aid in hyperthermia applications as well because the Fe_3O_4 could contribute Brownian and Néel losses, while eddy currents are generated on the Au surface, adding to the overall heating ability of the particles.

Thus far, we have assumed that the magnetic nanoparticles in suspension are superparamagnetic to avoid agglomeration, and aid in easier passage through the cell membrane. Largely, superparamagnetic particles are preferred because they stay in suspension, thus allowing easier manipulation to the specific site. However, once the particles have been taken up by a tumor cell and an AC magnetic field has been applied, this is no longer an issue. In fact, a particle that is superparamagnetic at room temperature and in DC fields but acquires a coercivity in an AC field would be very beneficial for hyperthermia. The amount of heat generated per unit volume is given by the frequency multiplied by the area of the hysteresis loop:

$$P_{FM} = \mu_0 f \oint \mathbf{H} d\mathbf{M} \tag{5.1}$$

Recently, Eggeman *et al.* [17] studied the size and concentration effects of iron oxide nanoparticles that exhibited hysteresis at higher frequencies, and found that hysteretic losses in these particles are significant. Therefore, being able to tune the blocking tem-

perature and blocking frequency to optimize functionality and hysteretic losses is a viable route to improving properties for hyperthermia.

5.1.3 MRI Contrast Enhancement

Magnetic resonance imaging (MRI) is currently one of the most common imaging techniques for soft tissue structure of the musculoskeletal system. In brief, it measures changes in the magnetization of hydrogen protons in water molecules sitting in a magnetic field after a pulse of radio frequency with H_{AC} perpendicular to H_{DC} is propagated through the sample. Protons from different tissue react differently, giving a picture of the anatomical structures. These images can be enhanced by adding contrast agents, which sharpen the contrast by affecting the behavior of the protons in their vicinity. In standard clinical MRI scans, contrast agents travel through the bloodstream and tissues, increasing contrast everywhere. The most commonly used MRI contrast media are gadolinium chelates, which tend to be non-specific with rapid accumulation in the liver and only allow a short window for imaging.

Dextran-coated superparamagnetic iron oxide nanoparticles for MRI enhancement are becoming increasingly common. They are selectively taken up by reticuloendothelial system, the cells that line blood vessels, whose function is to remove foreign substances from the bloodstream. Nanoparticles used for MRI contrast enhancement rely on the differential uptake of anatomical regions, and nanoparticle size plays a significant role in which cells selectively uptake them. Larger particles ($d > 30$ nm) are taken up by the liver and spleen, smaller particles ($d < 10$ nm) are not easily detected and propagate through the bloodstream and reticuloendothelial cells, including bone marrow and lymph nodes. Small particles can also be used to image the vascular system and central nervous system.

5.1.4 Transverse Susceptibility as a Biosensor

One can think of any number of ways to use an external field to sense cells that have taken up nanoparticles. Recently, the large change in magnetoimpedance of amorphous

magnetic ribbons was used to detect the presence of cells loaded with magnetic nanoparticles. This method, in which the impedance of a magnetic conductor changes with H_{DC}, relies on the fringe fields associated with the magnetic nanoparticles inside the cells to give a change in magnetoimpedance from the normal response exhibited by the ribbons [40]. We proposed that transverse susceptibility may be used to sense particles that have been taken up by cells as well. Recall that this technique is highly sensitive for two distinct reasons: any susceptibility measurement is a measure of the derivative of the magnetic response with respect to field, and our method of measurement is a resonant technique which can detect changes in frequency on the order of 10 Hz in 10 MHz. Therefore, it is possible that even a small sample of cells that have taken up nanoparticles when placed inside the sample space of the transverse susceptibility probe could yield a signal characteristic of the magnetic nanoparticles.

5.2 Nanoparticle Synthesis

Both Fe_3O_4 nanoparticles and Au-coated Fe_3O_4 were synthesized at the University of South Florida College of Medicine by Dr. Arun Kumar following the procedure outlined by Mandal *et al.* [49] using a micellar method. First, a stock solution was made by dissolving ferric ammonium sulfate (0.128 M with respect to the Fe(III) ion) and ferrous ammonium sulfate (0.064 M with respect to the Fe(II) ion) in 100 ml 0.40 M aqueous sulfuric acid. A separate solution of 1.0 M NaOH was added to 0.01 M poly(oxyethylene) isooctyl phenyl ether (TX-100) to make a concentration of 0.01 M TX-100. Of this solution, 25ml was added drop by drop to 0.01M TX-100. This solution was heated to 70-80°C, and 25 ml of the iron stock solution was added drop by drop while stirring. Heating and stirring continued for 30 minutes while Fe_3O_4 nanoparticles were formed. The particles were centrifuged to separate them from solution and washed. The resulting Fe_3O_4 particle sizes were measured using TEM and found to have an average diameter of 60 nm with a moderate size dispersion. This size of particle is desirable because the cells to be used in this experiment preferentially

take up particles of 60-70 nm. The static and dynamic magnetic properties of the Fe_3O_4 particles were studied and are presented in the next section.

The procedure outlined above was followed to obtain the Fe_3O_4 particles, which were then coated with gold. For this step 0.5 g of glucose was added to a solution of 1:1 molar ratio Fe_3O_4 to $HAuCl_4$. The solution was sonicated for 15 minutes and then heated in a water bath for 1 hour. Mandal *et al.* reported in reference [49] that the glucose helps promote Au-Fe_3O_4 adhesion and maintain Au thickness uniformity. The magnetic properties of the Au-Fe_3O_4 particles were also studied and presented in the following section. Due to the dual functionality of the Au and Fe_3O_4, these particles were chosen for cell transfection, and subsequently tested for detection using transverse susceptibility.

5.3 DC Magnetic Properties of Fe_3O_4 and Au-Fe_3O_4 Nanoparticles

5.3.1 Fe_3O_4 Nanoparticles

Zero field cooled and field cooled curves were taken of the Fe_3O_4 particles in an external field of 100 Oe (figure 5.1). The ZFC curve is consistent with a polydisperse sample of nanoparticles, with a broad blocking temperature (T_B) that occurs around 267K. This temperature matches well with that reported by Goya *et al.* [22] for 50 nm Fe_3O_4 particles. They also report a bump in the ZFC curve at 16K, which they attribute to the Verway transition, a well-studied structural transition which occurs at 120K in bulk Fe_3O_4. The Verway transition has been shown to be highly temperature dependent in nanoparticles, shifting to lower temperature as the particle diameter decreases until it cannot be seen in particles below about 40 nm [22]. The ZFC curve in figure 5.1 does show a small bump at 16K as well, which re-enforces the notion that these particles are relatively large.

The nearly linear relationship between magnetization and temperature in the ZFC curve indicates that the inter-particle interactions in these particles are strong, which is to be expected since these particles were not coated with a surfactant, so were free to agglomerate. Particles with fewer interactions tend to show a magnetization that rises faster than the increase in temperature, resulting in a more curved zero field cooled magnetization versus

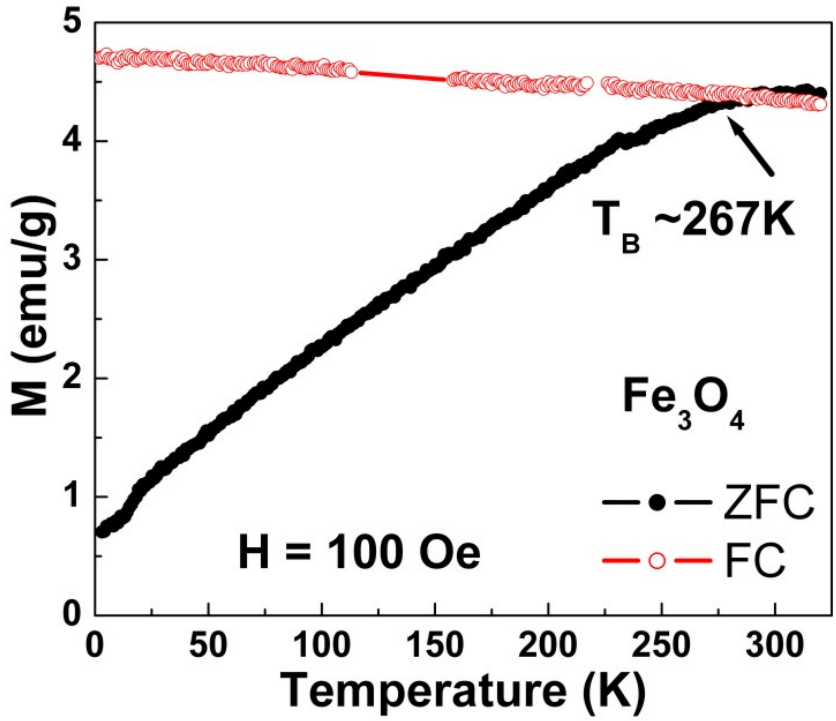

Figure 5.1. Zero field cooled and field cooled curves for Fe_3O_4 particles.

temperature. We also performed DC magnetic measurements on the Fe_3O_4 particles after dispersing them in a paraffin wax matrix to see if that would affect the overall shape of the ZFC and FC curves (figure 5.2). This was done by taking a dry sample of Fe_3O_4 and several pellets of wax in a vial, and sonicating in a hot water bath while the wax melted. This suspended the particles in the wax matrix, and prevented them from agglomerating. Ideally, the inter-particle distance is enough to prevent the particles from experiencing dipolar interactions from their neighbors. The ZFC curve did show better definition with a steeper rise of magnetization, more consistent with non-interacting particles. However, the freezing of residual water in the sample made it very difficult to observe the magnetic behavior right around the blocking temperature.

Figures 5.3 and 5.4 are the 300K and 2K magnetization versus field curves respectively for the Fe_3O_4 powder. The lack of coercivity in the 300K M-H curve confirms that the particles are superparamagnetic at 300K. At 2K, a coercivity is present of 430 Oe.

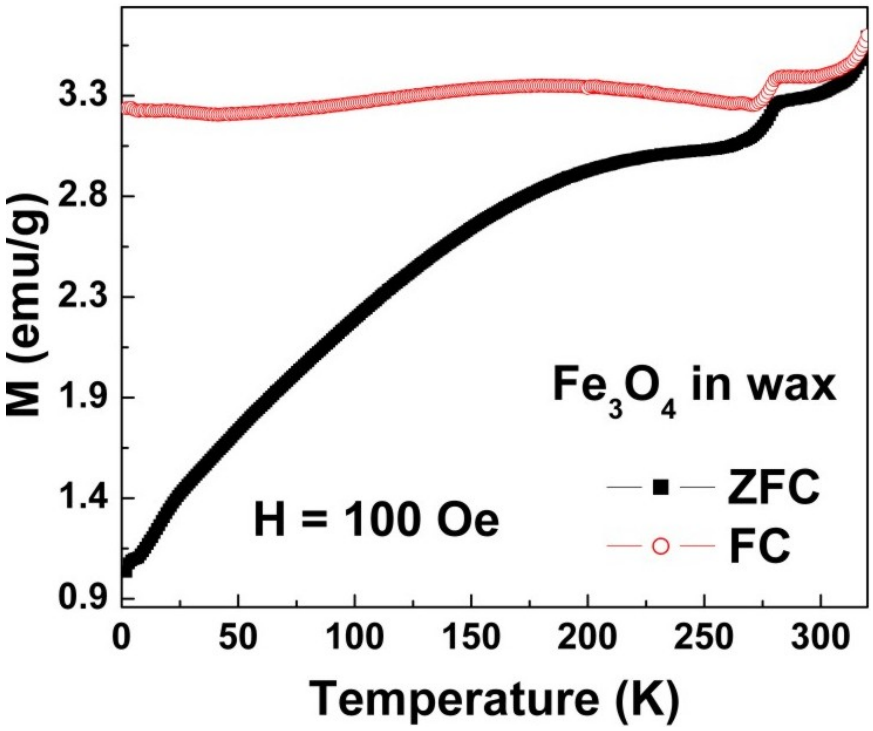

Figure 5.2. Zero field cooled and field cooled curves for Fe_3O_4 nanoparticles suspended in a paraffin wax matrix.

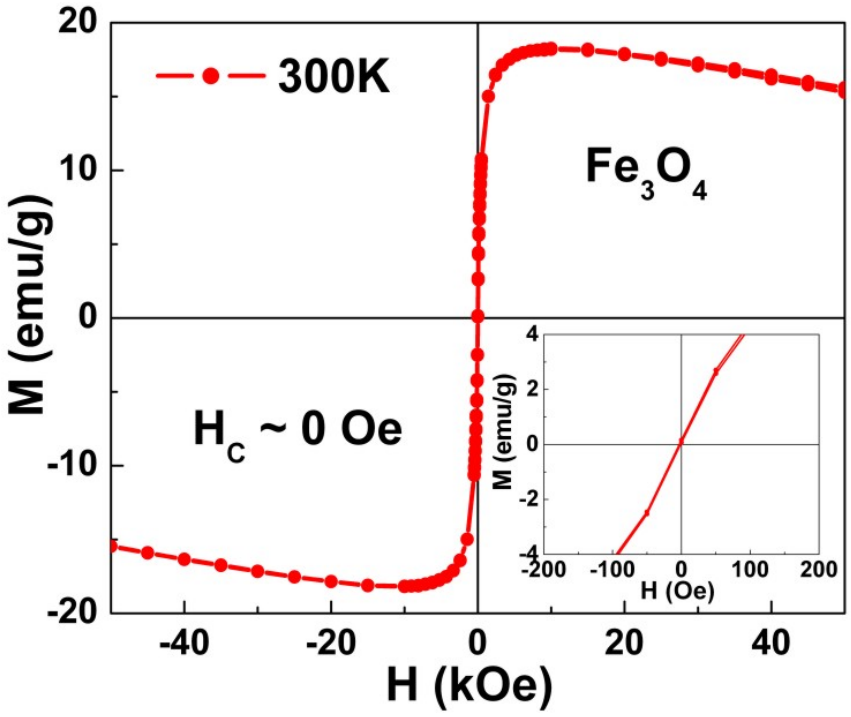

Figure 5.3. Magnetization versus field curve for Fe_3O_4 nanoparticles taken at 300K.

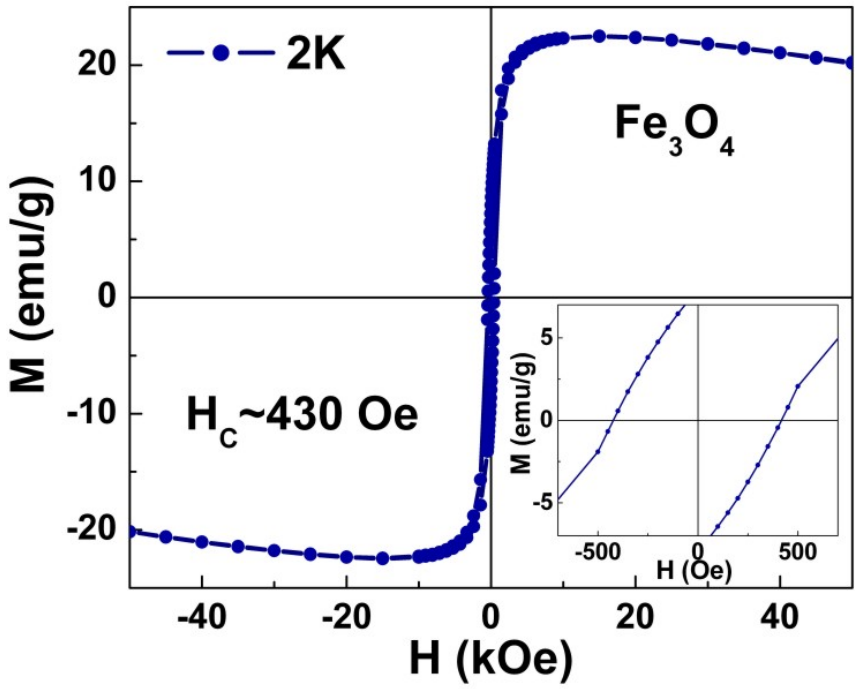

Figure 5.4. Magnetization versus field curve for Fe_3O_4 nanoparticles taken at 2K.

The coercivity of the system of particles will also be affected by inter-particle interactions, so the low temperature M-H curve was repeated after the Fe_3O_4 particles were put into paraffin wax. Indeed, the coercivity was reduced from 430 Oe to 230 Oe indicating that while interactions were present in the case of bare Fe_3O_4 particles, these interactions were greatly reduced or eliminated by placing them in the wax matrix (figure 5.5).

5.3.2 Au-Fe_3O_4 Nanoparticles

DC magnetic measurements were then taken of the Fe_3O_4 particles coated with Au. As can be seen in the ZFC curve (figure 5.6), the approach to the blocking temperature is steeper than for the Fe_3O_4 particles. This is consistent with a less interacting system, which can be expected for the particles coated with Au, as opposed to the bare Fe_3O_4. Indeed, one of the many reasons for coating the Fe_3O_4 with gold is to minimize the inter-particle interactions.

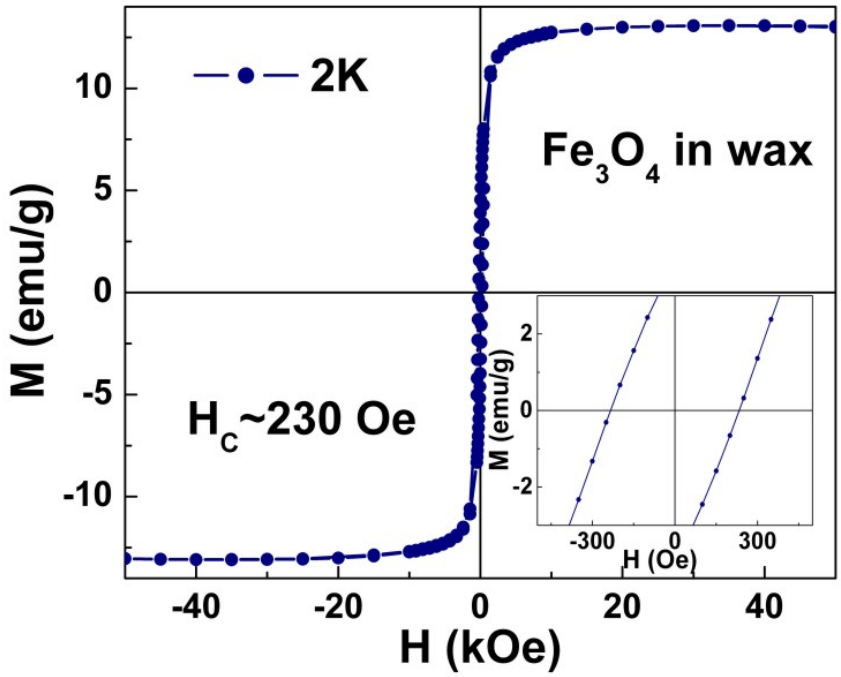

Figure 5.5. Magnetization versus field curve for Fe_3O_4 nanoparticles suspended in paraffin wax taken at 2K.

The blocking temperature for the Au-Fe_3O_4 particles is slightly higher than the Fe_3O_4 samples. This could be due to slight differences in chemical batches, as the two were synthesized on different occasions. In this sample, like the Fe_3O_4, the broad blocking indicates a particle size dispersion. It is likely that both sets of samples have particle size dispersions with the Au-Fe_3O_4 have an average Fe_3O_4 particle size slightly larger than the Fe_3O_4 particles measured in the previous section. The low temperature feature thought to be associated with the Verway transition is present in this sample as well, occurring at 17K rather than 16K.

Like the bare Fe_3O_4 particles, the 300K M-H curves for the Au-Fe_3O_4 particles (figure 5.7) confirm that they are superparamagnetic at room temperature. At 2K, the coercivity is 200 Oe (figure 5.8), lower than the 430 Oe measured for the Fe_3O_4 particles alone, and comparable to the particles suspended in wax. Again, this can be attributed to a decrease in inter-particle interactions. This demonstrates that suspending the particles in wax and simply coating them with a layer of Au achieve the same objective, that is, eliminating

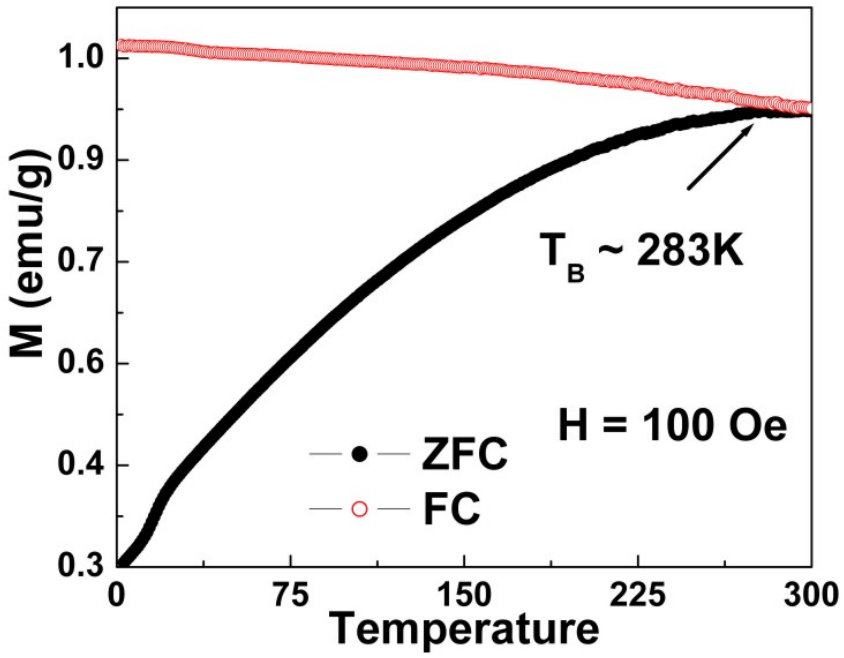

Figure 5.6. Zero field cooled and field cooled curves for Au-Fe_3O_4 nanoparticles.

inter-particle interactions. However, whereas manipulating nanoparticles in a solid matrix is not very useful for biomedical applications, the Au-coated Fe_3O_4 particles retain their versatility by being able to be manipulated while in a biocompatible liquid suspension.

5.4 Transverse Susceptibility Measurements

5.4.1 Fe_3O_4 Nanoparticles

Transverse susceptibility measurements were first performed on the bare Fe_3O_4 particles not in wax suspension. The transverse susceptibility data for these particles show indiscernible features, likely due to the inter-particle interactions. A representative low temperature bipolar scan is shown in figure 5.9. Therefore, in order to make any quantitative observations of the anisotropy of the Fe_3O_4 particles, we limit this discussion to the transverse susceptibility measurements made on Fe_3O_4 nanoparticles suspended in paraffin wax. For this experiment, the same wax sample was used that was presented in section 4.3.1.

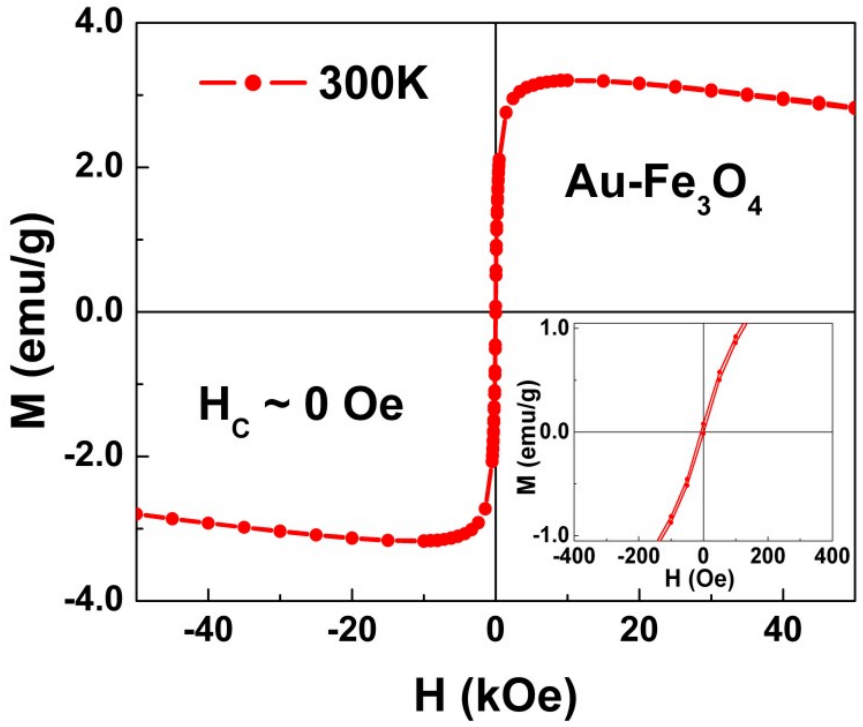

Figure 5.7. Magnetization versus field curve for Au-Fe_3O_4 nanoparticles taken at 300K.

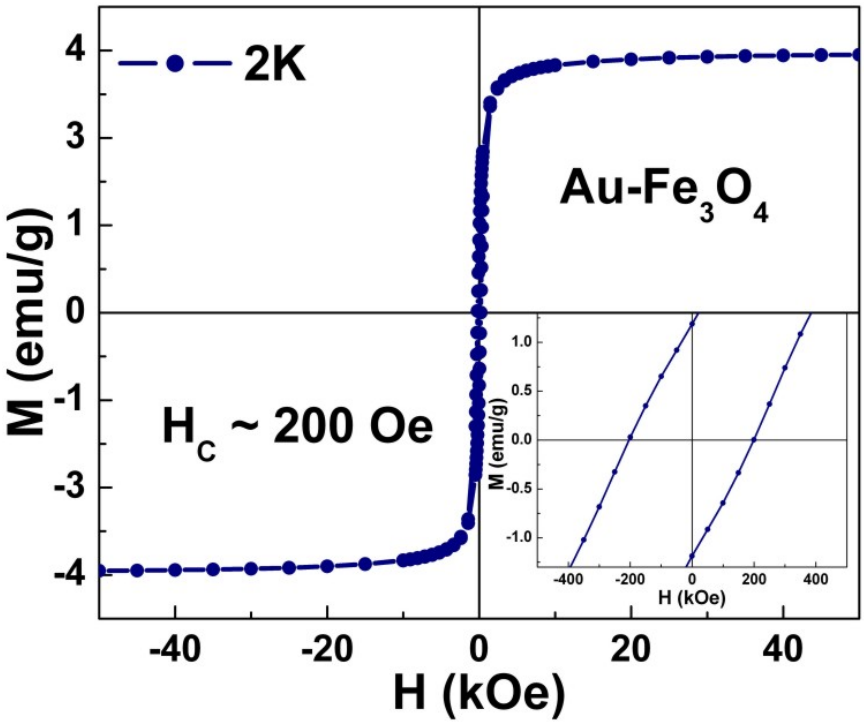

Figure 5.8. Magnetization versus field curve for Au-Fe_3O_4 nanoparticles taken at 2K.

Figure 5.10 shows several unipolar transverse susceptibility scans of the Fe_3O_4 particles in wax. At low temperatures, anisotropy peaks can be seen. As the temperature increases, the peaks shift to lower fields, and eventually merge into a single peak around H = 0, signaling the ferromagnetic to superparamagnetic transition. It can be seen from these graphs that anisotropy peaks are still present at 250K, but the transition is complete by 300K, in agreement with the ZFC curve.

Figure 5.11 is a low field, low temperature, bipolar scan of the particles clearly showing that two different anisotropy peaks, H_{K1} and H_{K2}, are present. Recall that asymmetry in the two anisotropy peaks is common for nanoparticles, and can be correlated with a lack of inter-particle interactions because the H = 0 energy environment is much different than the $H = H^{sat}$ environment for a non-interacting array of particles. Here $H_{K1} \approx 415$ Oe, while $H_{K2} \approx 530$ Oe.

In figure 5.12 we present the low field, room temperature, bipolar transverse susceptibility scan. A distinct lack of anisotropy peaks can be seen. It can be concluded from this scan that at room temperature and 12 MHz nearly all of the Fe_3O_4 particles in the wax matrix are in the superparamagnetic state.

5.4.2 Au-Fe_3O_4 Nanoparticles

In figure 5.13 we present several unipolar transverse susceptibility scans for the Fe_3O_4 particles coated with Au. Again, anisotropy peaks can clearly be made out at the lowest temperatures, with the peaks shifting to smaller fields as the temperature is increased. In this case, there remains a slight ferromagnetic signature even at room temperature, which indicates that not all of the particles have undergone the ferromagnetic to superparamagnetic transition. This is consistent with the Au-Fe_3O_4 particles having a slightly higher DC blocking temperature (283K versus 267K for the bare Fe_3O_4 particles). Again, keeping in mind that the particles were synthesized on two different occasions, slight differences in size distributions is not surprising. What is important though is the fact that both samples are superparamagnetic at room temperature and in DC fields, which is normally how mag-

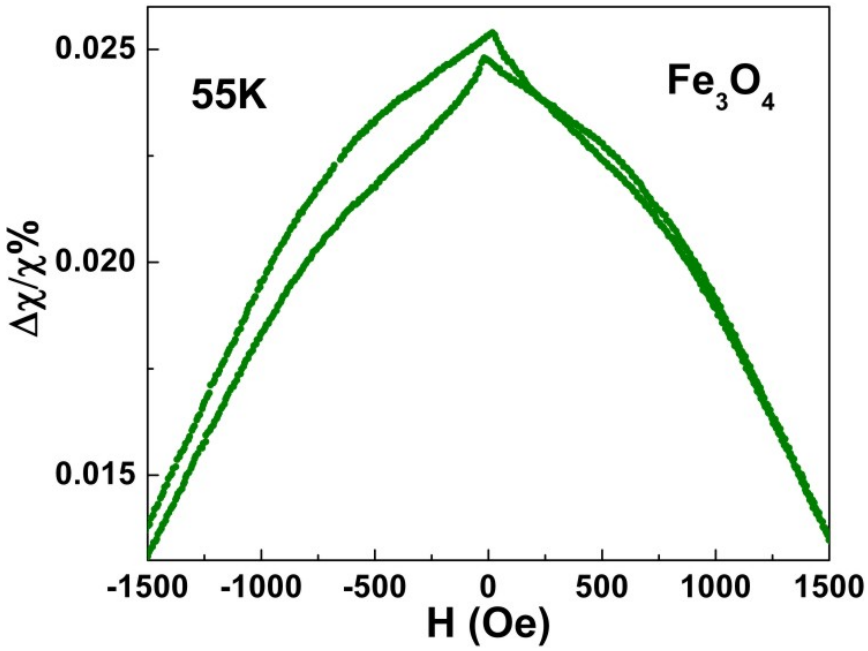

Figure 5.9. Low temperature bipolar transverse susceptibility scan of bare Fe_3O_4 not suspended in paraffin wax.

netic nanoparticles are manipulated in a biological environment. By slightly increasing the average size (thus the DC blocking temperature), the superparamagnetic particles become ferromagnetic in an AC field, in this case the AC field is 12 MHz. While this frequency is slightly above the generally accepted safe frequency of 1.2 MHz, the notion of tuning the size to correspond with DC superparamagnetic behavior and AC ferromagnetic behavior seems to be achievable for these particles.

Figure 5.14 is a low field, low temperature, bipolar scan of the Au-Fe_3O_4 particles taken at 20K. Like the Fe_3O_4 particles suspended in wax, the shape of the transverse susceptibility scan for these particles indicates an asymmetry in peak position with $H_{K1} \approx$ 415 Oe, and $H_{K2} \approx 535$ Oe. These values match up very well with the Fe_3O_4 particles indicating that two of the most important qualities of the Fe_3O_4 particles in paraffin wax (the anisotropy field H_K, and the lack of inter-particle interactions) are intact in the Au-Fe_3O_4 particles. This shows that coating the Fe_3O_4 particles with Au achieves the

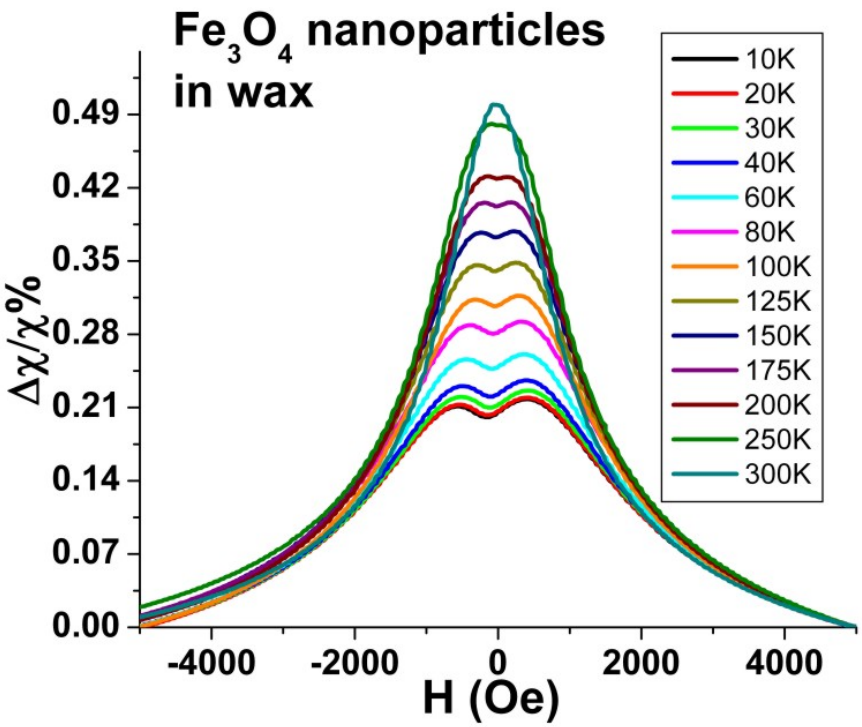

Figure 5.10. Transverse susceptibility scans taken at several different temperatures for Fe_3O_4 particles.

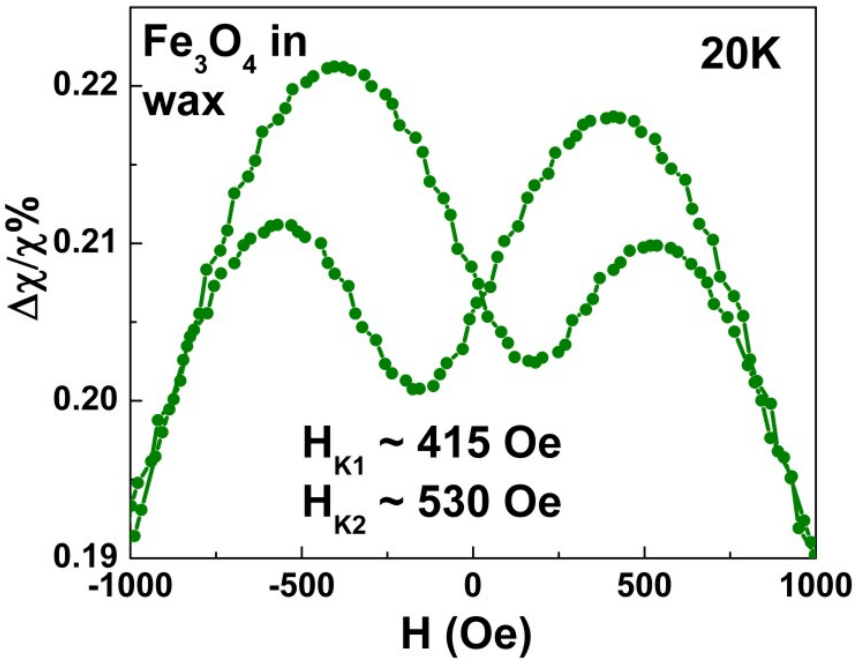

Figure 5.11. Low temperature (20K) transverse susceptibility bipolar scan of Fe_3O_4 particles.

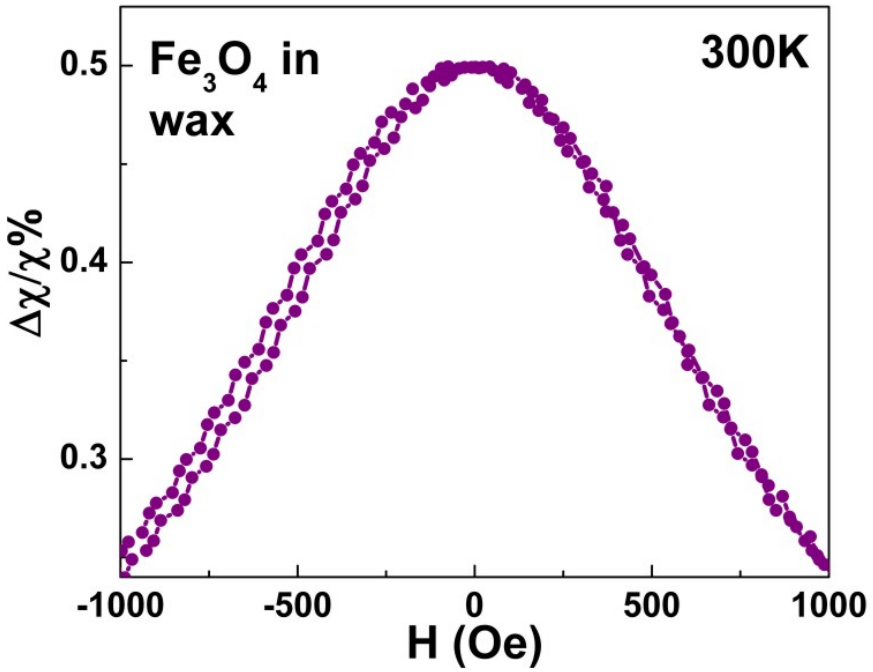

Figure 5.12. Room temperature (300K) transverse susceptibility bipolar scan of Fe_3O_4 particles.

important goal of separating the particles and reducing the inter-particle interactions, while still maintaining a nanopowder form that can be suspended in a biocompatible solvent.

Figure 5.15 shows a low field, room temperature, bipolar scan of the Au-Fe_3O_4 particles so that the anisotropy peaks can still be seen. It is likely that the majority of particles are too small to contribute to the anisotropy peaks (i.e. are superparamagnetic even at 12 MHz), but the very largest particles are ferromagnetic at this frequency.

In the next sections, we describe how the transverse susceptibility measurement was repeated for human embryonic kidney cells after transfection with the Au-Fe_3O_4 particles.

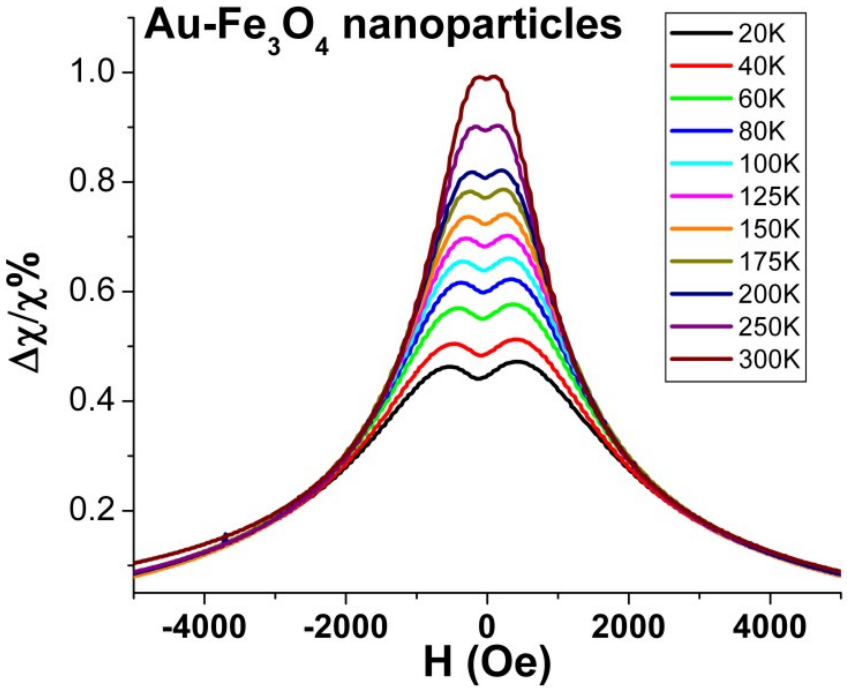

Figure 5.13. Transverse susceptibility scans taken at several different temperatures for Au-Fe_3O_4 particles.

5.5 Nanoparticle Transfection

Human embryonic kidney (HEK293) cells were obtained from the American Type Culture Collection (ATCC). Cells were cultured on a plastic substrate at 37°C in minimum

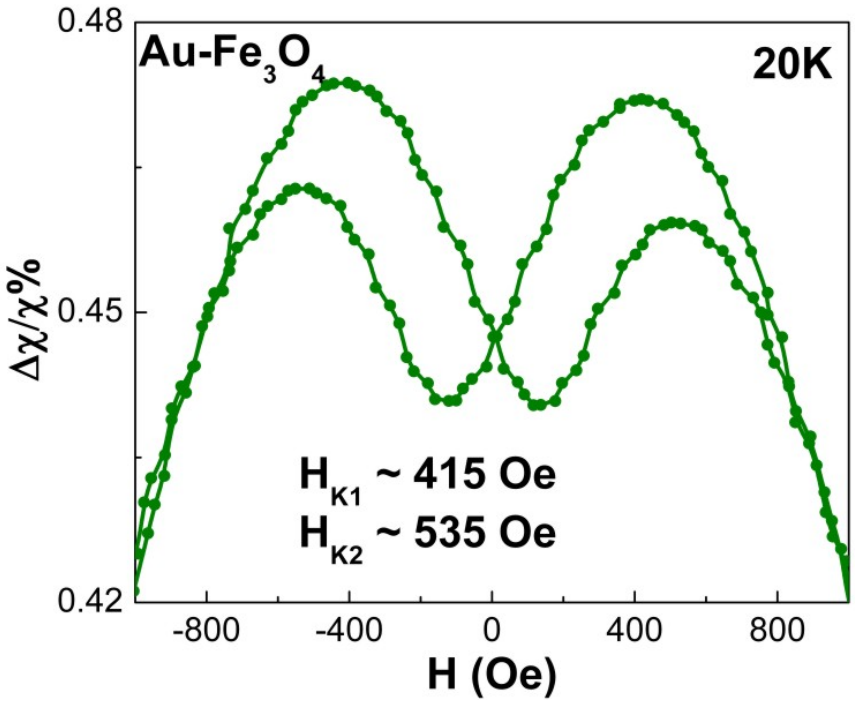

Figure 5.14. Low temperature (20K) transverse susceptibility bipolar scan of Au-Fe_3O_4 particles.

essential medium containing 10% fetal bovine serum and 100U/ml each of penicillin and streptomycin in an atmosphere of 5% CO_2/95% air.

Au-Fe_3O_4 nanoparticles were introduced to the medium at concentrations of 0.05, 0.1, 0.3, 0.5, and 1 mg/ml buffer, where they were transfected by the cells via phagocytosis. Cells were then detached from the substrate by removing excess medium, rinsing the cell layer with 0.25% (w/v) Trypsin- 0.53 mM EDTA solution and adding Trypsin-EDTA solution. A complete growth medium was then added to the cells for incubation. Figure 5.16 is a TEM image of a cell after transfection. The circle indicates the region where the nanoparticles are located, and the particles appear as the dark, filament-like structures.

The nanoparticles can be recovered from the cells through homogenization. Previous studies indicated that the percentage of nanoparticles transfected at maximum concentration (1 mg/ml) is approximately 70%.

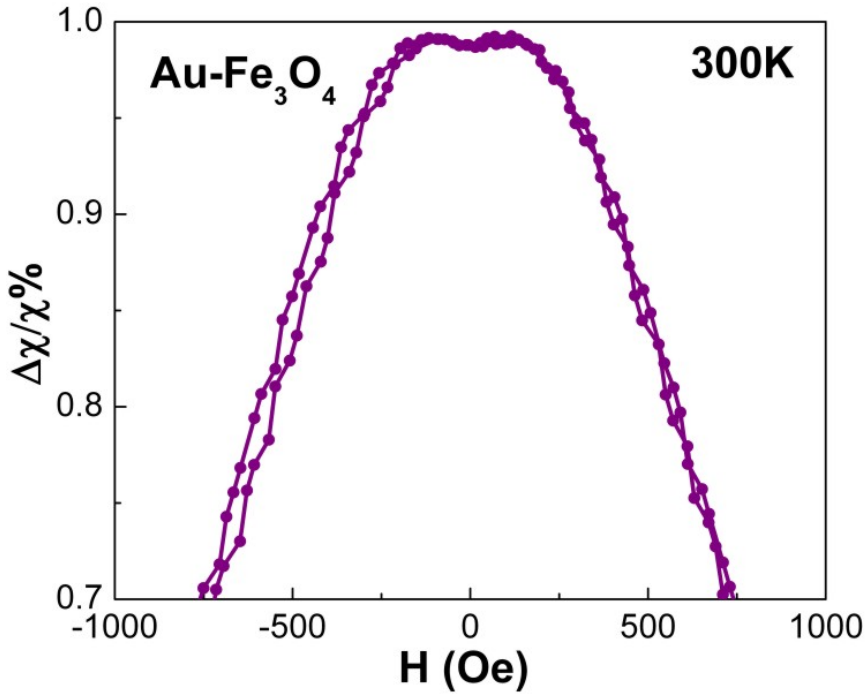

Figure 5.15. Room temperature (300K) transverse susceptibility bipolar scan of Au-Fe_3O_4 particles.

5.6 Transverse Susceptibility Measurements of Cells with Au-Fe_3O_4 Nanoparticles

Transverse susceptibility measurements were performed on cells that had not been transfected with nanoparticles, as well as cells after transfection of nanoparticles in all of the concentrations listed in the previous section. For each of these experiments, a sample of cells was placed inside of a liquid-safe, 1 ml sample holder. An inductance coil similar to the one used in the permanent transverse susceptibility setup was wound around the sample holder and held in place on each end by two small o-rings. The coil containing the sample was then soldered into the multifunctional probe in place of the regular inductance coil, and found to self-resonate at the same frequency of 12 MHz.

The transverse susceptibility probe was then placed inside of the Physical Properties Measurement System after the sample chamber had been warmed to ambient temperature, and the pressure inside the sample chamber was maintained at 1 atmosphere. This ensured

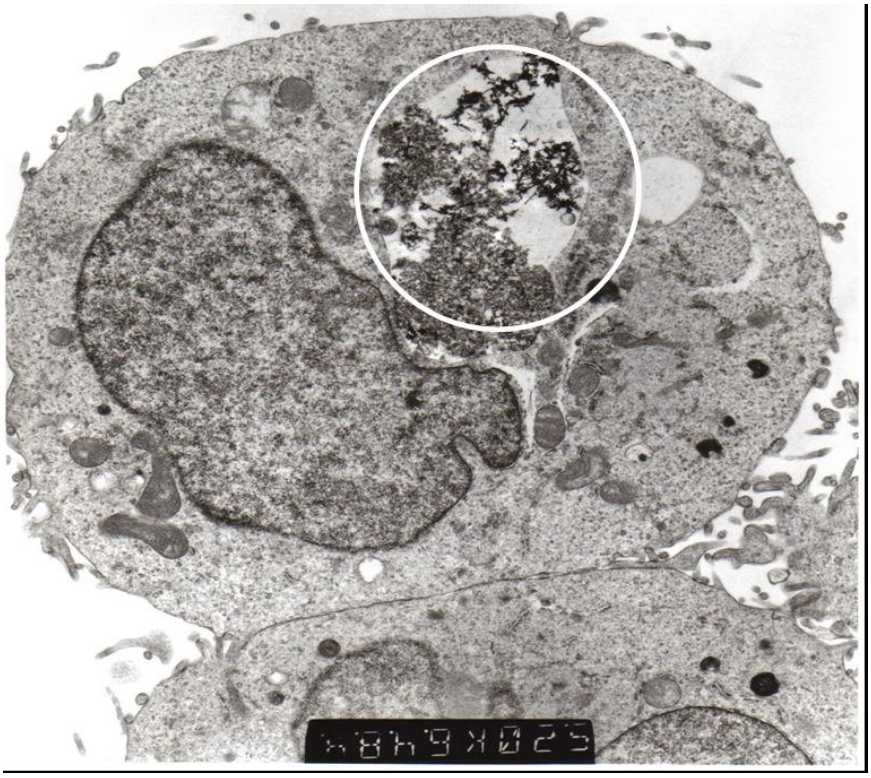

Figure 5.16. TEM image of Au-Fe_3O_4 particles (circled) inside of HEK cells.

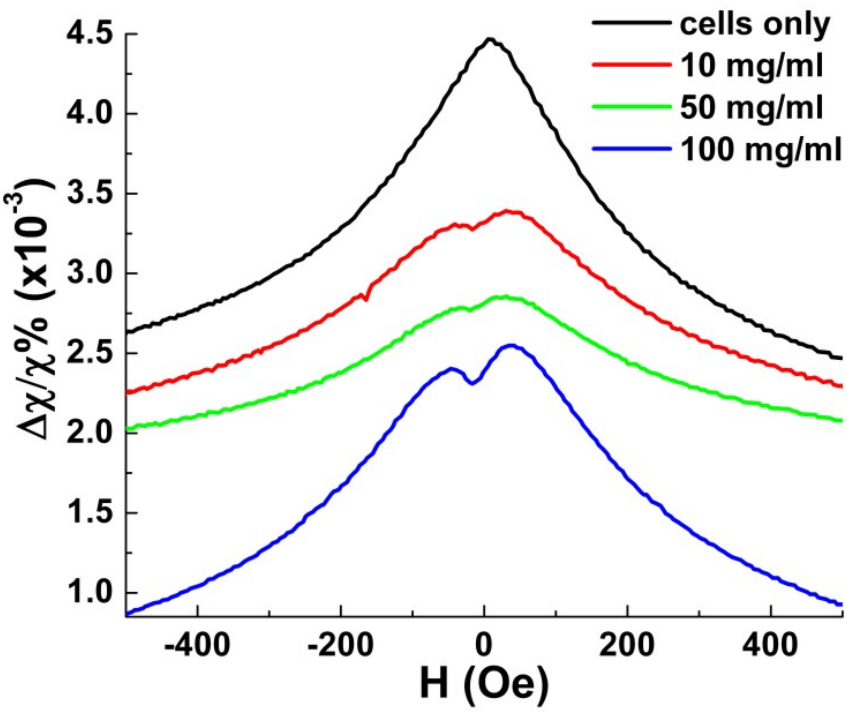

Figure 5.17. Transverse susceptibility measurements of HEK cells with varying concentrations of Au-Fe_3O_4 nanoparticles. The black scan is for the cells without any nanoparticles.

that the particles could stay inside of the cells as freezing of the cells causes the nanoparticles to be expelled. Applying a large enough pressure gradient might have caused the cells to be taken from the sample holder, and deposited into the sample chamber of the PPMS.

Low-field transverse susceptibility scans at ambient temperature and pressure were taken of the samples. Figure 5.17 shows the unipolar scan of the cells with several concentrations of the particles, as well as a scan of just cells that were not transfected with nanoparticles. It can clearly be seen that the transverse susceptibility probe was able to detect a signal from the nanoparticles inside of the cells, whereas the cells by themselves left no signal. For the lowest concentration of particles (0.05 mg/ml, not shown), no signal could be seen and at a concentration of 30 mg/ml (not shown), the signal was too noisy to exhibit anisotropy peaks. As expected, the highest concentration of nanoparticles gives the best signal, but it is important to note that at lower concentrations the signal of the particles can still be seen.

The anisotropy peaks seen for the nanoparticles inside of the cells appear more defined than those seen at room temperature for just the sample of Au-Fe_3O_4 particles. In this case, the same batch of Au-Fe_3O_4 particles was used for the measurement as for the transfection. It is well-known that certain types of cells will only take up particles in a particular size range, which was why the particles were synthesized in this experiment to be around 60 nm. However, while the DC measurements and even the transverse susceptibility measurements of just the particles pointed to a modest size dispersion, it may be that the cells only take up the biggest particles, acting as a size selection mechanism for the nanoparticles. If many of the smaller particles were not taken up by the cells, the ferromagnetic signal at 12 MHz would be stronger in this sample than the polydisperse nanoparticle sample (figure 5.15).

This experiment demonstrates how transverse susceptibility as a measurement technique can act as a biosensor for the presence of magnetic nanoparticles inside of cells. This could be used in a diagnostic capacity if the nanoparticles are functionalized with a biomarker specific to a type of cancer cell. Transfection of the nanoparticles would only occur if the cells were cancerous, and then transverse susceptibility could be used to determine if the cells had taken up the particles, and therefore if they are cancerous. Even though we used a Physical Properties Measurement System to provide the H_{DC} it is well worth noting that the fields needed for this experiment are less than 500 Oe, a field strength easily achievable with an electromagnet. The measurements were also taken at room temperature and not in a vacuum. Realistically, transverse susceptibility used in this capacity could be set up as a table-top experiment rather than integrated into a commercial PPMS.

5.7 Conclusion

In this chapter, we presented DC magnetic characterization and transverse susceptibility data for Fe_3O_4 and Au-Fe_3O_4 nanoparticles for biomedical applications. We showed that bare Fe_3O_4 particles have strong inter-particle interactions, compromising the magnetic properties, and likely leading to particle agglomeration. This is not preferable for

biomedical applications such as drug delivery or hyperthermia, which require the uptake of single particles within a specific size range.

Au-Fe_3O_4 particles showed almost identical magnetic properties to Fe_3O_4 particles that were suspended in a paraffin wax matrix, showing that a coating of Au around the Fe_3O_4 acts to greatly diminish or eliminate inter-particle interactions and agglomeration, while still keeping the versatility of a magnetic nanoparticle in a biocompatible suspension. Additionally, the Au coating is attractive because it offers more choices for functionalization via Au-thiol chemistry.

While all the particles studied were superparamagnetic at room temperature and under DC applied fields, it was demonstrated just how sensitive the ferromagnetic to superparamagnetic transition is to applied AC fields in the particle size range studied. The blocking temperature of the Fe_3O_4 particles was slightly lower than that of the Au-Fe_3O_4 particles, and the Fe_3O_4 particles showed room temperature superparamagnetism even at 12 MHz. Some of the Au-Fe_3O_4 particles appeared to still be in the ferromagnetic state at 12 MHz, consistent with the higher blocking temperature, indicating a slightly higher average particle size. This change in magnetic properties from superparamagnetic at DC fields to ferromagnetic at AC fields is ideal for hyperthermia. This size range also allowed for easy transfection by the cells, and led to the emergence of clear anisotropy peaks when transverse susceptibility was performed on the cells with the nanoparticles.

CHAPTER 6

"DUMBBELL" AND "FLOWER" Au-Fe_3O_4 COMPOSITE NANOPARTICLES

6.1 Introduction

In the previous chapter, it was described how Fe_3O_4 nanoparticles with an Au shell can be useful for several biomedical applications. While the magnetic core can be manipulated by DC and AC external fields, the gold surface can be functionalized to allow for attachment of therapeutic molecules or contrast agents to be delivered to the tissue of interest. So far, the key requirements have been that the Au have a surface available for functionalization and that the Fe_3O_4 be of a size to promote cellular uptake, while maintaining desirable magnetic properties. While most applications require that the particles be superparamagnetic, we saw in the last chapter how tuning the size of the particles to have frequency-dependent blocking around room temperature can optimize the magnetic properties.

However, as was shown by our collaborators, because of the lattice constants of Au and Fe_3O_4 being nearly 1:2 in ratio, the two can be grown epitaxially coupled to each other [93]. They used this fact to create composite nanoparticles of Au and Fe_3O_4 grown together in the shape of a dumbbell, with the two sharing a common facet. One advantage this may have over the core-shell structure is that not just the Au will be available for functionality through thiol attachment, but the exposed Fe_3O_4 surface can be functionalized using different chemistry, allowing the same composite particle to deliver two types of molecules. Moreover, it was proposed that the unique shape of the particle and the Au-Fe_3O_4 interface could give rise to different magnetic properties than the core-shell particles.

It was also found that by slightly changing the pH of the chemical reaction, the Fe_3O_4 can be nucleated on several Au facets, creating a composite structure similar to a flower in appearance, with Au making up the core, and Fe_3O_4 nanoparticles making up "petals". In this chapter, we will show that this results in a system with vastly different magnetic properties from the dumbbell particles, which can be understood in terms of the complex and competing interactions present in each composite particle. While the dual functionality of the dumbbell particles is promising for biomedical applications, the anomalously high anisotropy of the flower particles should be further explored for higher anisotropy applications such as beating the superparamagnetic limit for high density magnetic recording.

6.2 Nanoparticle Synthesis

All nanoparticles were synthesized at Brown University by Professor Shouheng Sun's group [93]. The dumbbell Au-Fe_3O_4 nanoparticles were prepared by decomposing iron pentacarbonyl, $Fe(CO)_5$, over the surface of Au nanoparticles in the presence of oleic acid and oleylamine. The mixture was heated to reflux (300°C), followed by oxidation in air. The Au nanoparticles were formed *in situ* by injecting $HAuCl_4$ solution into the reaction mixture. Flower-shaped nanoparticles were synthesized by changing the solvent from a non-polar hydrocarbon to a slightly polarized solvent (i.e. diphenyl ether). The size of the Au particles can be tuned by controlling the temperature at which the $HAuCl_4$ is injected. The size of the Fe_3O_4 particles can be tuned by adjusting the ratio between $Fe(CO)_5$ and Au. More $Fe(CO)_5$ results in larger Fe_3O_4 particles.

Figure 6.1 is a TEM image of a sample of dumbbell Au-Fe_3O_4 nanoparticles. For this sample, the average Au size is about 8 nm, and the average Fe_3O_4 size is about 9 nm. The dark particles represent the Au due to the higher electron density, and the lighter particles are the Fe_3O_4. Figure 6.2 is a TEM image of the flower nanoparticles. For comparison purposes, the flower sample has the same sizes of Au and Fe_3O_4 particles as the dumbbell sample (8 nm and 9 nm respectively).

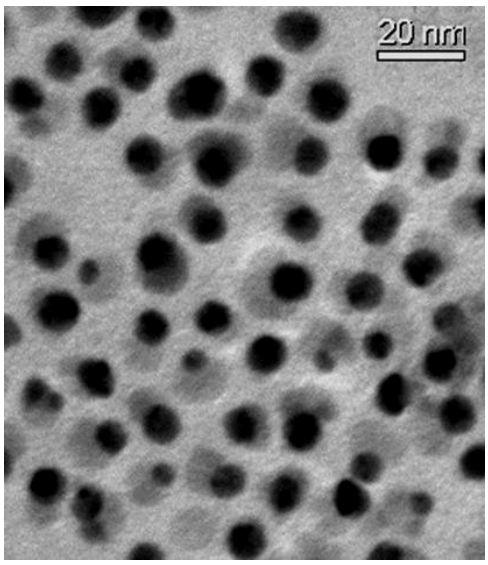

Figure 6.1. TEM image of a dumbbell Au-Fe_3O_4 nanoparticle. (Courtesy of Brown University)

In this synthesis method, the Fe_3O_4 is grown epitaxially onto the Au seed particle, which is possible because Au has an fcc structure with $a = 4.08$Å, while Fe_3O_4 has an inverse spinel (cubic) structure with $a = 8.35$Å, which is within 3% of being exactly double that of Au. This epitaxial growth is confirmed by high resolution TEM (HRTEM) for the dumbbell nanoparticles (figure 6.3). The lattice fringes in each particle correspond to atomic planes within the particle, indicating that both types of particles are single crystalline. The distance between two adjacent planes in Fe_3O_4 was measured to be 0.485 nm, corresponding to the (111) planes in the Fe_3O_4. The lattice fringe spacing in Au is 0.24 nm, resulting from a group of (111) planes in the Au.

Once the Fe_3O_4 starts to nucleate on the Au in the hydrocarbon solvent, the free electrons from the Au must compensate for the charge induced by the polarized plane at the interface. As the Au has only a limited source of electrons, the compensation makes all other facets of the Au nanoparticle electron deficient and unsuitable for multinucleation, giving only the dumbbell structure. If the polarity used for the synthesis is increased, the Au nanoparticle could compensate for the apparent electron density loss with charges from the solvent, allowing nucleation on multiple facets, resulting in the flower structure. [93]

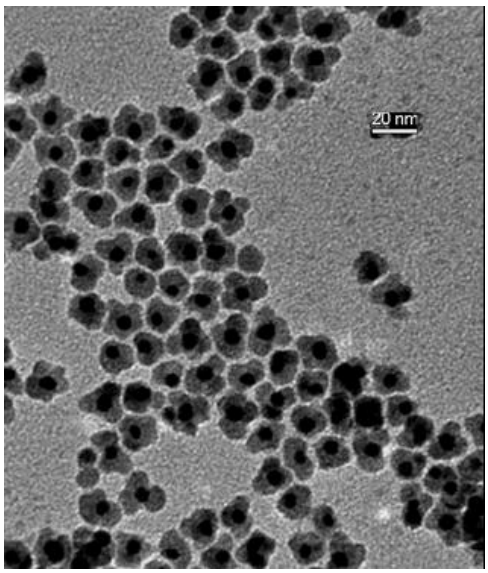

Figure 6.2. TEM image of a flower Au-Fe_3O_4 nanoparticle. (Courtesy of Brown University)

6.3 DC Magnetic Measurements

Magnetic measurements in a static field were carried out on all samples using the Physical Properties Measurement System (PPMS). These measurements consisted of zero field cooled and field cooled (ZFC-FC) curves and magnetization versus field (M-H) curves. Figure 6.4 shows the ZFC-FC curves for the dumbbell nanoparticles taken in a field of 100 Oe. The ZFC curve shows a peak at around 60K, consistent with the transition from the blocked state to the superparamagnetic state. The ZFC-FC curve for the flower nanoparticles (figure 6.5) shows a sharper peak around 90K. There is an additional feature seen in the FC curve, which is flat until about 65K, and then drops rapidly. This does not line up with the peak seen in the ZFC curve, and is indicative of another characteristic temperature associated with the flower nanoparticles, which will be explored further in subsequent sections. Since the Au and Fe_3O_4 components are the same size for both samples, the increase in traditional blocking temperature associated with the flower nanoparticles has to be from an added anisotropy contribution, likely due to the unusual configuration of the particles.

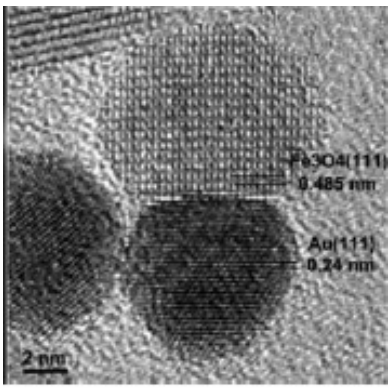

Figure 6.3. High resolution TEM image of a dumbbell Au-Fe_3O_4 nanoparticle. (Courtesy of Brown University)

Interestingly, the ZFC curves for both the dumbbell and the flower Au-Fe_3O_4 particles exhibit a negative magnetization at the lowest temperatures. This type of behavior has not been reported in the literature for ferrite nanoparticles of any configuration, and is likely due to the unique interfaces that are present in these systems. This feature is currently under intense investigation, and recent experiments have revealed that for both types of particles increasing the external DC magnetic field results in the low temperature magnetization increasing. ZFC curves were taken for several fields to determine at which field the 2K magnetization crosses from a negative value to a positive value. For the dumbbell particles, this field is around 150 Oe, whereas for the flower particles, it is around 210 Oe. It is not surprising that in light of the multiple interfaces present in the flower particles, there is a higher magnetic energy associated with changing the magnetization from a negative value to a positive value.

M-H measurements for the dumbbell nanoparticles were taken at low temperature (2K) and room temperature as well as some intermediate temperatures. Figure 6.7 shows the curves for 2K and 75K, just above the blocking temperature. The coercivity at 2K was measured to be 750 Oe, and at 75K the coercivity is zero, confirming that the particles are then in the superparamagnetic state. For the flower nanoparticles (figure 6.8), the low temperature M-H curve revealed a much higher coercivity (1270 Oe). In addition, the curve was irreversible (did not close) up to 1.5 Tesla and did not saturate at fields up to 2

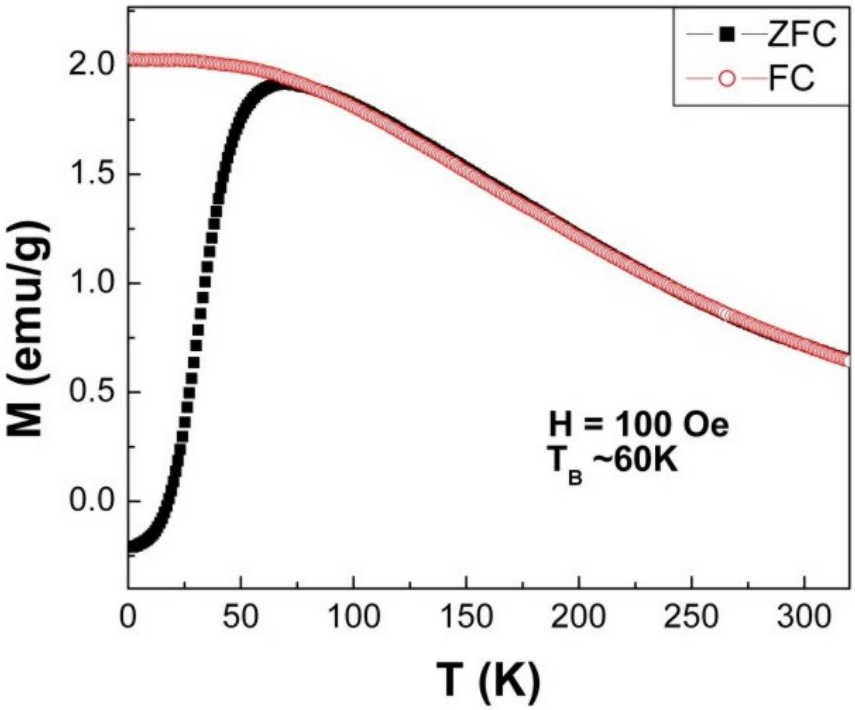

Figure 6.4. Zero field cooled and field cooled curves for dumbbell Au-Fe_3O_4 nanoparticles.

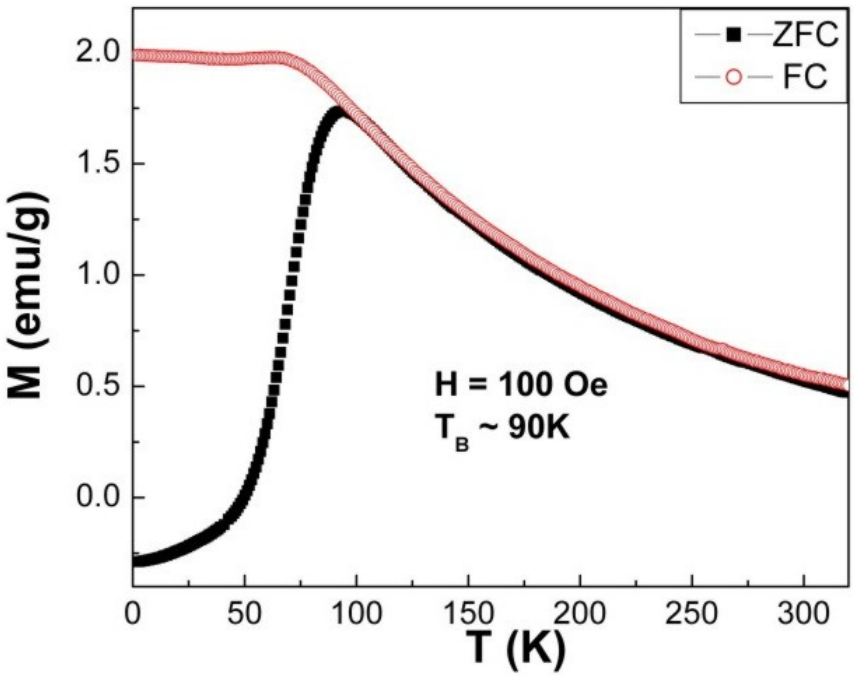

Figure 6.5. Zero field cooled and field cooled curves for flower Au-Fe_3O_4 nanoparticles.

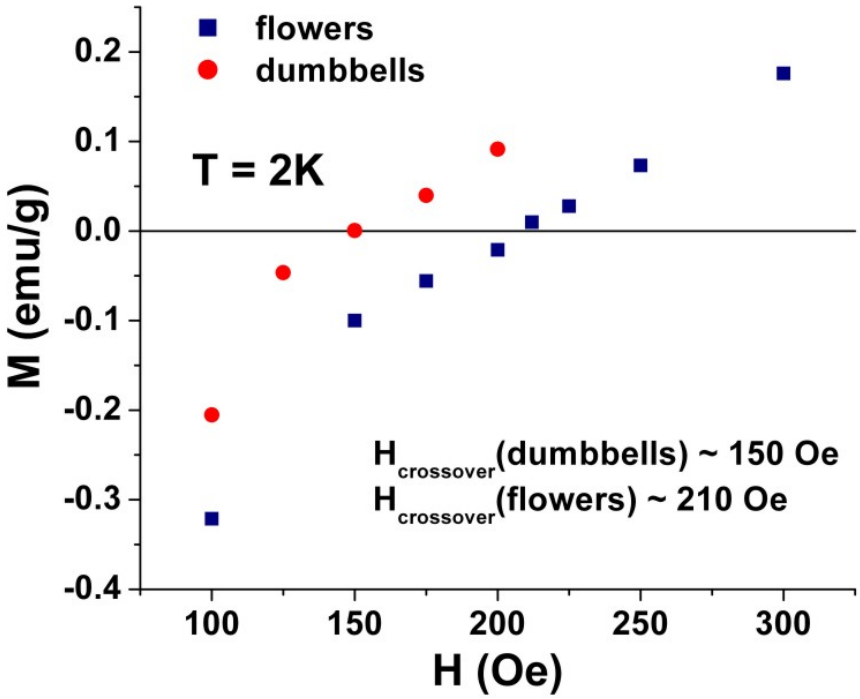

Figure 6.6. Values of magnetization at 2K for the Au-Fe_3O_4 composite particles taken in the zero field cooled condition for different values of H.

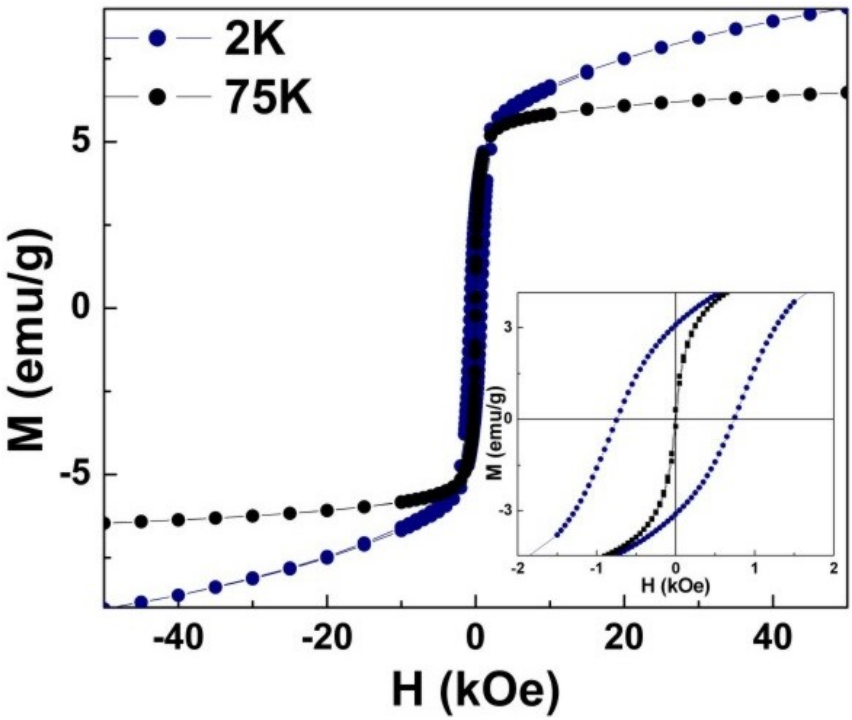

Figure 6.7. Magnetization versus field curve for dumbbell Au-Fe_3O_4 nanoparticles taken at 2K (blue) and 75K (black).

Tesla. These features, combined with the higher blocking temperature and anomalous 65K feature in the FC curve, are indicative of a fundamental difference in magnetic response between the dumbbell (which are closer to conventional) and the flower (more anomalous) nanoparticles. One can infer that the major difference between the two systems is the geometrical arrangement of the Fe_3O_4 clusters, and the role of the spins at the surfaces as well as at the multiple interfaces between Fe_3O_4 and Au. It is known that interfacial spin configuration can be greatly influenced in core-shell nanoparticles [60, 89, 75, 64], and an important consequence is the observation of exchange bias in such materials. The next section describes experiments that were done to probe the presence of exchange bias in both of these types of Fe_3O_4 particles.

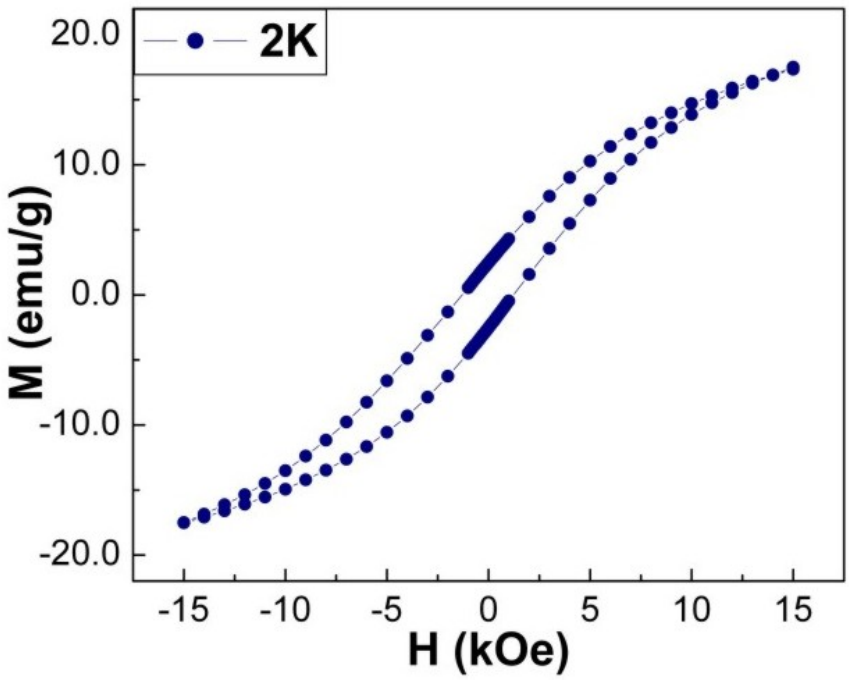

Figure 6.8. Magnetization versus field curve for flower Au-Fe_3O_4 nanoparticles taken at 2K.

6.4 Exchange Bias and Training Effect in Flower-Shaped Nanoparticles

To test for the presence of exchange bias, both types of particles were cooled from room temperature in a 5 Tesla field, and magnetization versus temperature measurements were performed. While the dumbbell-shaped particles retained a symmetric hysteresis loop for all temperatures after field-cooling, the flower-shaped particles exhibited a large horizontal shift in their hysteresis loops (figure 6.9). This exchange bias was then tested for a number of temperatures and shown to persist up to about 65K, lower than the blocking temperature but consistent with the feature seen in the FC curve. This suggests two characteristic temperatures for the flower particles, as opposed to only one for the dumbbell particles (namely, the blocking temperature). This lower characteristic temperature for the flower particles is likely due to the onset of a unidirectional anisotropy, whose origin can be correlated with interactions between Fe_3O_4 particles sharing the same Au seed particle (henceforth, these will be referred to as *intra*-particle interactions as opposed to the more

well-known *inter*-particle interactions, the interactions between separate particles). In addition to the horizontal shift in the M-H loops, there is a marked increase in coercivity after field-cooling (1920 Oe after field cooling as opposed to 1270 Oe after zero field cooling), which is another signature of exchange bias. Figure 6.10 shows the exchange bias field (H_E, or the amount by which the loop is shifted) and coercivity (H_C) as a function of temperature for the flower particles. The shapes of the curves are similar, and both have 65K as a characteristic temperature (H_E goes to zero, H_C decreases less rapidly, consistent with more traditional nanoparticle systems). These similarities suggest that the two phenomena are related, and that the anisotropy in these particles is uniaxial as well as unidirectional.

Exchange bias in nanostructures is a topic of current interest, and has been reported in several core-shell particles [60, 89, 75, 64, 96]. These results for the flower-shaped Au-Fe_3O_4 particles represent the first report of exchange bias in nanoparticles with an ordered cluster-type geometry, displaying both unidirectional and uniaxial anisotropy. Furthermore, since exchange bias isn't seen in either of the other two geometries studied (core-shell and dumb-bell configuration), the behavior must be associated this particular configuration.

In many exchange-biased systems, the exchange field, H_E, and the coercive field, H_C, will decrease if the magnetization versus field measurement is repeated immediately after an initial magnetization versus field measurement is taken. This decrease in H_E and H_C upon subsequent M-H cycles is known as the training effect [60]. Like many exchange-biased systems, the flower nanoparticles also exhibit a training effect. Figure 6.11 is a plot of the field cooled hysteresis loop taken from positive saturation to negative saturation and back to positive. The measurement was then repeated immediately without zeroing out the field or warming the sample. H_E was still present but to a lesser extent, and H_C decreased as well. The measurement was repeated for one more cycle, and H_E and H_C decreased again, but the decrease from second to third cycle was not as much as from the first to second cycle. In total, H_C decreased from 1920 Oe in the first cycle to 1650 in the third cycle. The inset of figure 6.11 shows H_C as a function of M-H cycle.

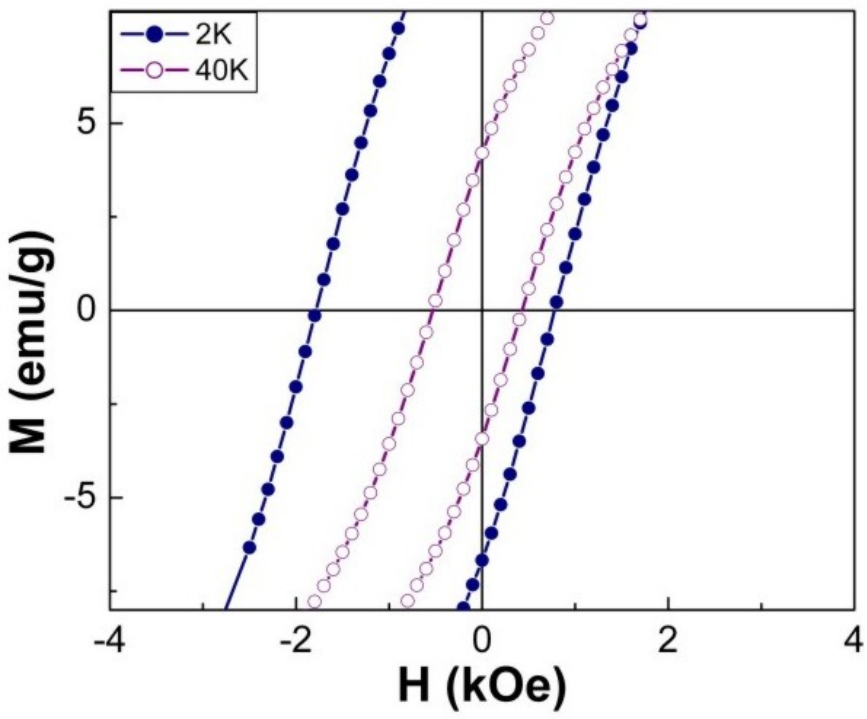

Figure 6.9. Magnetization versus field curve for flower Au-Fe_3O_4 nanoparticles taken at 2K (blue) and 40K (purple) after cooling in a 5 Tesla field.

It is interesting to note that both the horizontal shift in hysteresis loop, and the training effect seen in the nanoparticles, are different from those seen in many exchange-biased thin films. In the latter case, the first field cooled M-H loop is also accompanied by a first order reversal asymmetry. In these systems, the hysteresis loop has a sharp jump in the first magnetization reversal (with decreasing field), while the second reversal (with increasing field) is more gradual. In contrast, the second hysteresis loop is more symmetric with a smaller decrease in H_E and H_C, and similar shapes for both magnetization reversals. Any subsequent hysteresis loops are unchanged in shape from the first. It is suggested that in thin films, two reversal mechanisms are present, with domain wall nucleation and propagation being responsible for one reversal, and coherent rotation of magnetization being responsible for the other [54]. In nanoparticle systems, there is only coherent magnetization rotation, so the hysteresis loop can only show one type of reversal, which is consistent with Zheng *et al.*'s model of training effects in γ-Fe_2O_3 coated Fe nanoparticles [96]. In

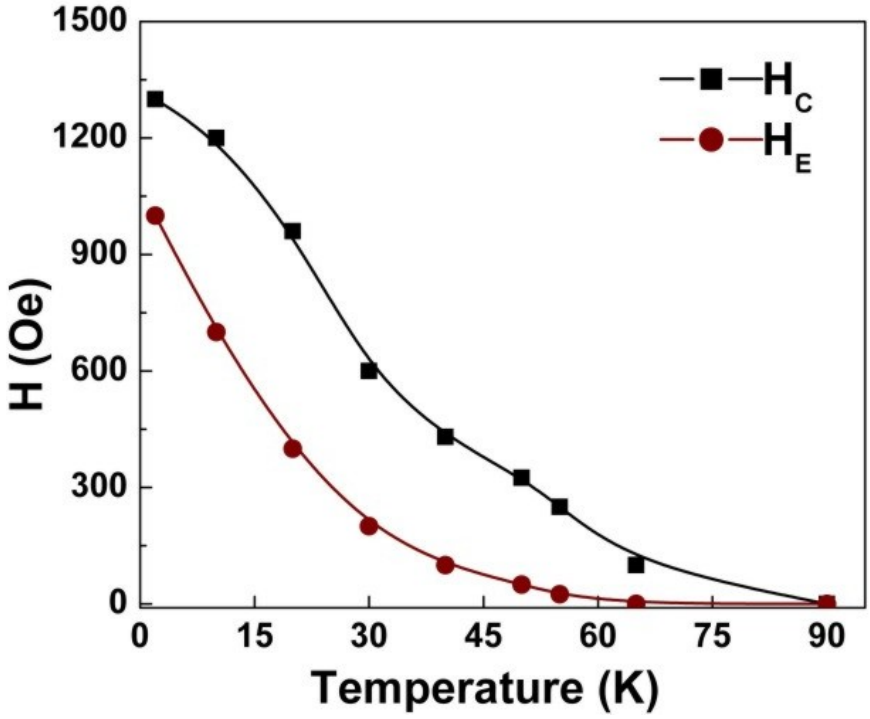

Figure 6.10. H_E and H_C as a function of temperature for flower Au-Fe_3O_4 nanoparticles after cooling in a 5 Tesla field.

this model, the training effect and horizontal shift in M-H loops has been interpreted by a modified Stoner-Wohlfarth model, with an additional unidirectional anisotropy energy term to the total energy. If the presence of a pinned layer, which causes the exchange bias, is due to a spin-glass-like surface phase, then the frozen spins which were originally aligned in the cooling field direction may change their directions and fall into other metastable configurations during the hysteresis measurements, leading to a training effect. In this case, it is not exactly clear whether it is a surface spin effect which is causing the training effect, or the pinning of spins at the Au-Fe_3O_4 interface. In the last section, we will present a schematic picture describing the various possible interactions in the flower particles.

6.5 AC Susceptibility Measurements

We measured the temperature dependence of AC susceptibility (both in phase $\chi\prime$(T) and out of phase $\chi\prime\prime$(T)) in the frequency range of 10 Hz to 10 kHz for both sets of

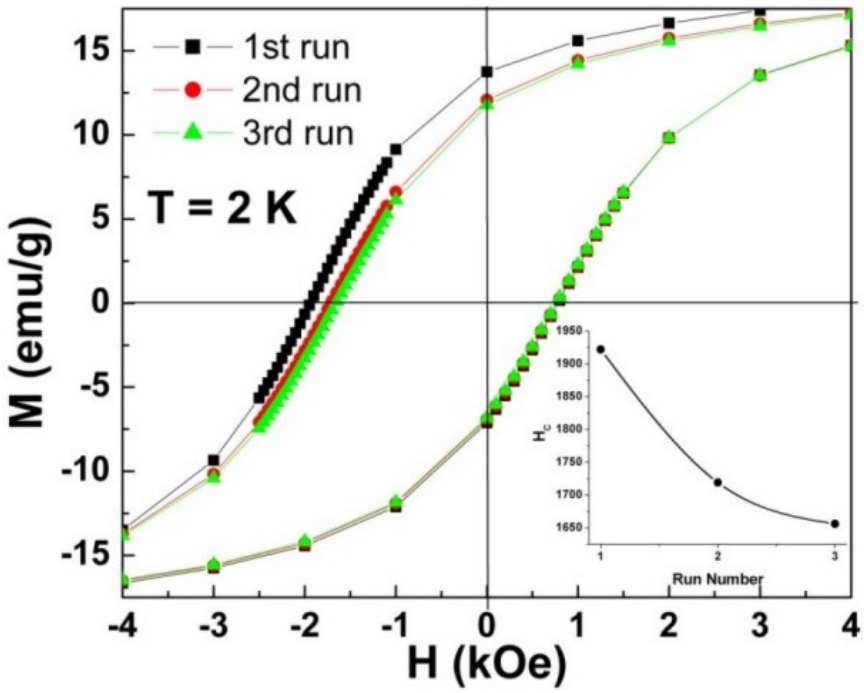

Figure 6.11. Training effect in flower-shaped Au-Fe_3O_4 nanoparticles. The inset shows the coercivity (H_C) as a function of the loop cycle.

composite nanoparticles. The data for both the dumbbell nanoparticles (figure 6.12) and flower nanoparticles (figure 6.13) show superparamagnetic behavior with a maximum at a temperature T_m, which shifts to a higher temperature with increase in frequency.

The out-of-phase component of the AC susceptibility for the flower particles shows a shift in peak position with an increase in frequency, as well as a decrease in peak magnitude, again consistent with superparamagnetic particles.

As discussed in chapter 2, The magnetization reversal of a single domain particle over the anisotropy barrier (E_a) can be described using the Néel-Arrhenius law: $\tau = \tau_0 \exp(E_a/k_BT)$ [22, 73]. We first plotted $1/T_B$ vs. ln(f), and from the fitting of the experimental data using the above equation, we obtained values of E_a/k_B for the flower and dumbbell particles as 4211K (5.8×10^{-20} J) and 2741K (3.8×10^{-20} J) respectively. The fitted values of τ_0 for the flower and dumbbell particles were 4.5×10^{-17} s and 3.1×10^{-15} s respectively. These attempt frequencies are unphysical and cannot accurately de-

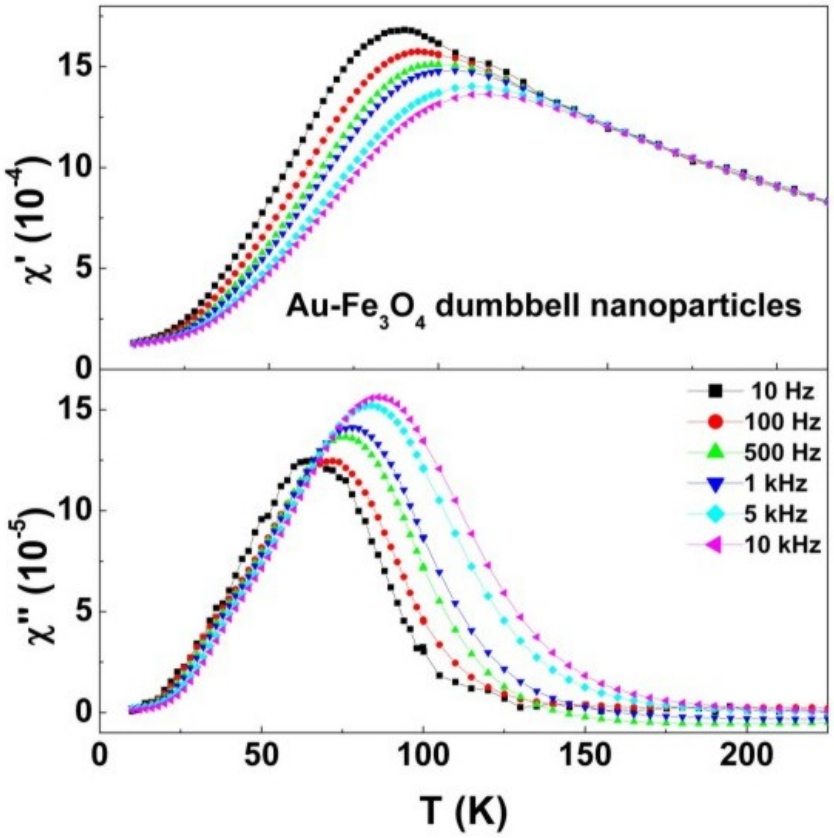

Figure 6.12. Temperature dependence of the in-phase $\chi\prime$(T) and out-of-phase component $\chi\prime\prime$(T) of the magnetic susceptibility for the dumbbell Au-Fe_3O_4 nanoparticles.

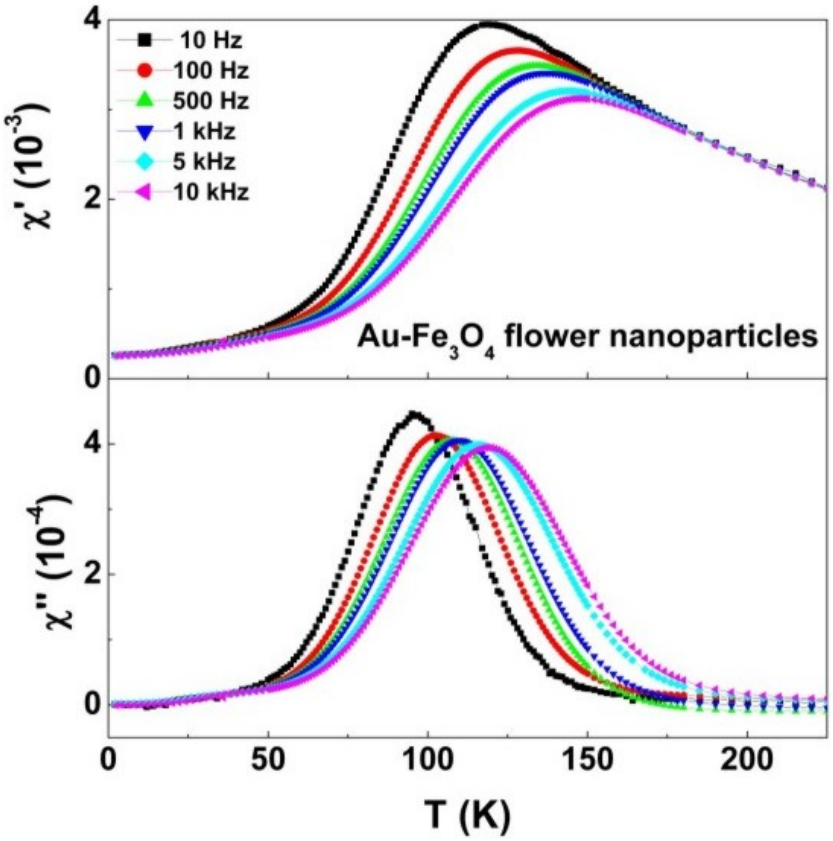

Figure 6.13. Temperature dependence of the in-phase $\chi\prime$(T) and out-of-phase component $\chi\prime\prime$(T) of the magnetic susceptibility for the flower Au-Fe_3O_4 nanoparticles.

scribe the relaxation of these particles since the accepted τ_0 for an array of non-interacting superparamagnetic particles is between 10^{-10}-10^{-9} s. This prompted us to try to use the Vogel-Fulcher model to calculate τ_0 and E_a/k_B values for the Au-Fe_3O_4 particles (figure 6.15). Recall from section 2.2 that the Vogel-Fulcher equation can account for weak dipolar interaction by incorporating the parameter T_0 so that $\tau^{-1} = \tau_0^{-1} \exp(E_a/k_B(T - T_0))$. This time the values of τ_0 and E_a/k_B for the dumbbell particles were 0.80×10^{-8} s and 616K respectively. These are both reasonable values and indicate that the weakly interacting particle assumption is valid for the dumbbell nanoparticles. The value of T_0, which can be thought of as an activation energy for the dipolar interaction in this system, is 50K. For the flower Au-Fe_3O_4 particles, we were still unable to obtain reasonable values for τ_0 and E_a/k_B. In fact, the values deviated even further from the accepted range as we obtained a τ_0 of 0.36×10^{-27} s and an E_a/k_B of 13675K. We also obtained a nonsensical value of -105K for T_0. Neither the Néel-Arrhenius fits nor the Vogel-Fulcher fits successfully modeled the relaxation of the flower particles, which indicates that the particles are interacting (since they don't fit Néel-Arrhenius), but that the interactions cannot be described as weak and dipolar. This points to the existence of a much stronger intra-particle type interaction in the flower particles.

6.6 Transverse Susceptibility Measurements

To further study the anisotropy properties of both types of particles, we did transverse susceptibility measurements over a broad range of temperatures (10K < T < 300K), with a variable DC field, H_{DC}, of ± 5 kOe in both zero field cooled and field cooled conditions. Figure 6.16 shows the field-dependent transverse susceptibility data for the dumbbell-shaped particles at fixed temperatures from 10K to 300K measured in the zero field cooled condition. The plot represents unipolar field sweeps from positive (+5kOe) to negative (-5kOe) fields, chosen to be far above saturation. The two peaks seen in the scan below the blocking temperature occur at the positive and negative anisotropy fields. These peaks shift to higher fields and broaden as the temperature decreases. It has been suggested that the

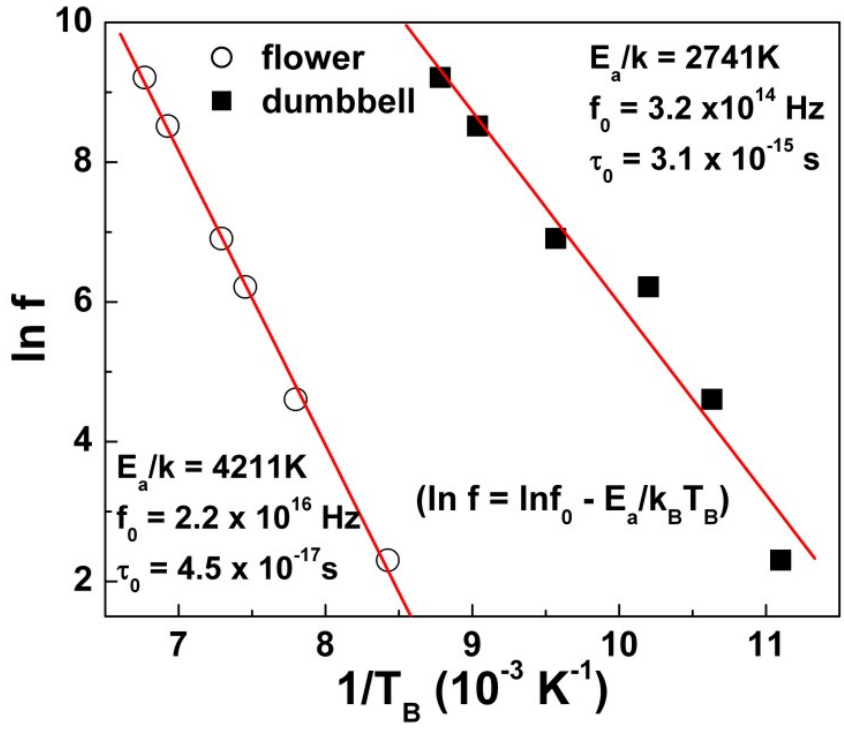

Figure 6.14. Plot of ln(f) against $1/T_B$ for both types of nanoparticles. The solid red line is the fit to the Néel-Arrhenius law.

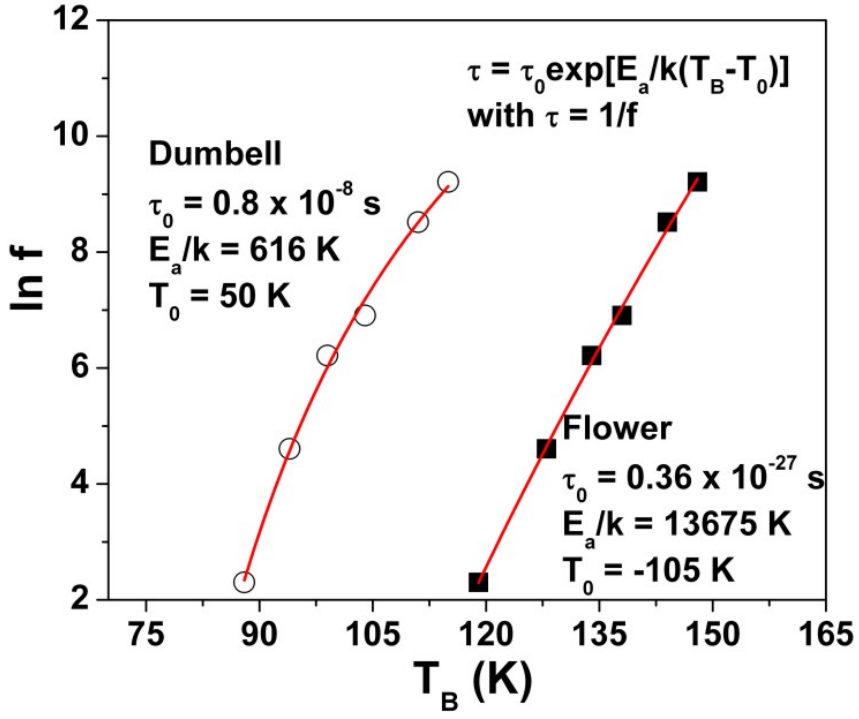

Figure 6.15. Plot of ln(f) against $1/T_B$ for both types of nanoparticles. The solid red line is the fit to the Vogel-Fulcher relation.

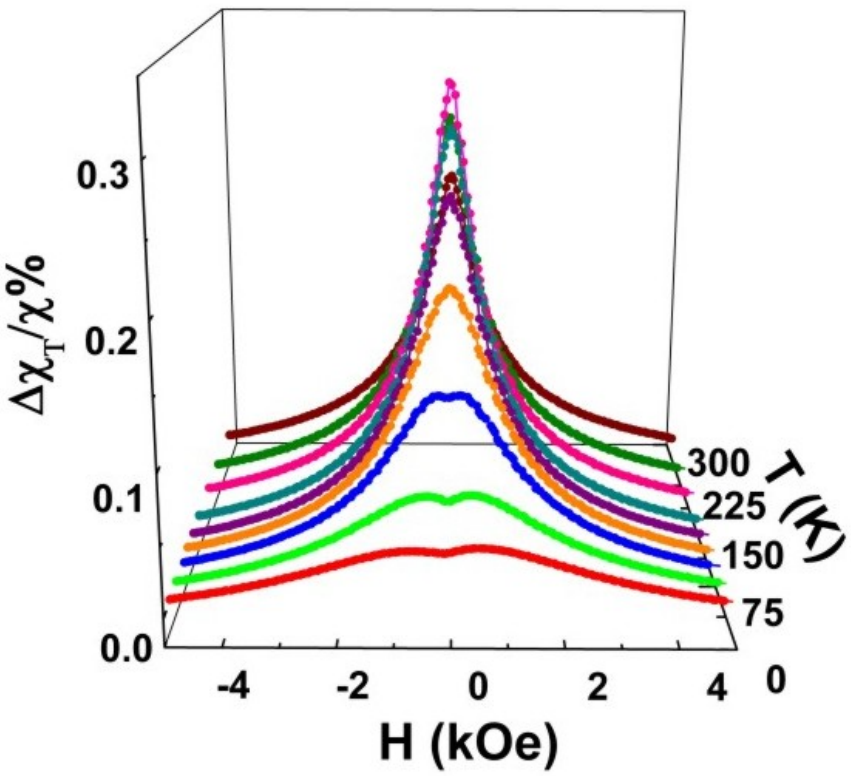

Figure 6.16. Unipolar transverse susceptibility curves of the dumbbell Au-Fe_3O_4 nanoparticles taken at several different temperatures.

broadening of anisotropy peaks at the lowest temperatures is due to the random freezing of spins [66]. At higher temperatures, above the blocking temperature, the peaks merge into a single peak at zero field with a monotonic decrease in transverse susceptibility as the field is increased in the negative and positive directions. This signals the transition from the blocked state to the superparamagnetic state.

Figure 6.17 shows the low-field portion of a bipolar scan taken at 30K for the same sample of dumbbell-shaped particles as presented in figure 6.16. As is the case with most nanoparticles, two distinct sets of peaks can be seen, the narrower peak with the higher magnitude ($\pm H_{K1}$) occurring after saturation, the broader peak with the lower magnitude ($\pm H_{K2}$) occurring after the field passes through zero. As discussed in chapter 3, this is likely due the differences in the energy states of the system during saturation (when the Zeeman energy is highest), and after the field is decreased to zero, allowing some of the

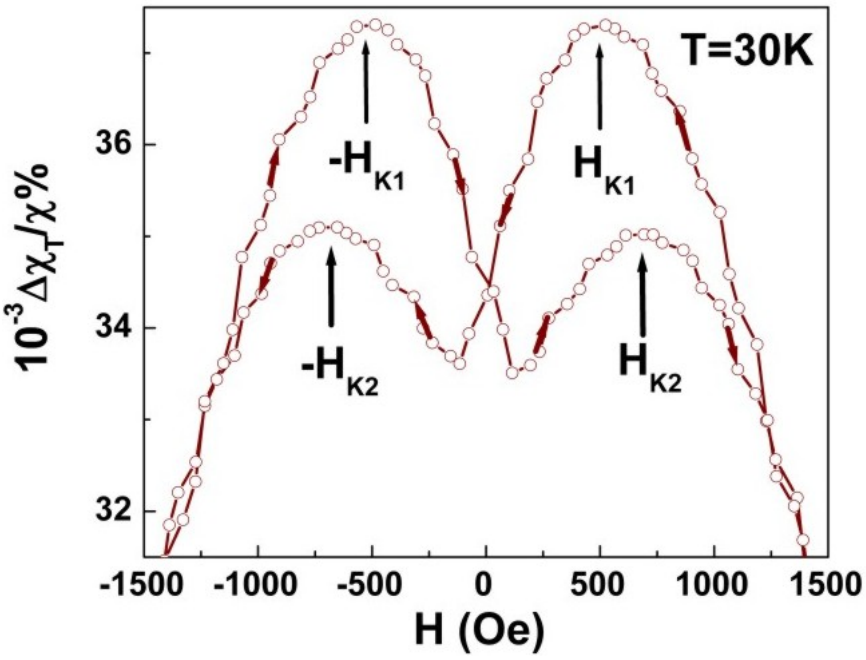

Figure 6.17. Low field portion of a transverse susceptibility scan of the dumbbell Au-Fe_3O_4 nanoparticles taken at 30K. The arrows indicate the sequence of measurement.

spins to randomize again. Also recall that according to Aharoni's theory [2], one should see a switching peak as well for a Stoner-Wohlfarth particle. In nanoparticle arrays, the switching field associated with each particle is not a well-defined peak, and is instead a distribution, which is likely merged into the H_{K2} peak. For the dumbbell nanoparticles, these two separate peaks, H_{K1} and H_{K2}, are symmetric with respect to the positive to negative (+scan) and the negative to positive (−scan). We also see no shift in peak position after cooling in a 5 Tesla field, showing the absence of exchange bias, and thus consistent with the field cooled M-H measurements.

In figure 6.18, we present the unipolar transverse susceptibility data for the flower nanoparticles at several different temperatures. The most important thing to note is the dramatically large difference in the anisotropy fields for the flower-shaped particles compared to the dumbbell-shaped particles. The first set of anisotropy peaks for the flower particles ($H_{K1} \approx \pm 1650$ Oe for T = 10K) occur at fields three times higher than that for the dumbbell particles ($H_{K1} \approx \pm 560$ Oe). The position of the second set of peaks anisotropy

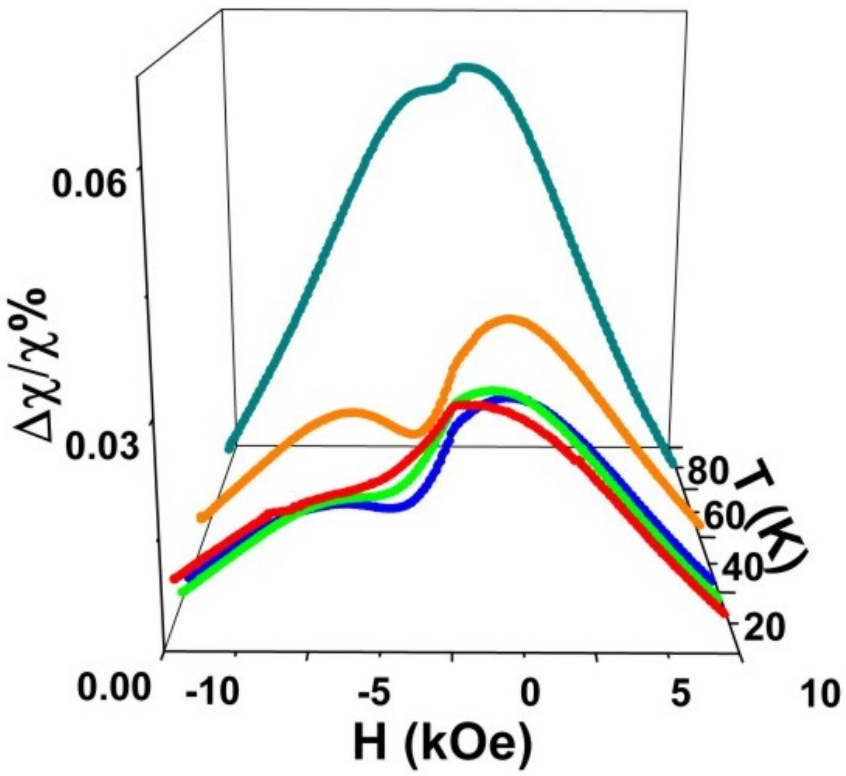

Figure 6.18. Unipolar transverse susceptibility curves of the flower Au-Fe_3O_4 nanoparticles taken at several different temperatures.

peaks for the flower particles ($H_{K2} \approx \pm 4050$ Oe for T = 10K) is over six times higher than the position of the corresponding dumbbell particle anisotropy peaks ($H_{K2} \approx \pm 630$ Oe).

The $\pm H_{K1}$ and $\pm H_{K2}$ for T = 30K (figure 6.19) are ± 1650 Oe and ± 3000 Oe respectively, depending on the +scan or −scan. These values, along with the unipolar data, are consistent with the flower-shaped particles having higher shape and surface anisotropies than the dumbbell-shaped particles. The asymmetry in the peak height, width, and position in the unipolar scan is much more pronounced for the flower particles as well. The fact that there is a much greater discrepancy between H_{K2} peaks of the two types of particles than the H_{K1} peaks is also consistent with the large difference seen in coercivity between the two types of particles since the H_{K2} peak can be correlated with the switching of the particles. It should be kept in mind that peak width can also be correlated with other effects, such as short-range interactions within clusters. The asymmetry of the transverse

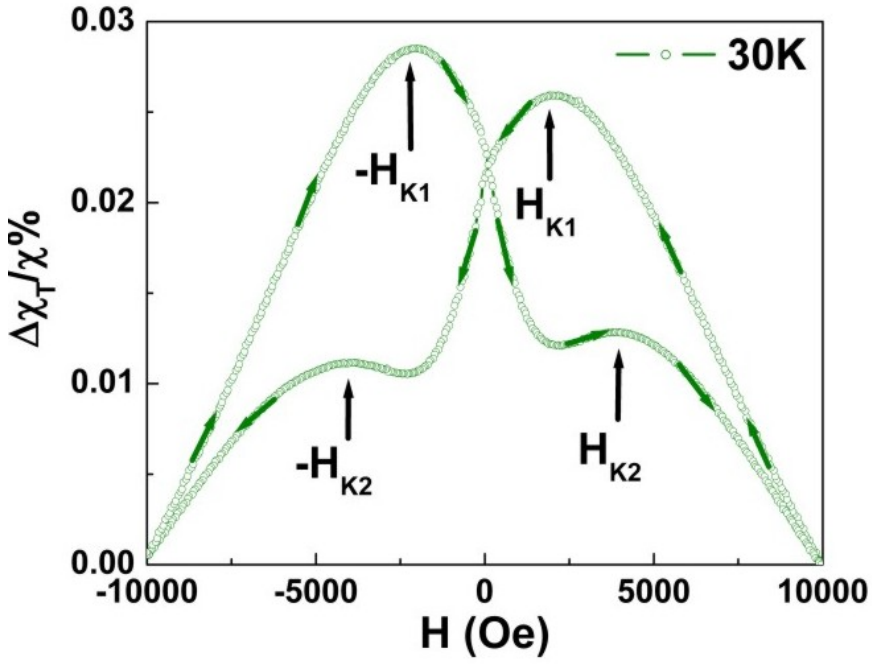

Figure 6.19. Low field portion of a transverse susceptibility scan of the flower Au-Fe_3O_4 nanoparticles taken at 30K. The arrows indicate the sequence of measurement.

susceptibility peaks being higher in the flower particles also can be reconciled with the fact that each flower particle is a compact cluster of Fe_3O_4 nanoparticles bound to a single Au nanoparticle, thus forming a geometry favoring a certain level of short-range interactions between the spins. The presence of such interactions in clusters would make it relatively harder (and the peaks sharper) for collective flipping of the spins as the field polarity is changed during the scans. The relatively lower peak asymmetry in the dumbbells is consistent with the absence of such short-range cluster type interactions.

Figures 6.20 and 6.21 show the evolution of both sets of peaks with temperature for the dumbbell-shaped and flower-shaped particles respectively. The anisotropy fields of both these nanoparticle types decrease with increase in temperature. The striking difference in the first peak (H_{K1}) and second peak (H_{K2}) positions in the flower particles is most evident in this figure when compared to the dumbbell particles, underscoring the role of shape and surface anisotropy in the Au-Fe_3O_4 system.

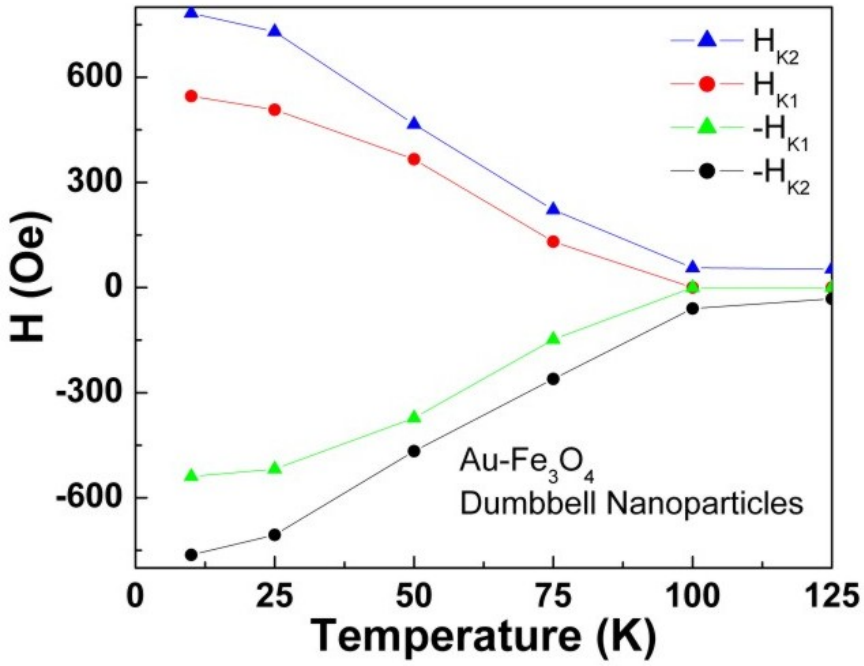

Figure 6.20. Values of $\pm H_{K1}$ and $\pm H_{K2}$ as a function of temperature for the dumbbell Au-Fe_3O_4 nanoparticles.

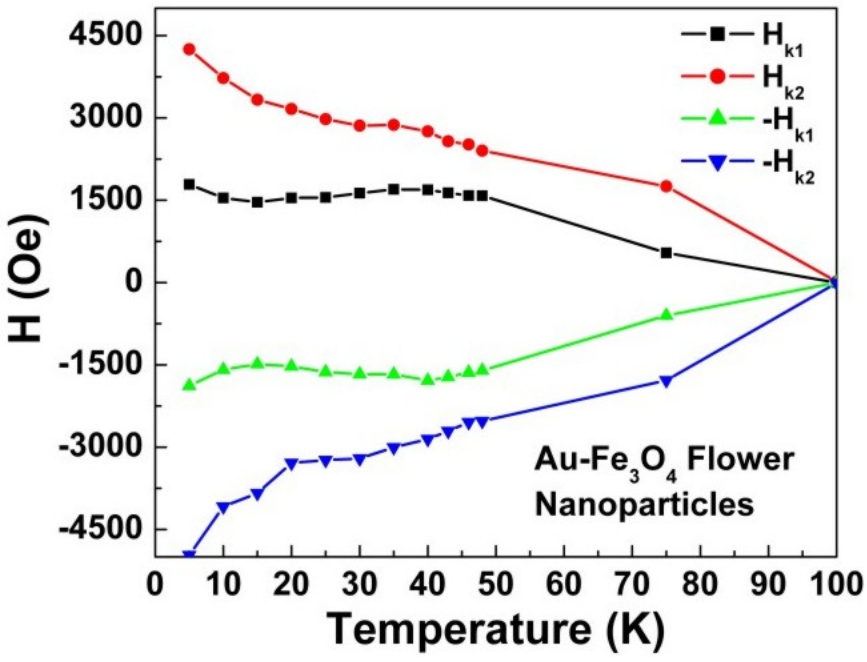

Figure 6.21. Values of $\pm H_{K1}$ and $\pm H_{K2}$ as a function of temperature for the flower Au-Fe_3O_4 nanoparticles.

The exchange bias in the flower nanoparticles was further probed by transverse susceptibility measurements. In comparing the ZFC and 5 Tesla FC transverse susceptibility curves (figure 6.22), we can see that the shapes of the curves and the relative positions of the peaks remained the same, but the curves were horizontally shifted as expected. While the narrower peaks measured in the zero field cooled condition were seen at $H_{K1} \approx \pm 1650$ Oe and $H_{K2} \approx \pm 3000$ Oe, in the field cooled condition case the anisotropy field values were $H_{K1} \approx +1100$ Oe, -1500 Oe and $H_{K2} \approx -2600$ Oe, $+2250$ Oe respectively depending on the positive or negative scan. It is also interesting to note the difference in shape of the transverse susceptibility scans for the FC versus the ZFC case. The FC scans have the narrower peaks. Recall that the width of the peaks depends on the random freezing of spins. In the FC situation, the spins are not randomly frozen; their directions are determined by the field in which they are cooled, thus narrowing the peaks. The difference of H_{K1}'s (i.e. ΔH_{K1}) and H_{K2}'s (i.e. ΔH_{K2}) between the +scan and $-$scan in field cooled transverse susceptibility is a measure of the exchange bias, H_E. The temperature dependence of both ΔH_{K1} and ΔH_{K2} matches very well with the H_E(T) from the M-H data shown in figure 6.10. Our transverse susceptibility study of exchange bias in these nanoparticles represents the first such study in exchange-biased nanostructures.

6.7 Memory Effect in Flower and Dumbbell Nanoparticles

The phenomena associated with the intentional decay of magnetization at one temperature while cooling, and the observation of an imprint of that decay at the same temperature upon warming back up are often referred as "memory" effects. This is because it seems to be that the system retains a memory of its thermal and magnetic history. To perform memory effect measurements on both types of samples, we employed the same experimental procedure that was described by Sun *et al.* [87]. The experiment was conducted by cooling the sample in a 50 Oe field (FC) from 300K at a constant rate of 2 K/min, and measuring the magnetization while cooling. The measurement was stopped at T = 90K, 70K, 50K, 20K, 10K and 2K for the flower particles, and T = 70K, 50K, 20K, 10K and 2K

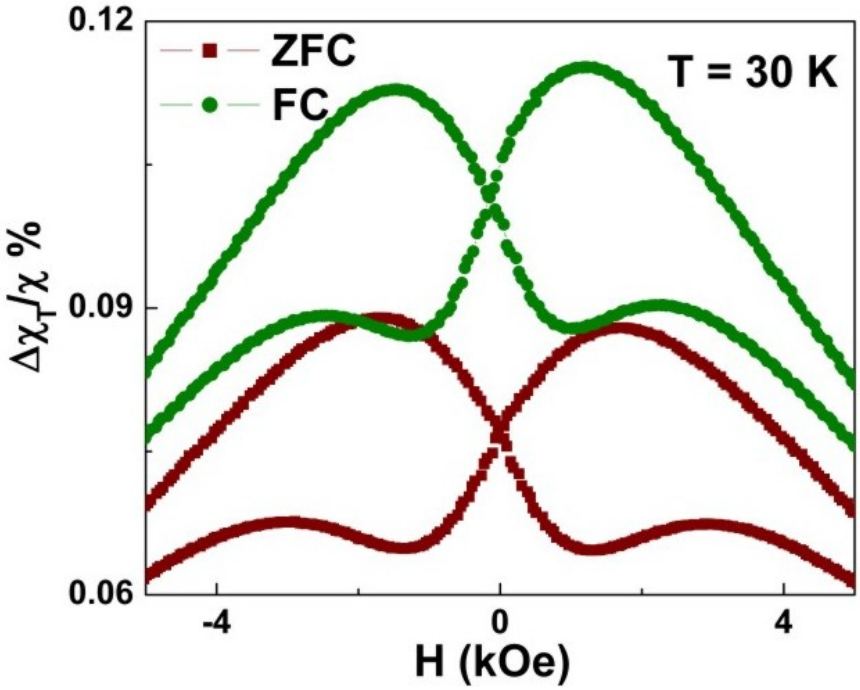

Figure 6.22. Zero field cooled and field cooled transverse susceptibility curves for the flower Au-Fe_3O_4 nanoparticles taken at 30K.

for the dumbbell nanoparticles for a wait time of 2 hours. During that wait time, the field was switched off, and the magnetization was allowed to relax. The solid squares in figures 6.23 and 6.24 were collected in this manner. It can be clearly seen that during the wait time, the magnetization consistently relaxed for T > 20K, indicating the absence of any short range order. However at T = 10K and 2K, after the wait time there is no change in magnetization (even though the field was switched off), indicating that a robust short range order had set in. After reaching the lowest temperature of 2K, the magnetization was measured (open circles) while warming back up (FW) to 300K at the same rate of 2K/min. The M(T) measured during this cycle also shows step-like behavior at the stop temperatures of 50K, 70K and 90K ,indicating that the system can retain memory of its thermal and magnetic history at those temperatures. The memory effect is observed for both the flower and dumbbell nanoparticles. Memory effects have been studied extensively in spin glasses, and have been reported in nanoparticle systems as well [87, 34, 71, 94, 10].

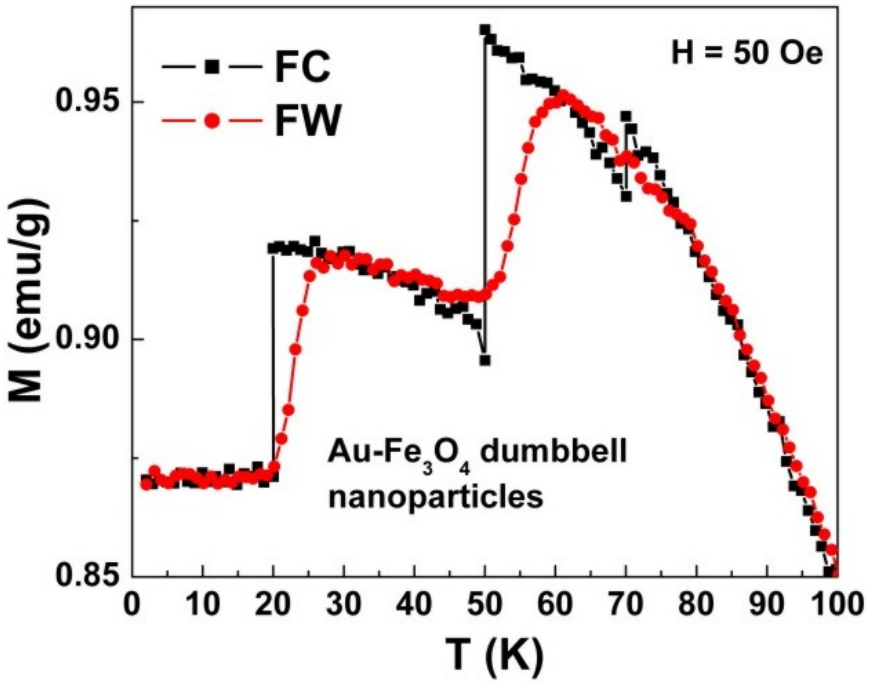

Figure 6.23. Memory effect in dumbbell Au-Fe_3O_4 nanoparticles. Black squares show field cooling, red circles show field warming.

The origin of this memory effect in spin glasses is understood in terms of hierarchal organization of the metastable states as a function of temperature. In nanoparticle systems, the memory effect is attributed more to the distribution of relaxation times arising due to the distribution of particle sizes. For example, when the magnetic field is turned off at 90K, those particles with blocking temperatures above 90K relax easily, while the rest remain aligned with the field. At the next lower temperature, smaller particles with a lower blocking temperature can relax shortly after the removal of a field. This process is repeated for the temperatures at which the memory effects are observed. Upon warming, those particles that relaxed at the lowest temperatures are re-aligned with the field, and so on until all the stop temperatures have once again been reached upon warming. In the present case we have a relatively uniform particle size, but the shape of the composite particles along with inter-particle interactions would lead to a distribution in relaxation times.

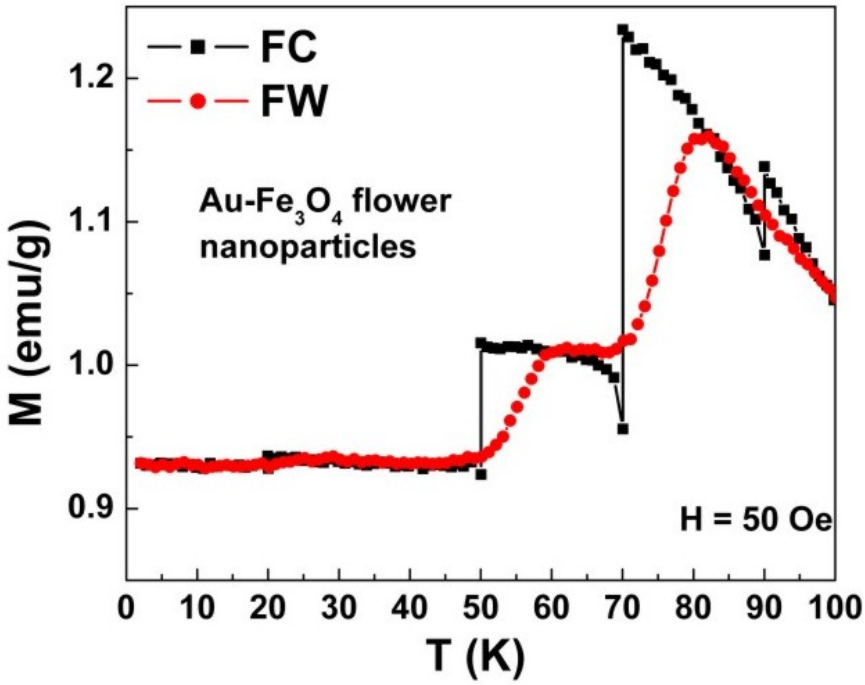

Figure 6.24. Memory effect in flower Au-Fe_3O_4 nanoparticles. Black squares show field cooling, red circles show field warming.

6.8 Origins of Enhanced Anisotropy and Exchange Bias in Flower Nanoparticles

What is clear from the above experiments is that the dumbbell-shaped nanoparticles behave in a much more conventional manner than the flower-shaped nanoparticles, despite the fact that both of these systems are composite nanoparticles. We believe that it is the complex interactions at the multiple surfaces and interfaces of the flower particles that can account for the deviation in magnetic properties between the two systems. In this section, we examine the role of the surface anisotropy and Au-Fe_3O_4 interactions, as well as the interactions between Fe_3O_4 nanoparticles sharing the same Au particles, and correlate these interactions with the behavior observed.

Several groups have focused on anomalous magnetic behavior in ferrite nanoparticles due to surface spin disorder such as exchange-biased hysteresis loops and high field irreversibility [38, 50, 90, 92, 4]. An explanation of this behavior is that when a large enough

fraction of atoms reside on the surface of a particle, the broken exchange bonds are sufficient to induce surface spin disorder, thus creating a core-shell structure made of the ferrite core with a shell of disordered spins. These disordered spins can take on a number of configurations, one of which can be chosen by field cooling the particle to induce a unidirectional anisotropy resulting in a shifted hysteresis loop [38]. It is thought that the lowest energy configuration of surface spins in the zero field cooled condition of a spherical particle is the one in which the spins point out in the radial direction from the particle. Although Bødker *et al.* have demonstrated via symmetry arguments that a perfect spherical particle should have a zero net contribution from surface anisotropy [8], it is important to note that in both dumbbell and flower nanoparticles, the spherical symmetry is broken resulting in a net surface anisotropy. However, the fact that we see no signature whatsoever of a unidirectional anisotropy in the dumbbells suggests that surface anisotropy alone cannot account for the behavior seen in the flower particles. It is possible that the surface spin configuration of the dumbbell particles can explain the spin-glass-like behavior seen in the AC susceptibility data and that other, stronger interactions suppress this behavior in the flower nanoparticles.

In the flower-shaped system, two Fe_3O_4 particles located at opposite ends of the structure are separated by one Au particle, and the three particles as a group form a structure reminiscent of those seen in thin films displaying giant magnetoresistance (GMR). Such multilayer films have two metallic ferromagnetic layers separated by a nonmagnetic metal (unlike the situation described here in which the ferromagnetic phase is insulating). The result is an indirect exchange coupling between the two ferromagnetic layers mediated by the RKKY interaction. The sign and strength of the coupling constant is dependent upon the space between the layers. In the case of the flower nanoparticles, it is possible that the distance between Fe_3O_4 particles (i.e. the radius of the Au particle) sets up a an antiferromagnetic coupling between the Fe_3O_4 nanoparticles reminiscent of this type of exchange (figure 6.25). A similar, indirect ferromagnetic coupling has been observed for adjacent Fe nanodots sharing a metallic (Cu) substrate [65]. In this work, the exchange

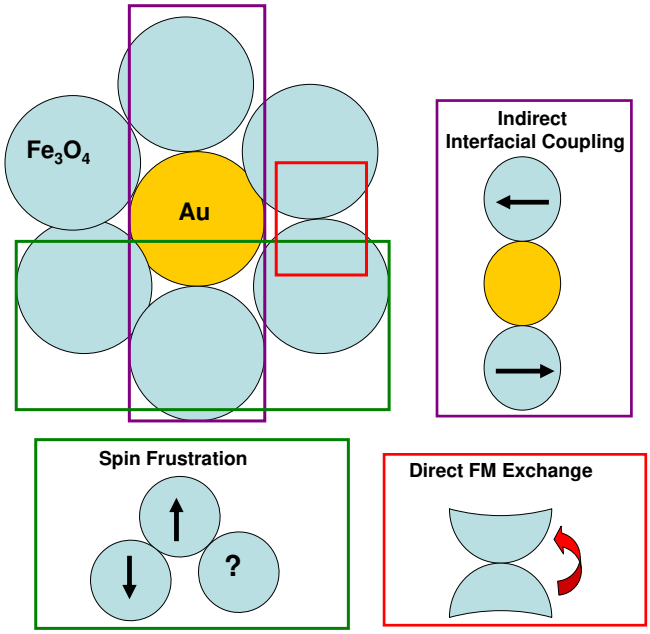

Figure 6.25. Schematic of possible interactions in flower Au-Fe_3O_4 leading to anomalous behavior.

strength could be tuned by changing the distance between nanodots. This tells us that it is reasonable to postulate that at the distances separating the Fe_3O_4 nanoparticles, indirect exchange through the Au-Fe_3O_4 interfaces can result in antiferromagnetic coupling, setting up the unidirectional anisotropy needed to observe exchange bias effects. Just as Pierce *et al.* found that the metal-mediated coupling dominated over anisotropy effects, we believe that the interfacial coupling between the Au and Fe_3O_4 dominates the low temperature behavior seen. However, since there are multiple Fe_3O_4 particles sharing interfaces with the Au particle, this antiferromagnetic coupling could have the added feature of spin frustration. While the magnetization states of two opposite particles are determined by indirect exchange across the Au, they can still be directly adjacent to one another, creating a competition between the metal-mediated exchange and traditional inter-particle interactions. This competition could leave the system frustrated adding to the large anisotropy seen.

It should be emphasized that the anomalous magnetic behavior seen in the flower nanoparticles can be observed below 65K, which is still below the superparamagnetic tran-

sition and consistent with the plateau in the FC curve. We believe this characteristic temperature is due to thermal energy overcoming the energy associated with the Au-Fe_3O_4 interaction. For temperatures below the interaction energy, the antiferromagnetic-type order is robust and we see the exchange bias and training effects. At the thermal activation energy (65K), the coupling is broken and we have a situation where the particles are still in the blocked state and, according to the transverse susceptibility measurements, still show quite a bit more anisotropy than the dumbbell particles. At 75K, the values of H_{K1} and H_{K2} for the flower nanoparticles are 550 Oe and 1770 Oe respectively (figure 6.21), whereas for the dumbbell nanoparticles the H_{K1} and H_{K2} values are 130 Oe and 220 Oe respectively (figure 6.20). This indicates that even after the unidirectional anisotropy is gone, the flower nanoparticles still possess a higher effective anisotropy than the dumbbell particles. Even though the antiferromagnetic coupling has likely been broken, the spin frustration associated with a cluster geometry of Fe_3O_4 may still exist (figure 6.25). It is also possible that rather than possessing broken exchange bonds which normally lead to surface disorder in small ferrite nanoparticles, the nucleating Fe_3O_4 particles making up the "petals" could be growing together into a larger structure, forming exchange bonds with each other, resulting in more of a continuous, cluster-type particle. After projecting a three dimensional particle onto a two dimensional screen when taking a TEM image, it is difficult to tell from figure 6.2 how many of the Fe_3O_4 particles are in direct contact.

6.9 Conclusion

In this chapter, the magnetic properties of two new configurations of Au-Fe_3O_4 were presented. While the dumbbell-shaped Au-Fe_3O_4 did not show behavior that different from traditional Fe_3O_4 nanoparticles, it is still an important system to explore for biomedical applications as two separate surfaces are available for functionalization, and both the Au and Fe_3O_4 sizes can be controlled. It would be interesting to look at various size combinations of Au and Fe_3O_4 to see which combination performs best for functionalization, cellular uptake, and magnetic manipulation while inside the cells.

The flower-shaped nanoparticles proved to be a fascinating system from a fundamental physics point of view due to the combination of competing interactions giving rise to exchange bias and training effects in the low temperature regime, while maintaining an anomalously high anisotropy in the intermediate regime before blocking. In order to fully develop the model briefly proposed by the schematic in figure 6.25, it would be beneficial to look at several different sizes of Au particles to determine the dependence of the interaction strength on the distance between particles. Changing the size of the Fe_3O_4, as well as the number nucleated onto the Au (possibly by making very small changes to the reaction pH), could help form a better picture of the spin frustration likely involved between adjacent Fe_3O_4 particles.

CHAPTER 7

SINGLE LAYER CrO_2 AND BILAYER CrO_2/Cr_2O_3 THIN FILMS

7.1 Introduction

CrO_2 belongs to an important class of oxides. It is ferromagnetic with a Curie temperature of 395K. Band structure calculations have predicted that it is nearly 100% spin-polarized, meaning all of the electrons at the Fermi level have the same spin orientation, and experiments support these predictions [77]. This makes CrO_2 an attractive material for spintronic devices such as spin valves and magnetic tunnel junctions.

Cr_2O_3 is an antiferromagnet with a Néel temperature of 307K. It is the more thermodynamically stable of the two chromium oxide phases. In zero magnetic field, the Cr^{3+} ions are antiferromagnetically aligned parallel to the rhombohedral c axis. When a strong enough external magnetic field is applied along the c axis, the spins switch to lie in the basal plane [57]. Rado *et al.* were the first to experimentally study the existence of both magnetic and electric field-dependent magnetoelectric (ME) effect in Cr_2O_3 powders [68]. The magnetically induced ME effect is manifest as a magnetic-field induced voltage, while the electrically induced ME effect is a magnetic moment that arises in the presence of an electric field. This dual manipulation of one material could have important consequences in the next generation of devices. Cr_2O_3 is also the native oxide that forms on the surface of CrO_2 films and there is evidence that the CrO_2 layer may polarize the Cr_2O_3 layer [14].

Moreover, the multifunctionality of a structure with spintronic and multiferroic properties could be of considerable interest from basic and applied materials perspectives. This chapter describes the growth, characterization, and magnetic properties of CrO_2 thin films and CrO_2/Cr_2O_3 bilayer thin films. We present evidence for exchange coupling between the

layers seen as an increase in anisotropy that cannot be explained by the varying thickness of the CrO_2 phase alone.

7.2 Thin Film Growth

High-quality epitaxial CrO_2 films were grown by Professor Arunava Gupta's group at the University of Alabama MINT Center. Atmospheric pressure chemical vapor deposition (CVD) was used to grow CrO_2 on (100)-oriented TiO_2 substrates using chromium trioxide (CrO_3) as a precursor. In this reaction, oxygen is used as a carrier gas in a two-zone furnace to transport the precursor from the source region to the reaction zone, where it decomposes selectively to form CrO_2. The films were grown at a substrate temperature of about 400°C, with the source temperature maintained at 260°C, and an oxygen flow rate of 100 sccm [43].

It is well known that formation of a natural Cr_2O_3 layer will occur on the CrO_2 surface because it is thermodynamically a much more stable phase than CrO_2 [55]. Because of its metastability, bulk CrO_2 will also irreversibly be reduced to Cr_2O_3 at temperatures higher than about 425°C. The MINT group took advantage of this transformation to grow CrO_2/Cr_2O_3 heterostructures of varying relative thickness. For example, by post-annealing a CrO_2 film at 450°C for varying lengths of time, the film starting from the top surface layer can be controllably converted to Cr_2O_3. All films studied were grown on TiO_2, single crystal (100) substrates, with 5×5 mm^2 dimension, and of varying thicknesses and Cr_2O_3 content. In order to decouple the effect of thickness on magnetic anisotropy from that of interface coupling in bilayers, we have also examined films of CrO_2 with varying thickness in the range of 20nm to 725 nm, whereas the total thickness of the CrO_2/Cr_2O_3 bilayers was kept constant at 200 nm with different proportions of CrO_2 and Cr_2O_3. This does not account, however, for the variation in volume arising due to the difference in density between the two.

The CrO_2 and CrO_2/Cr_2O_3 bilayer films were studied at MINT using a Philips X'Pert x-ray diffractometer and electron microscopy. Dr. Maria Varela and Dr. Stephen Pennycook

of Oak Ridge National Laboratory imaged one of the bilayers using an aberration-corrected scanning transmission electron microscope (STEM). Figure 7.1 shows a cross-sectional STEM image of the CrO_2/Cr_2O_3 bilayers, where it can be seen that the two layers are well-aligned and form an abrupt interface. The Cr_2O_3 layer is crystalline and it is grown epitaxially on top of the CrO_2 with very few defects. The grain boundary defect, which in the figure is marked by an arrow, propagates into the Cr_2O_3 layer directly from the CrO_2 layer. Measurements of the STEM done at Oak Ridge National Laboratory indicated that the (0001) plane of the Cr_2O_3 with a corundum structure is parallel to the (100) plane of the rutile CrO_2. Also, the in-plane [010] and [001] directions of CrO_2 are aligned with the $[11\bar{2}0]$ and $[\bar{1}100]$ directions of Cr_2O_3 respectively. This epitaxial relationship is consistent with what has been observed for the naturally formed Cr_2O_3 surface layer on commercial acicular CrO_2 particles [95].

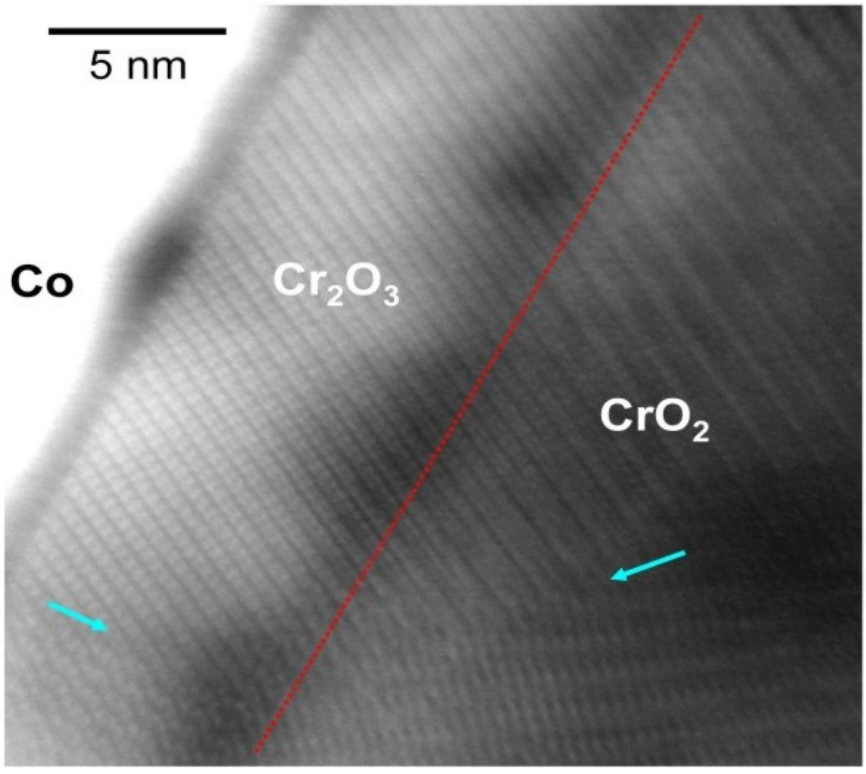

Figure 7.1. Cross-sectional high resolution STEM micrograph of heteroepitaxial CrO_2/Cr_2O_3 bilayer. A grain boundary defect that propagates across the CrO_2/Cr_2O_3 interface is indicated with an arrow. Image courtesy of Oak Ridge National Laboratory.

7.3 DC Magnetic Characterization

Magnetization versus field (M-H) curves were done at the University of Alabama (using an alternating gradient magnetometer), and here at the University of South Florida (using our Physical Properties Measurement System). Figures 7.2 and 7.3 show the M-H curves for the CrO_2 films of 21.5 nm and 725 nm respectively taken at room temperature. Measurements were done along the b axis ([010] direction, red circles) and c axis ([001] direction, black circles). Figure 7.4 shows the room temperature M-H curves for the CrO_2/Cr_2O_3 bilayers. The 100% CrO_2 film corresponds to the 200 nm CrO_2 film, and the inset shows the b axis and c axis data for this sample. The step observed in the hysteresis loops near the saturation field in figure 7.3 is an artifact of the AGM measurement. Miao *et al.* showed in reference [55] that the magnetic easy axis of CrO_2 changes orientation with film thickness. This is attributed to the competition between the magnetocrystalline anisotropy of the CrO_2, and the strain induced by the lattice mismatch with the substrate. The magnetocrystalline anisotropy of CrO_2 favors the magnetic easy axis to orient along the in-plane c direction, as observed both for bulk samples [70], and also for thicker films [43]. The strain anisotropy is an interface effect, and strained thin films grown on (100) TiO_2 substrates exhibit magnetic easy axis alignment along the b direction, since the lattice misfit is larger along the b than in the c direction (3.91% vs 1.44%). Thicker films exhibit inhomogeneous strain distribution, with the magnetic easy axis vector rotating from the b direction near the substrate to the c direction closer to the surface. Consistent with this picture, the M-H curves for the 200 nm and 725 nm films exhibit an easy axis along the [001] direction, and a hard axis along the [010] direction. For the 21.5 nm film, the M-H data indicate an easy axis along the [010] direction, and a hard axis along the [001] direction.

The decrease in saturation magnetization for the bilayer films is due to the decrease in ferromagnetic content (CrO_2) by annealing and conversion to anitferromagnetic Cr_2O_3. The thicknesses of the Cr_2O_3 layers were deduced from the decrease in saturation magnetization (M_S) of the bilayer in comparison to the pure CrO_2 film as the Cr_2O_3 contribution

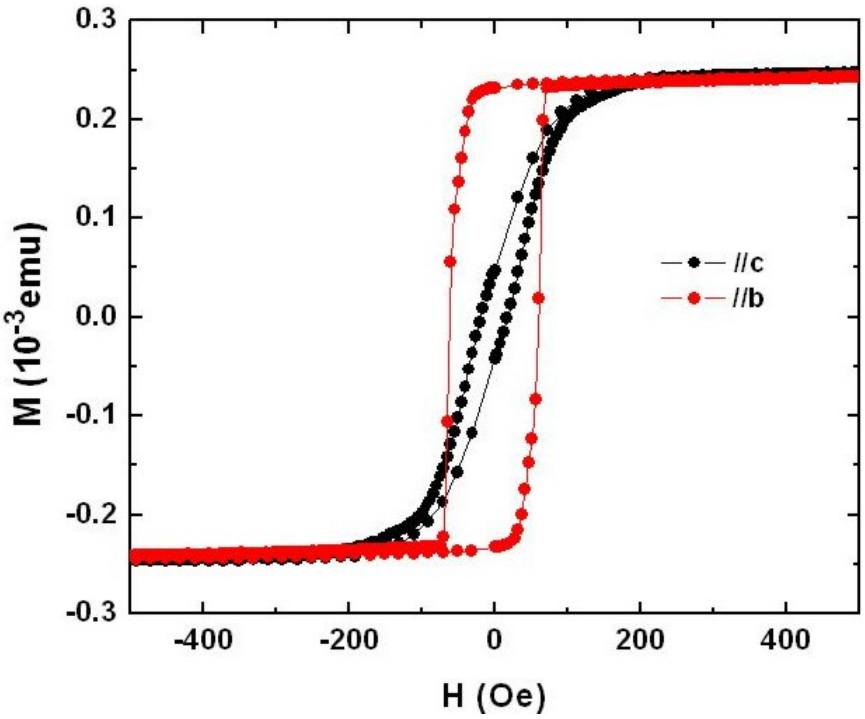

Figure 7.2. Hysteresis loops of 21.5 nm thick CrO_2 film taken along the b and c axes.

to M_S is negligible. The estimated percent content of CrO_2 remaining in different bilayer films measured were 64%, 50%, and 32%. The annealing times for these films were 14h (64% CrO_2), 24h (50% CrO_2), and 34h (32% CrO_2). For all the bilayers, the room temperature M-H curves showed a magnetic easy axis along the [001] direction (c axis), and a hard axis along the [010] direction (b axis).

In figure 7.5 the temperature dependence of the coercivity with variation of CrO_2 content in CrO_2/Cr_2O_3 bilayers is compared to the pure CrO_2 film of the same total thickness of 200 nm. H_C of the bilayers increases in comparison to the pure CrO_2 film depending on the thickness of Cr_2O_3. For the bilayer with 64% CrO_2 content ($\approx$64 nm antiferromagnet thickness), enhancement persists even above the Néel temperature (307K) up to 350K. Increase in H_C above T_N is reported in single crystalline exchange-biased antiferromagnetic FeF_2 films with Co [42] or Fe [23] ferromagnetic layers. This is interpreted as being due to the short range order induced in the antiferromagnet by the ferromagnet. As the CrO_2 (Cr_2O_3) content increases (decreases) the variation in H_C decreases and well

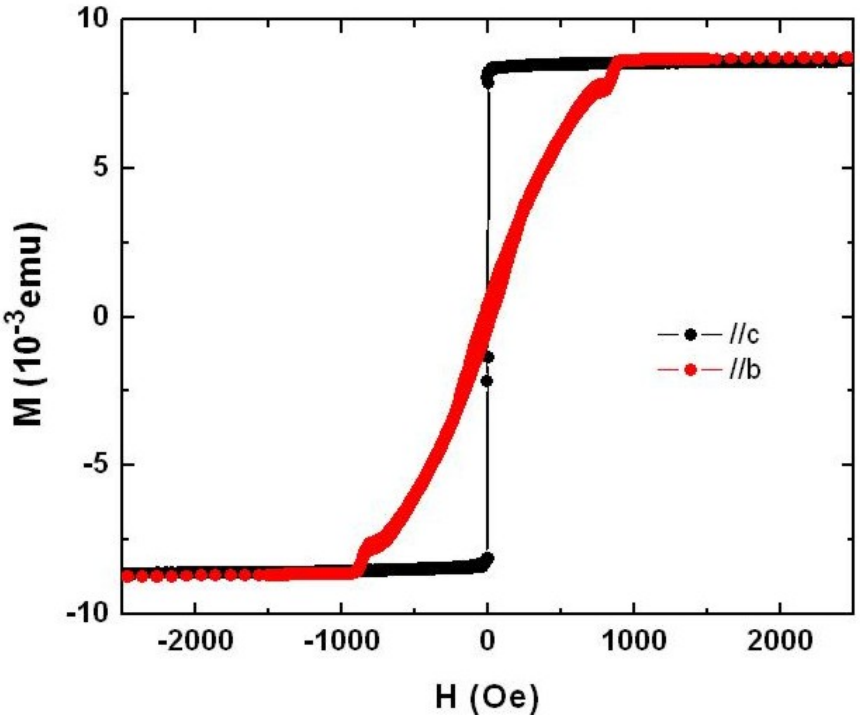

Figure 7.3. Hysteresis loops of 725 nm thick CrO_2 film taken along the b and c axes.

above the Néel temperature it becomes equal to that of the pure CrO_2 film. The inset of figure 7.5 shows the variation of H_C with CrO_2 content at room temperature. H_C increases from 47 Oe for the 100% CrO_2 film of 200 nm to 174 Oe for the bilayer film with 64% CrO_2, and with further decrease in CrO_2 content H_C decreases. The films with 50% and 32% CrO_2 content have H_C values of 145 Oe and 83 Oe respectively. H_C for the CrO_2 films alone is inversely proportional to the ferromagnetic thickness (t_{FM}). The enhancement and functional dependence of H_C on t_{FM} in the bilayer films strongly suggests the existence of a coupling between the CrO_2 and Cr_2O_3 layers. To further probe the nature of the coupling, we measured the hysteresis loops of the bilayer samples after cooling them from above the Néel temperature in a field of 1 Tesla. We did not see any shift in M-H even at 10K except for one film with 32% CrO_2 (64 nm), for which a very small exchange field of 12 Oe was observed. This implies that the exchange coupling mechanism in this system is primarily manifest in the enhancement of H_C, and not accompanied by a shift in M-H (H_E).

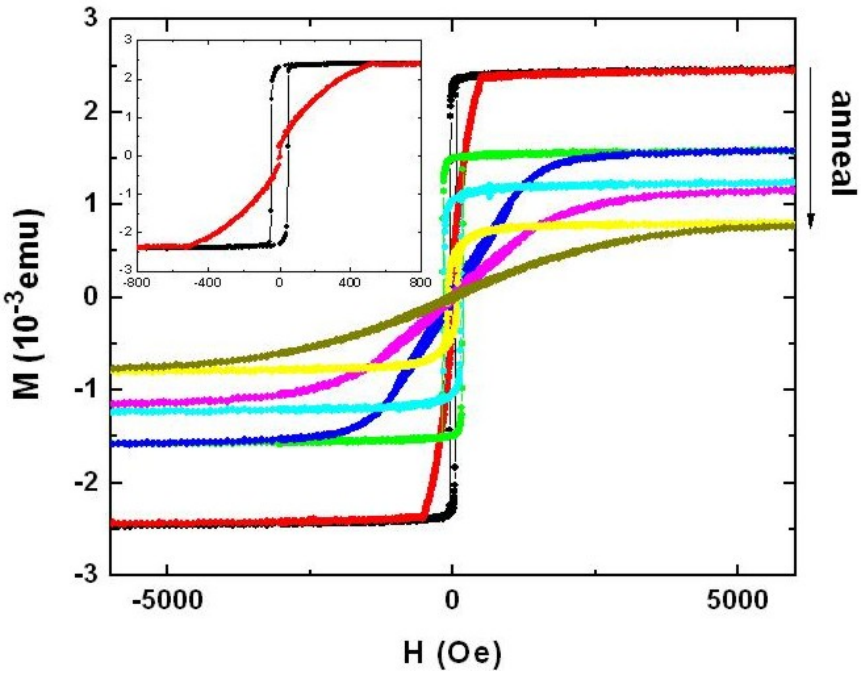

Figure 7.4. Hysteresis loops for CrO_2/Cr_2O_3 bilayers of varying CrO_2 content. Inset shows the hysteresis loops for the 100% 200 nm CrO_2 film taken along the b and c axes.

The role of thickness of the antiferromagnetic and ferromagnetic layers in a number of exchange-biased systems has been studied in detail. In general either the ferromagnetic layer or the antiferromagnetic layers only varied, and the main results of these studies indicate that the exchange bias, H_E, and coercivity, H_C, are inversely proportional to the thickness of the ferromagnetic layer [59]. Furthermore, H_E and H_C are independent of antiferromagnetic thickness (t_{AFM}) for thick films, and H_E abruptly decreases and goes to zero for small t_{AFM} [59]. In the CrO_2/Cr_2O_3 system, the functional dependence of H_E and H_C on t_{FM} and t_{AFM} is rather complicated as t_{FM} and t_{AFM} are varying simultaneously. It is the total thickness (200 nm) of the bilayer which is held constant. Apart from this, the t_{FM} falls in the range of CrO_2 thickness wherein both the inhomogeneous strain and the magnetocrystalline anisotropy compete, and the easy axis switches with both thickness and also temperature. This point will be further discussed in subsequent sections.

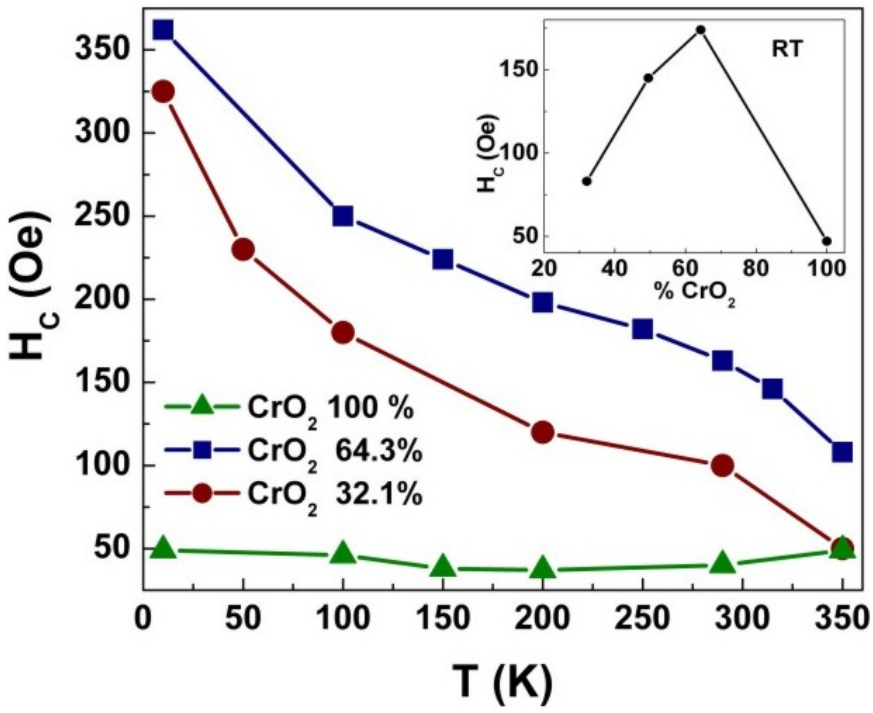

Figure 7.5. Variation of coercivity as a function of % CrO_2 in CrO_2/Cr_2O_3 bilayer films.

7.4 Transverse Susceptibility Measurements for CrO_2 Films

In figure 7.6 we present the unipolar (positive to negative saturation) field-dependent change in transverse susceptibility (χ_T) obtained for the CrO_2 films with different thicknesses at room temperature with the static magnetic field, H_{DC}, applied along the hard in-plane axis of magnetization (c axis for the 21.5 nm film, b axis for 200 nm and 725 nm films). Identical anisotropy peaks are seen in χ_T symmetrically located around H=0, followed by an approach to saturation at higher fields. This is different than the data we saw for the nanoparticle systems, because here we can discern one distinct anisotropy field, which is symmetric regardless of direction of transverse susceptibility scan (i.e. $H_{K1} = H_{K2} = H_K$). We also do not see a separate switching peak along the hard axis, because as the out-of-plane hysteresis loops indicate, the switching field and anisotropy field are very nearly equal. The anisotropy peak height increases with increase in film thickness. An increase in the anisotropy field, H_K, with increase in film thickness is also observed. Using

the standard relation $H_K = 2K_{\text{eff}}/2M_S$, we extracted the effective anisotropy K_{eff} at room temperature. CrO_2 films are known to have a prominent in-plane uniaxial anisotropy, leading to the assumption that $K_{\text{eff}} \approx K_1$ [79]. Furthermore, transverse susceptibility performed on thin CrO_2 films grown from the same group in 2000 revealed that the magnetization rotation could be successfully reproduced using a coherent rotation model, resulting in behavior very similar to a Stoner-Wohlfarth particle [79]. Using H_K=80 Oe and M_S = 465 emu/cc, we calculated K_{eff} as 1.9×10^4 erg/cc for the 21.5 nm CrO_2 film. Using the same procedure, we calculated K_{eff} values for the 200 nm and 725 nm CrO_2 films as 1.1×10^5 erg/cc (H_K = 514 Oe) and 2.5×10^5 erg/cc (H_K = 1050 Oe) respectively. These results agree well with the values obtained by Miao *et al.* in their thickness dependent study of K_{eff} in CrO_2 films using DC magnetic measurements [55].

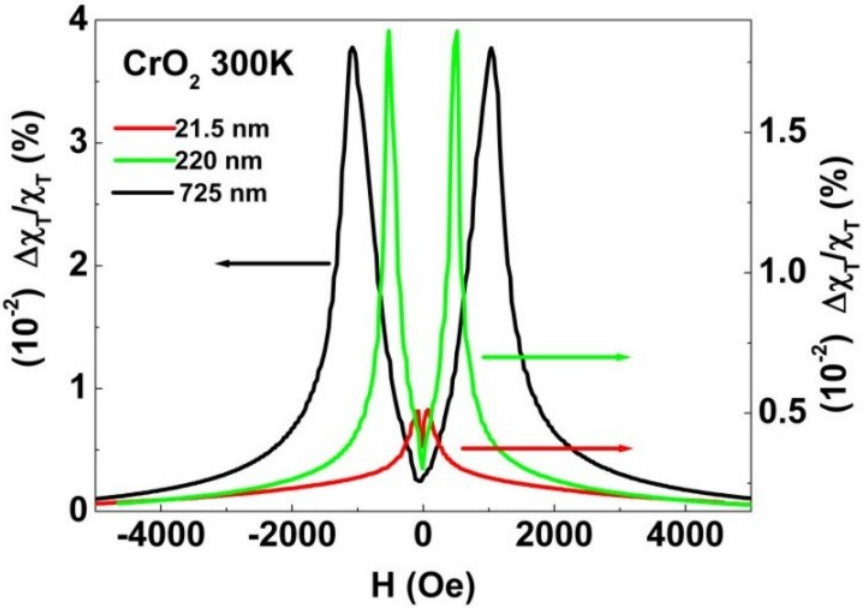

Figure 7.6. Unipolar transverse susceptibility data for CrO_2 films of varying thicknesses taken at room temperature. Scan was taken from positive to negative saturation.

At 10K, the H_K and K_{eff} don't show the same increase in value with increase in thickness (figure 7.7). The 725 nm film still has the highest H_K (1340 Oe) and K_{eff} (4.3×10^5 erg/cc), but the 21.5 nm films has a higher H_K (815 Oe) and K_{eff} (2.6×10^5 erg/cc) than the 200 nm film (390 Oe and 1.2×10^5 erg/cc). The room temperature magnetic properties and

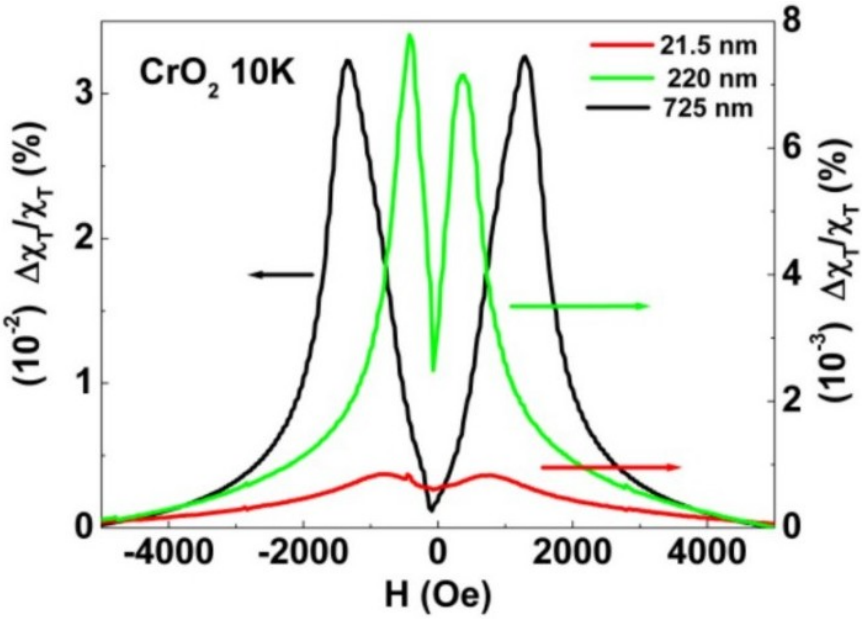

Figure 7.7. Transverse susceptibility data for CrO_2 films of varying thicknesses taken at 10K. Scan was taken from positive to negative saturation.

low temperature magnetic properties are collected in table 7.1. The low temperature M_S values were taken from reference [55]. The films used in that study were also grown by Professor Gupta's group, so the two sets of films can be compared with confidence.

CrO_2 thickness (nm)	M_S (emu/cc) (RT)	H_K (Oe) (RT)	K_{eff} (erg/cc) (RT)	M_S (emu/cc) (LT) Ref. [55]	H_K (Oe) (LT)	K_{eff} (erg/cc) (LT)
21.5	465	80	1.9×10^4	640	815	2.6×10^5
200	436	514	1.1×10^5	640	390	1.2×10^5
725	486	1050	2.6×10^5	640	1340	4.3×10^5

Table 7.1. Magnetic properties of CrO_2 films at room temperature (RT) and low temperature (LT).

In order to understand this complex thickness dependence on the anisotropic properties, transverse susceptibility measurements were done over the full range of temperatures and the H_K values are plotted in figure 7.8. For the 21.5 nm and the 725 nm films, the peak position shifts to higher fields as the temperature decreases. The temperature variation is dominated in the 21.5 nm film by strain effects from the substrate, which introduces a

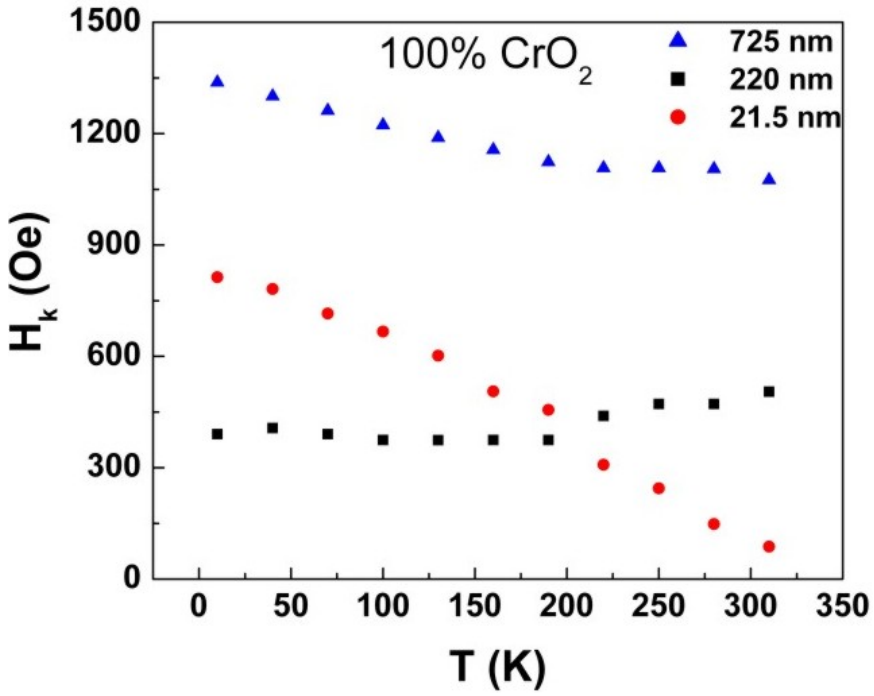

Figure 7.8. Temperature dependence of H_K for various thicknesses of CrO_2.

magnetoelastic term to the effective anisotropy. The 725 nm film will behave the closest to a bulk sample where the magnetocrystalline anisotropy will dominate, and an increase in anisotropy with decrease in temperature is what is expected for most bulk systems [70]. For the 200 nm film there is a slight increase in H_K with increase in temperature. This intermediate thickness film should have the most competition between strain anisotropy and magnetocrystalline anisotropy, and in fact it falls within the range (50-250 nm) reported by Miao *et al.* where these competing anisotropies induce a change in easy axis of magnetization. The transverse susceptibility measurements presented here seem to also display a temperature dependent switching of easy axis due to the inhomogeneous strain distribution, resulting in a decrease in anisotropy field at lower temperature.

Interestingly, the 200 nm thin film also shows a double switching feature consistent with the findings reported in reference [55], likely due to the large presence of both strain and magnetocrystalline anisotropies favoring different magnetic easy axes. While the H_K measurements for the 200 nm film for the temperatures shown in figure 7.8 were all done

with H_{DC} along the [010] direction, systematic measurements done with H_{DC} along the [001] direction showed that the c axis was an easy axis at room temperature (consistent with figure 7.4) but that as the temperature was lowered, it became a hard axis of magnetization. Figure 7.9 shows transverse susceptibility scans with H_{DC} along the c axis for several different temperatures. While just one peak at the switching field is seen at room temperature, anisotropy peaks begin to emerge as the temperature decreases. The [001] peaks appear different from the [010] peaks because the [010] peaks behave as expected for a thin film measured along the hard axis, that is, the anisotropy peaks are sharp and coincide with the switching peak. The [001] peaks behave more as if the anisotropy fields have a slight distribution and a separate switching field manifest as a separate peak closer to $H = 0$. This is consistent with the emergence of the [001] being strain-related and inhomogeneous, so that the easy axis is rotating throughout the thickness of the film. This could give rises to slight distribution in H_K which is not equal to H_S. The increase in anisotropy associated with the presence of these peaks when the temperature is lowered as H_{DC} is applied along the c axis could help to explain the anomalous decrease in anisotropy with decrease in temperature as H_{DC} is applied along the b axis. As expected, neither the 21.5 nm film nor the 725 nm film showed this behavior at low temperatures when H_{DC} was applied along their respective easy axes.

7.5 Transverse susceptibility Measurements for CrO_2/Cr_2O_3 Bilayers

Transverse susceptibility measurements were carried out on all bilayer samples by applying the H_{DC} parallel to the hard [010] axis. First, transverse susceptibility was measured on a fully decomposed sample to look at the signal due to Cr_2O_3 only. As expected for antiferromagnetic materials, a single sharp peak was present at H=0 and the curves did not flatten out at high fields, indicative of a failure to reach saturation. Non-saturating magnetization is a known feature of antiferromagnetic materials that is also commonly observed in M-H curves. We observe a distinct asymmetry in the shape of the curves for negative and positive field polarities. This could be associated with slightly different responses of

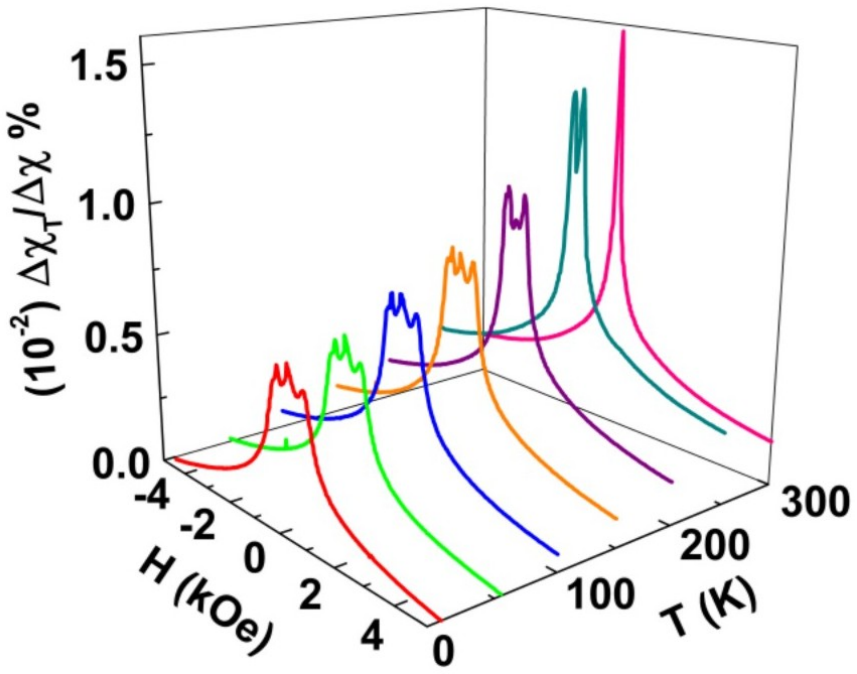

Figure 7.9. Unipolar transverse susceptibility scans of 200 nm CrO_2 film for several temperatures showing anisotropy peaks emerging as the temperature is decreased. Here H_{DC} is applied along the [001] direction from positive to negative saturation.

the sublattice magnetization components of the antiferromagnetic order when the field is reversed. While this is generally not seen in DC magnetization measurements (which is a volume magnetization measurement), the transverse susceptibility geometry, which probes the transverse component of the magnetization vector, is highly sensitive to the influence of the sublattice magnetization energy.

The transverse susceptibility measurements on the bilayers interestingly exhibit combined features associated with both the ferromagnetic CrO_2 (anisotropy peaks), and antiferromagnetic Cr_2O_3 (peak at H=0, as well as the nonsaturation and asymmetry discussed earlier). The transverse susceptibility data for all the samples containing different amounts of CrO_2 percent content at room temperature is presented in figure 7.10. The most noticeable feature of the bilayer data is the shift in the anisotropy peaks to higher fields as the content of Cr_2O_3 increases. The anisotropy peaks are not as sharp as in the case for CrO_2, but appear as broad shoulders about the center peak. The broadening becomes

more pronounced with increase in Cr_2O_3 until at 32% CrO_2, anisotropy peaks can barely be made out. There is also a prominent strain-associated peak that appears and becomes more prominent at lower temperatures (figure 7.13). The emergence of peaks which can be associated with strain was also seen by Spinu *et al.* in transverse susceptibility data of CrO_2 thin films [79]. This behavior can be explained in terms of a slight deviation of the anisotropy axis from the hard axis of magnetization and was successfully modeled by introducing a magnetoelastic term into the total anisotropy energy.

H_K for the 200 nm 100% CrO_2 film is ≈515 Oe, whereas for the film with 32% CrO_2 it is ≈2100 Oe. The shift in anisotropy peaks to higher fields with decrease in CrO_2 content for the bilayers implies a change in effective anisotropy (K_{eff}). It is important to verify if the increase in H_K corresponds to an increase in K_{eff} after taking into account the corresponding M_S of the t_{FM}. The t_{FM} values based on the percent content of CrO_2 was calculated, and is presented in tables 7.2 and 7.3. The corresponding K_{eff} for these thicknesses is obtained by a fit to a curve based on data in reference [55] (figure 7.11). When comparing the observed room temperature K_{eff} values with those calculated based on t_{FM}, it is clear that the observed K_{eff} is consistently larger than what it would be if the Cr_2O_3 were not present in the films. The maximum K_{eff} (2.4×10^5 erg/cc) was obtained for a bilayer film with 50% content of CrO_2, which is much larger in comparison to the K_{eff} extracted from the curve (6.2×10^4 erg/cc). The results for all the films are given in table 7.2. For the pure CrO_2 films, H_K is proportional to CrO_2 thickness (table 7.1), while for the bilayers, H_K is inversely proportional to the t_{FM} (table 7.2). The role of Cr_2O_3 and its interface with CrO_2 is manifest not only by the enhancement of H_K, but also by its functional dependence with t_{FM}.

The temperature dependence of H_K for the bilayers is plotted in figure 7.12. For all bilayer films, an increase in H_K with decrease in temperature is observed. This indicates that the presence of Cr_2O_3 changes the temperature dependence of the strain in comparison to the pure CrO_2 films, thus the easy axis of magnetization remains along the c axis throughout the temperature range. This is also evident from the absence of the anisotropy

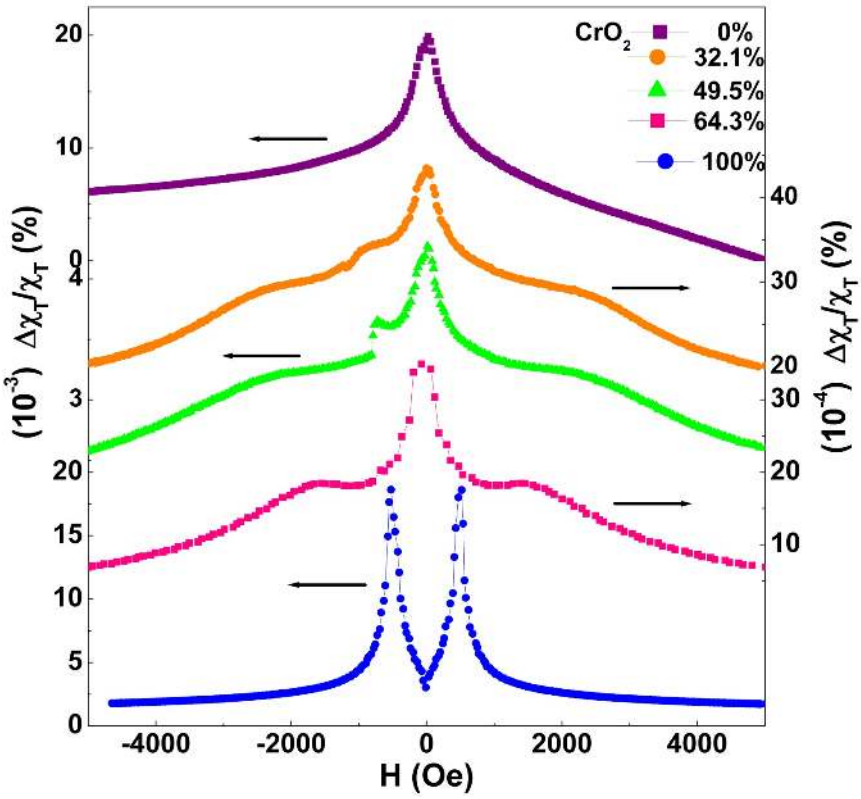

Figure 7.10. Room temperature transverse susceptibility scans of CrO_2/Cr_2O_3 bilayers for different CrO_2 percentages. Scan taken from positive to negative saturation.

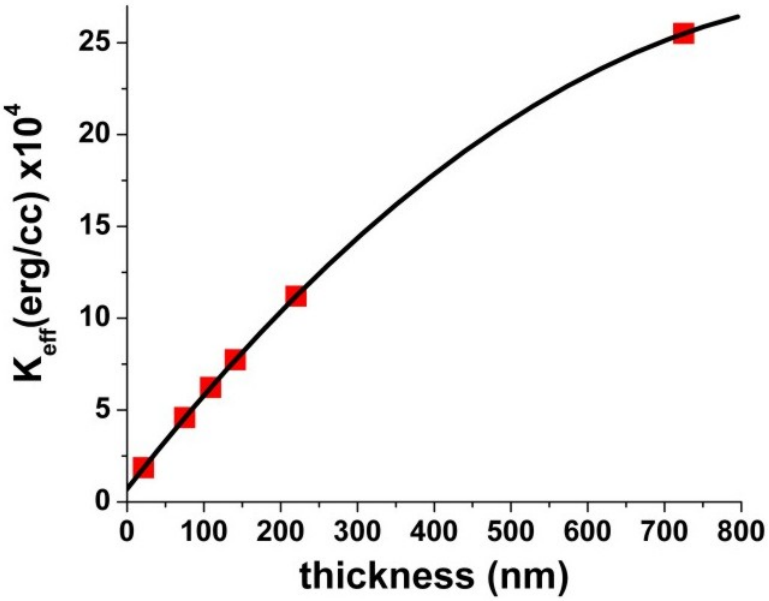

Figure 7.11. K_{eff} versus CrO_2 thickness for the films studied here and in ref [55]. This is used for a reference curve to predict values of K_{eff} for the effective CrO_2 thickness in the bilayers.

peaks throughout the temperature range when the transverse susceptibility is measured with the applied field parallel to the easy (b) axis. Similar to the room temperature measurements, H_K increases with increase in Cr_2O_3 content throughout the measured temperature range. While the values of K_{eff} for the CrO_2 thin films matched well with those reported in reference [55], the K_{eff} values for the bilayers were consistently larger throughout the temperature range, again indicating a coupling between the layers. As we saw in chapter 6, transverse susceptibility can be used to probe systems showing exchange bias due to unidirectional anisotropy, and there was no shift in the transverse susceptibility for the bilayers, which is consistent with the lack of shift observed in the M-H loops.

Table 7.3 is a collection of the low temperature (10K) values of H_K and K_{eff}. From figure 7.12, we can see that H_K is highest at low temperature, but from table 7.3 it can be clearly seen that this translates into an increase in K_{eff} as well. Figure 7.13 shows a low temperature (36K) transverse susceptibility scan of the bilayer with 64% CrO_2. The strain-associated peak discussed above is much more noticeable at low temperature. For

% CrO_2	Effective thickness (nm)	M_S (emu/cc) (RT)	H_K (Oe) TS (RT)	K_{eff} (erg/cc) (observed) (RT)	K_{eff} (erg/cc) (calc)	H_K (Oe) (calc)
100	200	436	514	1.1×10^5	1.1×10^5	514
64	128	291	1448	2.1×10^5	4.6×10^4	314
50	99	227	2075	2.3×10^5	6.2×10^4	548
32	64	136	2100	1.4×10^5	7.7×10^4	1136

Table 7.2. Magnetic properties of CrO_2/Cr_2O_3 bilayer films of different Cr_2O_3 content measured at room temperature (RT). The calculated values correspond to what the effective anisotropy should be for just the CrO_2 component according the reference in figure 7.11.

% CrO_2	Effective thickness (nm)	H_K (Oe) (TS) (10K)	M_S (emu/cc) (10K)	K_{eff} (erg/cc) (10K)
100	200	390	660	1.3×10^5
64	128	2130	423	4.5×10^5
50	99	3150	326	5.1×10^5
32	64	3230	212	3.4×10^5

Table 7.3. Magnetic properties of CrO_2/Cr_2O_3 bilayer films of different Cr_2O_3 content measured low temperature (LT).

this particular sample, the strain peak was not present at room temperature. The other two samples, which did show strain peaks in figure 7.10, also showed the strain peak evolving further as the temperature is decreased.

7.6 Origins of Exchange Coupling in CrO_2/Cr_2O_3 Bilayers

To observe an exchange bias (H_E), the spins in the antiferromagnet must not be rotated by the magnetic field applied. Therefore, the anisotropy energy of the antiferromagnet must be larger that the interface coupling energy,

$$4\sqrt{A_{AFM}K_{AFM}}/\pi^2 < K_{AFM}t_{AFM}$$

where A_{AFM} and K_{AFM} are the exchange stiffness ($\approx$4x10^{-7} erg/cc for Cr_2O_3) and the anisotropy constant ($\approx2\times10^5$) [95]. This gives a minimum antiferromagnetic thickness requirement of 5.73 nm. Since our t_{AFM} values are all much larger than this ($t_{AFM} > 64$

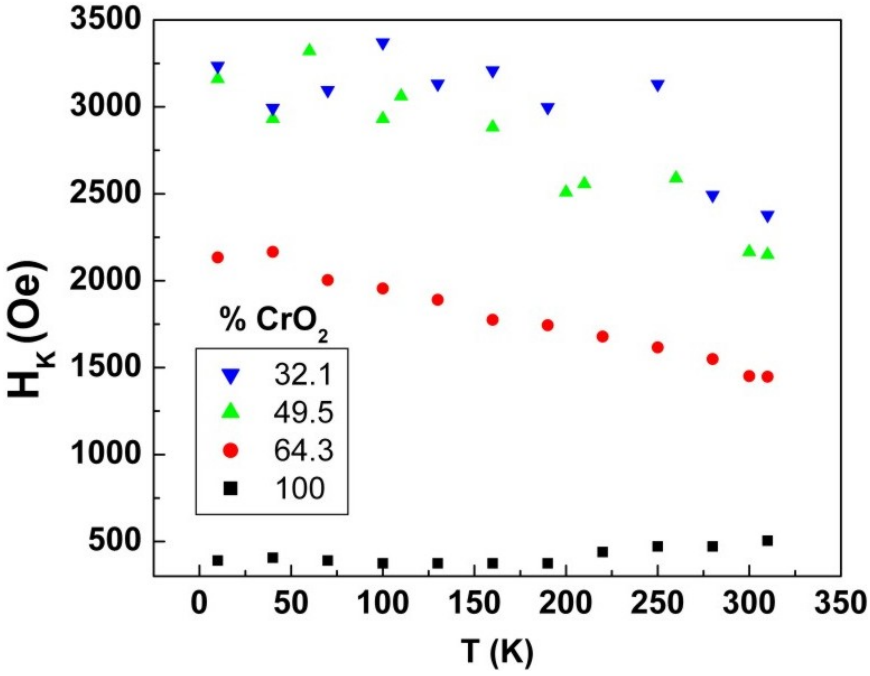

Figure 7.12. H_K versus temperature for the CrO_2/Cr_2O_3 bilayers.

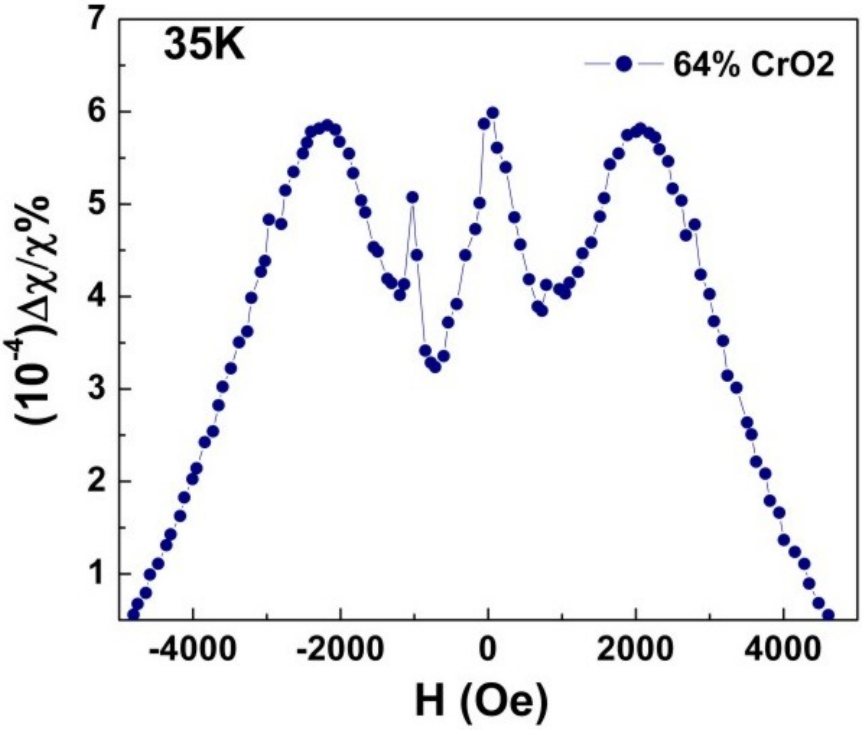

Figure 7.13. Low temperature (36K) transverse susceptibility scan of 64% CrO_2 bilayer. This is a portion of a scan taken from positive to negative saturation.

nm), the antiferromagnetic spins should be pinning the ferromagnetic spins, giving rise to a unidirectional anisotropy. Clearly from the data shown, there is no unidirectional anisotropy, only a uniaxial anisotropy.

The behavior observed in the CrO_2/Cr_2O_3 bilayers can in fact be understood in terms of a model put forth by Schulthess *et al.* [72]. The model applies to systems with compensated spins at the interface, i.e. when there is an equal number of positive and negative exchange interactions across the interface, which would apply to the nearly perfect epitaxy seen in the CrO_2/Cr_2O_3 bilayers. In such a system, the exchange coupling between the antiferromagnet and the ferromagnet is perpendicular. This perpendicular coupling, referred to as "spin-flop" coupling, fits within a microscopic Heisenberg model where, due to frustration of the moments at the interface, the ferromagnet minimizes the energy when it aligns perpendicular to the antiferromagnetic easy axis. This type of coupling will not lead to a unidirectional anisotropy because the antiferromagnetic spins at the interface will not pin the ferromagnetic spins when cooled from above the Néel temperature in the presence of a field. Instead, since the spins will be perpendicular, the antiferromagnetic spins will "drag" the ferromagnetic ones, leading to a uniaxial anisotropy, and thus an enhanced coercivity. Figure 7.14 is a schematic of this model, which shows the bulk antiferromagnetic spins (bottom), the interfacial antiferromagnetic films (middle), and the ferromagnetic spins (top). The antiferromagnetic spins do not rotate except for small disturbances very near to the interface.

Recall that both the total thickness of the bilayers (200 nm), and all the effective CrO_2 thicknesses fall into the region of CrO_2 which exhibit a doubling switching phenomenon due to the inhomogeneous strain distribution caused by the substrate. Hence the magnetization of the bilayers is the result of the inhomogeneous strain caused by the substrate at one end and the exchange coupling with the antiferromagnetic Cr_2O_3 at the other end. This is likely the origin of the large strain-induced peak seen for all the bilayer films. Another striking feature of the combined analysis of the M-H and transverse susceptibility on the bilayer system is the variation of H_C and H_K with t_{FM}. Thus the Cr_2O_3 presence in the

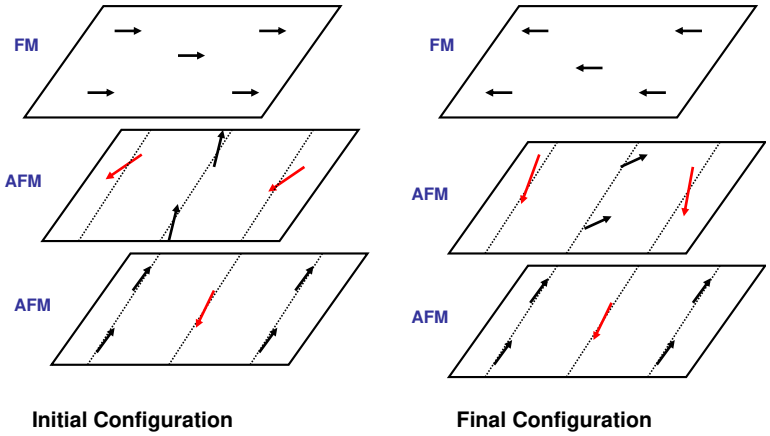

Figure 7.14. Schematic of spin-flop coupling model. Adapted from reference [72].

bilayer affects the two most important magnetic properties, the switching field and the anisotropy field, establishing the coupling between the CrO_2 and Cr_2O_3 layers.

It should also be noted that CrO_2/Cr_2O_3 system is an exchange-coupled system in which the top layer is a magnetoelectric antiferromagnet. Recently, magnetoelectric switching of an exchange bias was shown in $Cr_2O_3/(CoPt)_3$ [9], wherein the Co/Pt multilayers were grown on Cr_2O_3 single crystals of 0.7 mm thickness. The direction of the exchange bias (or the horizontal shift of M-H) could be switched by cooling the sample from above the Néel temperature in an external *electric* field either parallel or antiparallel to the cooling DC magnetic field. So apart from the exchange coupling, magnetoelectric coupling of Cr_2O_3 to the ferromagnetic may contribute to the variation in H_C and H_K. Testing for magnetoelectric coupling would require large electric fields to be present inside the PPMS, which is not something we are currently capable of doing. Future work will focus on the completion of a probe designed to measure complex impedance, where the magnetic and dielectric response functions can be simultaneously measured inside of the PPMS.

7.7 Conclusion

We have presented in this chapter a compelling case for exchange coupling of CrO_2/Cr_2O_3 bilayers through a uniaxial anisotropy rather than the unidirectional anisotropy normally associated with exchange-coupled systems. This uniaxial anisotropy is manifest as a modest increase in H_C and a substantial increase in H_K measured with transverse susceptibility. We were successfully able to rule out a simple ferromagnetic thickness dependence by measuring several different thicknesses of CrO_2 films, meanwhile providing more evidence of strain-induced double switching in the CrO_2 films. We also proposed that the lack of unidirectional anisotropy in the bilayers is likely due to perpendicular spin-flop coupling between the Cr_2O_3 and the CrO_2.

CHAPTER 8

BARIUM HEXAFERRITE/BARIUM STRONTIUM TITANATE MULTILAYER THIN FILMS

This chapter contains a summary of the author's work for her master's thesis [18] and the publications that followed [19, 84]. Growth of one batch of thin films along with some of their structural characterization was done at Dr. Nancy Dudney's laboratory at Oak Ridge National Laboratory by the author as a visiting student. A second batch of thin films was grown in Dr. Kevin Coffey's laboratory at the University of Central Florida. All post-annealing and magnetic characterization was done at the University of South Florida.

8.1 Introduction

As discussed in the opening chapters, multiferroic materials, or those possessing both ferroelectric and magnetic ordering, have seen a renewed interest as of late due to the dual functionality and interesting coupled properties they display. While single phase multiferroics are being intensely studied for fundamental physics, it is becoming more popular to synthesize composites and multilayer structures of ferroelectrically and magnetically ordered phases where it is possible to engineer the material for a desired application by means of modifying its chemical composition, microstructure and layer morphology. Growing magnetic/ferroelectric multilayers is promising due to the significant control one has over the growth process. This results in the ability to optimize growth parameters to achieve the desired thickness, and microstructure including grain size and shape. In this chapter, we present results on the magnetic properties of multilayer thin films of $BaFe_{12}O_{19}$ and $Ba_{(1-x)}Sr_xTiO_3$, two very important materials used in microwave devices.

The compound $BaFe_{12}O_{19}$ (Barium-hexaferrite, BaM) is an important ferrite, and is used in a variety of magnetic recording [33] and high-frequency applications such as isolators, filters, phase shifters, and circulators [27]. It belongs to the M-type class of hexagonal ferrites (hexaferrites). This type of hexagonal ferrite has a magnetoplumbite crystal structure, shown in figure 8.1, which consists of four interchanging spinel (S and S*) and rhombohedral (R and R*) blocks. The asterisk means that the corresponding block has been turned 180° around the hexagonal c-axis. The ferrimagnetic properties come entirely from the 24 Fe^{3+} ions, each having a magnetic moment of $5\mu_B$ (μ_B: Bohr magneton), and the total magnetic moment is $40\mu_B$ [52]. The lattice parameters of the unit cell of BaM are $a \approx$5.89Åand $c \approx$23.19Å [91]. The most outstanding property of BaM is its large magnetic anisotropy [76]. The easy direction of magnetization is along the hexagonal c-axis, and the hard direction is along the hexagonal a-axis.

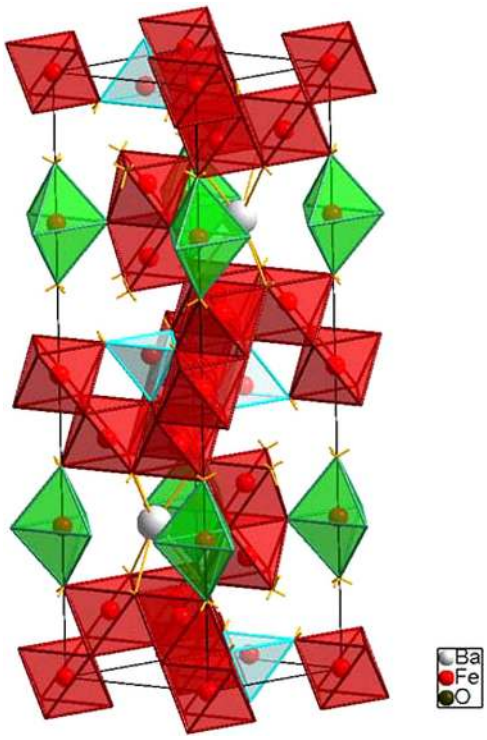

Figure 8.1. Crystal structure of Barium Hexaferrite. Figure adapted from reference [27].

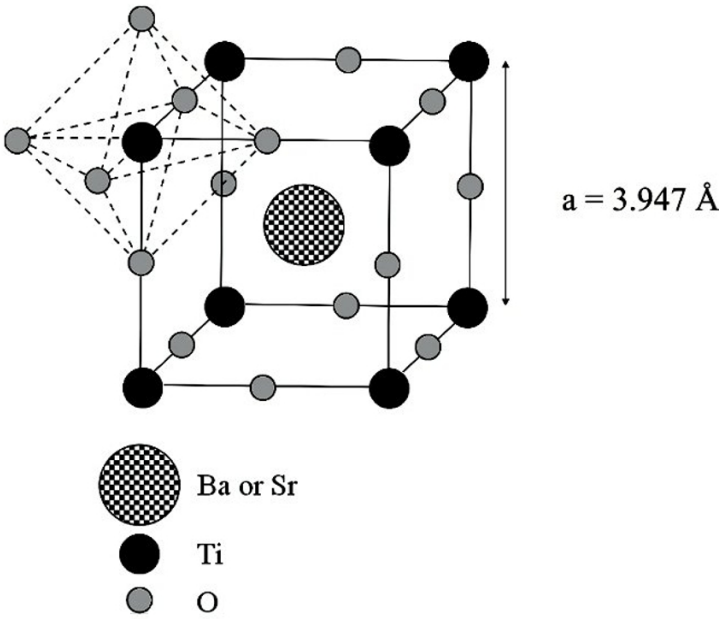

Figure 8.2. Crystal structure of Barium Strontium Titanate. Figure adapted from reference [6].

Barium-strontium-titanate (BSTO) is a widely used ferroelectric, having the formula $Ba_{1-x}Sr_xTiO_3$. BSTO is often referred to as a "tunable" ferroelectric because the permittivity changes with applied electric field. The compound with x=0.5 is in a paraelectric state, with Curie temperature below room temperature. The Curie temperature can be adjusted by changing the value of x ($BaTiO_3$ is ferroelectric and $SrTiO_3$ is paraelectric at room temperature). The spontaneous polarization comes from the relative displacement of Ba(Sr) and Ti atoms to the O atoms. The crystal structure of BSTO is shown in figure 8.2, with lattice parameter around 4Å. At the Curie point, the lattice undergoes a phase transition from cubic (paraelectric) to tetragonal (ferroelectric). BSTO is a particularly attractive material for microwave applications because it posseses a large permittivity ($\epsilon \approx 10,000$ at 0 V), high tunability, fast response to electric fields, high breakdown fields, low dielectric leakage currents, and it is relatively easy to fabricate [6, 88].

Other groups have brought together these two technologically important materials through doping BaM with BSTO [32] and a former graduate who graduated from our lab with a Ph.D. has grown 50% BSTO/50% BaM composite thin films as well as multilayers

fabricated by pulsed laser deposition (PLD) [26]. My research was the primary contribution in our group's effort which led to the optimized growth of sputtered BSTO/BaM multilayer thin films and studying their magnetic properties.

8.2 Multilayer Thin Film Growth

8.2.1 Films Grown at Oak Ridge National Laboratory

Pure BSTO and BaM films as well as multilayer films were grown on two types of substrates: Polished alumina (Al_2O_3) and thermally oxidized (001) silicon. Deposition was done using a non-commercial magnetron sputtering vacuum chamber equipped with two guns holding the BSTO and BaM targets and attached to RF power supplies. The BSTO and BaM targets were 2-inch ceramic sputter targets with copper back plates from SCI Engineered Materials. The two targets were set up vertically and a movable substrate holder could be positioned over either target. In addition, a quartz crystal oscillator could be placed over either of the targets to measure deposition rates. The presence of two guns allowed the multilayer structure to be grown *in situ* by simply rotating the substrate holder to be in position above the desired target. The original substrate holder was modified by the author to include a heater and thermocouple. The substrates were heated during deposition to around 300° to promote film adhesion. For all multilayer films, BSTO was used as the bottom layer due to its superior adhesion to silicon over BaM. The multilayer films grown at Oak Ridge National Laboratory were four layers: Substrate/BSTO/BaM/BSTO/BaM. The overall film thickness was optimized to be around 1.5 μm. Deposition conditions are presented in table 8.1.

All films were taken back to the University of South Florida for post-annealing as the substrate heater was sufficient for promoting adhesion, but the as-grown films were still amorphous. Post annealing was done in a tube furnace at 1000°C in flowing O_2 for 10 hours. X-ray diffraction (XRD) scans were performed at the University of South Florida using a Philips PW2-4-Pro diffractometer available through the College of Engineering. XRD measurements revealed the presence of several BaM and BSTO peaks consistent with the

Base pressure = 6.8×10^{-6} Torr Deposition Temperature 350°C	Layer 1 (BSTO)	Layer 2 (BaM)	Layer 3 (BSTO)	Layer 4 (BaM)
Argon pressure (mTorr)	20	20	20	20
Argon flow (sccm)	57.0	56.7	56.6	56.4
Power (W)	71	70	71	70
DC Bias (V)	146	242	148	245
Deposition rate (Å/min)	60.0	39.2	71.6	46.4

Table 8.1. RF Magnetron sputtering parameters for BSTO/BaM multilayers grown at Oak Ridge National Laboratory.

polycrystalline phases of each. The films grown on Si/SiO_2 showed impurity peaks which matched well the diffraction pattern of $Sr_3Si_3O_9$. Since BSTO was the bottom layer, we believe that the BSTO film reacted with the Si/SiO_2 substrate creating an impurity layer. Figure 8.3 is a representative X-ray diffraction scan of the multilayers on Al_2O_3.

8.2.2 Films Grown at the University of Central Florida

Multilayer thin films as well as pure BSTO and BaM films were grown together with Dr. Srinath Sanyadanam and Dr. Ranko Heindl using a commercial magnetron sputtering system built by AJA International, Inc. The targets used this time were 3-inch ceramic targets from STMC, Ohio. A new substrate holder had to be built for this system as well because the substrate-target distance was prohibitively large causing very low deposition rates. Even with the modified substrate holder, the deposition time was still quite long so the number of layers was limited to just three. A heater was not included in the modified substrate holder, which created more adhesion problems. It was found that the BaM could adhere properly at room temperature onto Al_2O_3 and allow for annealing. Thus the films grown at the University of Central Florida were all Al_2O_3/BaM/BSTO/BaM. The deposition details are presented in table 8.2. As-grown films were again amorphous and post annealing was done at the University of South Florida using the same conditions described above. Figure 8.4 is a representative XRD scan for the multilayer films grown at the University of Central Florida.

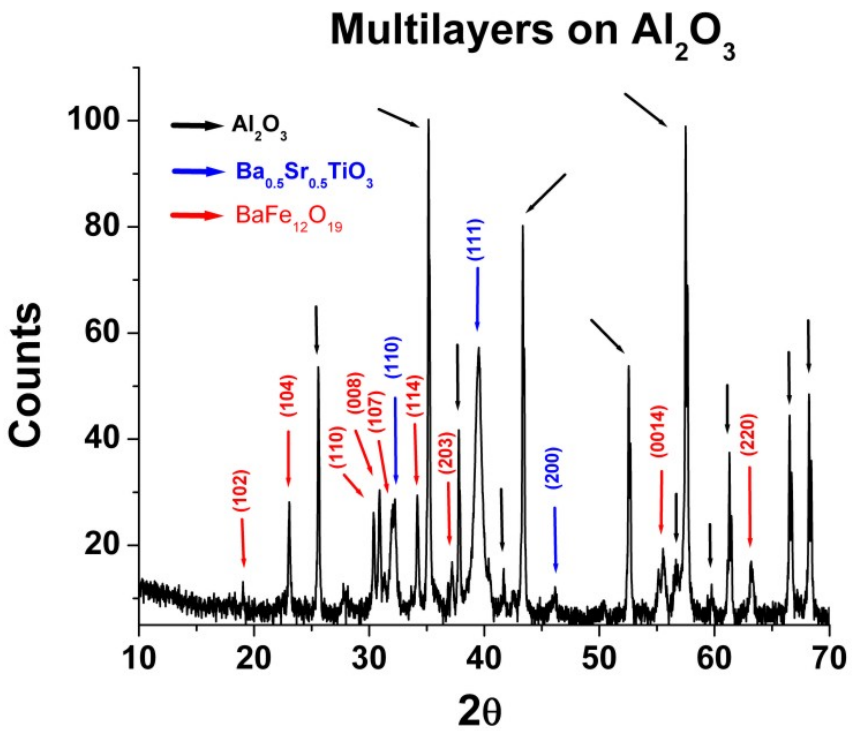

Figure 8.3. X-ray diffraction scan of BaM/BSTO multilayers grown on Al_2O_3 at Oak Ridge National Laboratory.

Base pressure = 7.8×10^{-6} Torr Deposition Temperature: Ambient	Layer 1 (BaM)	Layer 2 (BSTO)	Layer 3 (BaM)
Argon pressure (mTorr)	4	4	4
Argon flow (sccm)	20	20	20
Power (W)	70	70	70
DC Bias (V)	302	196	302
Deposition rate (Å/min)	38	57	38

Table 8.2. RF Magnetron sputtering parameters for BSTO/BaM multilayers grown by the author at the University of Central Florida.

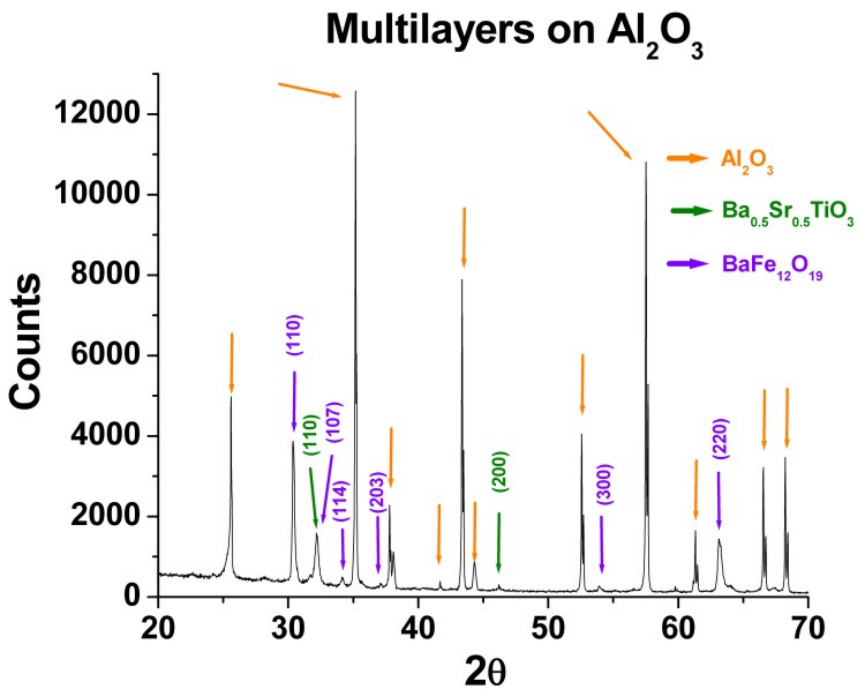

Figure 8.4. X-ray diffraction scan of BaM/BSTO multilayers grown on Al_2O_3 at the University of Central Florida

8.3 Multilayer Characterization

Figure 8.5 shows a cross-sectional scanning electron microscope (SEM) image of one of the multilayer thin films grown on Si at Oak Ridge National Laboratory. A multilayer structure with distinct interfaces between layers is evident even after annealing. The picture depicts alternate layers of 0.3 μm thick BaM and 0.2 μm thick BSTO. The bottom layer may consist of intermixing of Strontium with the Silicon substrate, which would account for the peaks corresponding to $Sr_3Si_3O_9$ in the XRD spectra. While there was some error in estimation of deposition rate leading to non-uniform thickness of individual layers, what it unmistakable is the presence of well-defined and distinctly visible layers from a coarse grain-structure point of view in the final-annealed film. This is promising in terms of realizing composite multilayers without significant degradation of materials properties at the interfaces.

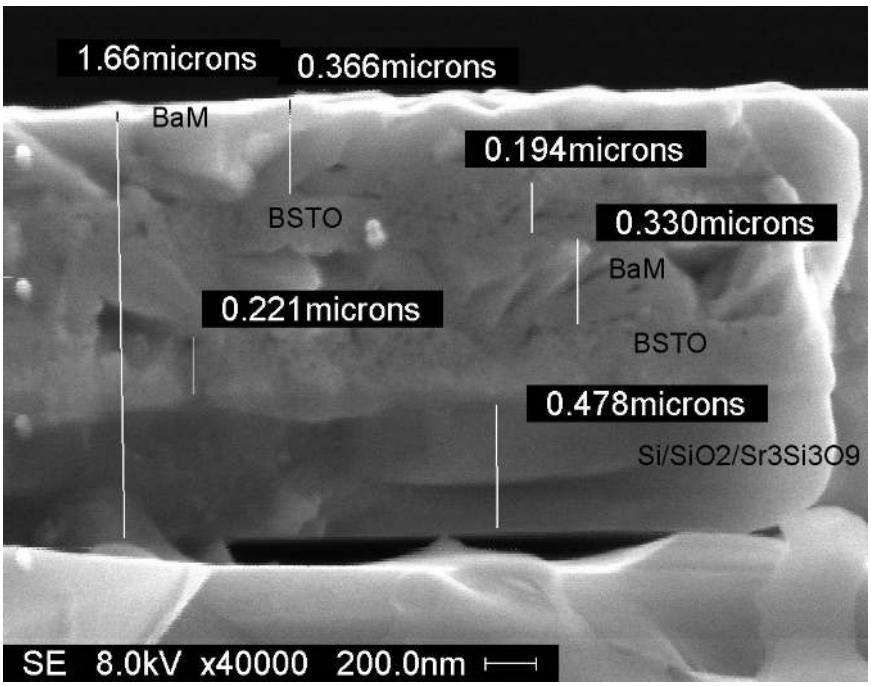

Figure 8.5. Cross-sectional image of a $Si/SiO_2/(BSTO/BaM)_2$ multilayer film after annealing.

Figure 8.6 shows an SEM image of the surface of the same sample used in figure 8.5. The elongated platelet-type grains which are typical of BaM are clearly visible with an average grain size of 1.2 μm x 0.3 μm. This high aspect ratio in the grains is what gives BaM its well-known shape anisotropy. The size and shape of the grains depend largely on the deposition and annealing conditions, which in turn affect the overall magnetic properties. This is desirable for microwave properties as the dielectric constant and permeability have been shown to increase with increase in the grain size [32].

8.4 Magnetic Properties of BaM and Multilayer Thin Films

From the growth conditions described in section 8.1, it is not very practical to make direct comparisons between the films grown at Oak Ridge National Laboratory and those grown at the University of Central Florida. Not only were the substrate temperatures different (350°C versus room temperature) but also the multilayer structure was different ($sub/(BSTO/BaM)_2$) versus sub/BaM/BSTO/BaM). Therefore, any comparison made be-

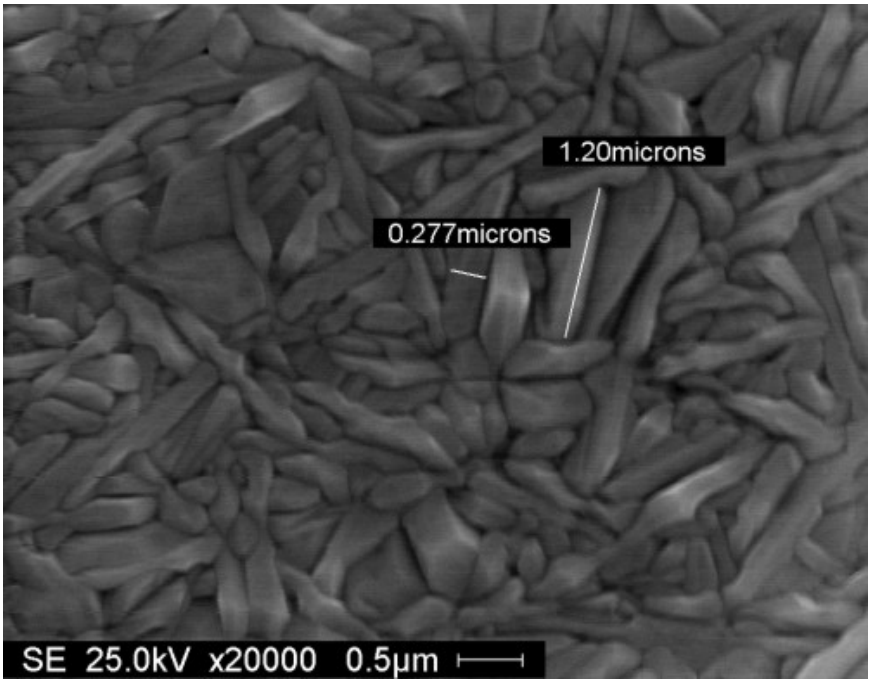

Figure 8.6. SEM image of the BaM surface of a multilayer film.

tween the two can only be done without decoupling the effects of substrate temperature, bottom layer and total number of layers. In this section, brief summaries of each set of films and the conclusions that can be drawn from them will be presented as well as a broad overall summary of all samples with only minimal discussion about the origin of the differing magnetic properties.

8.4.1 Magnetic Properties of Films Grown at the University of Central Florida

We first examined the magnetization versus field loops of a film of just BaM on Al_2O_3 at 10K and 300K (figure 8.7). In all of the M-H curves presented, a noticeable diamagnetic background can be seen at low temperatures which is manifest as a downward tilt of the loop. This is due to the magnetic response of the substrates, which are diamagnetic at low temperature and contribute a slight paramagnetic response at higher temperatures, manifest as a slight upward tilt. The room temperature H_C value of the BaM (1900 Oe) is

Sample Description	H_C (Oe) 10K	H_C (Oe) 300K
BaM/Al_2O_3	2100	1900
BaM/BSTO/BaM/Al_2O_3	1800	2100

Table 8.3. Coercivity values for multilayer films grown at The University of Central Florida.

in good agreement with reported values of BaM films [11, 74]. For the pure BaM film only, we were able to determine the saturation magnetization (M_S) from the magnetic moment with confidence since the entire film thickness is BaM and therefore the magnetic volume can be estimated. Using a Tencor Instruments profilometer, we measured film thickness of the BaM to be 0.45μm. After finding the sample area to be 0.324cm^2, and the total magnetic moment to be 6.13 x 10^{-3} emu at 10K and 1.75 x 10^{-3} emu at 300K we calculated the values of M_S to be 420 emu/cc at 10K and 120 emu/cc at 300K. These values again match well with magnetic properties reported in BaM thin films [11, 74]]. For the multilayer films, we did not calculate the M_S values as there was no way to accurately determine the total magnetic volume. However, for our purposes, it is coercivity and the shape of the M-H curves that we are most interested in as it is the best indicator of magnetic anisotropy in this system. For the pure BaM film, the coercivity increases with decrease in temperature (2100 Oe at 10K), which is the expected behavior in bulk magnetic materials.

Upon examining the 10K and 300K hysteresis loops of the multilayer films grown under the same conditions (figure 8.8) it is apparent the magnetic behavior is different. Rather than a decrease in coercivity with a increase in temperature like the pure BaM film, the multilayers exhibit an increase in coercivity with increase in temperature going from 1800 Oe at 10K to 2100 Oe at 300K . This trend is also seen in the films grown at Oak Ridge National Laboratory and will be discussed in a later section. The high and low temperature H_C values for both the BaM and the multilayer films are collected in table 8.3.

8.4.2 Magnetic Properties of Films Grown at Oak Ridge National Laboratory

Magnetization versus field (M-H) measurements were performed at 10K and 300K with magnetic field applied parallel (in-plane) and perpendicular (out-of-plane) to the surface of

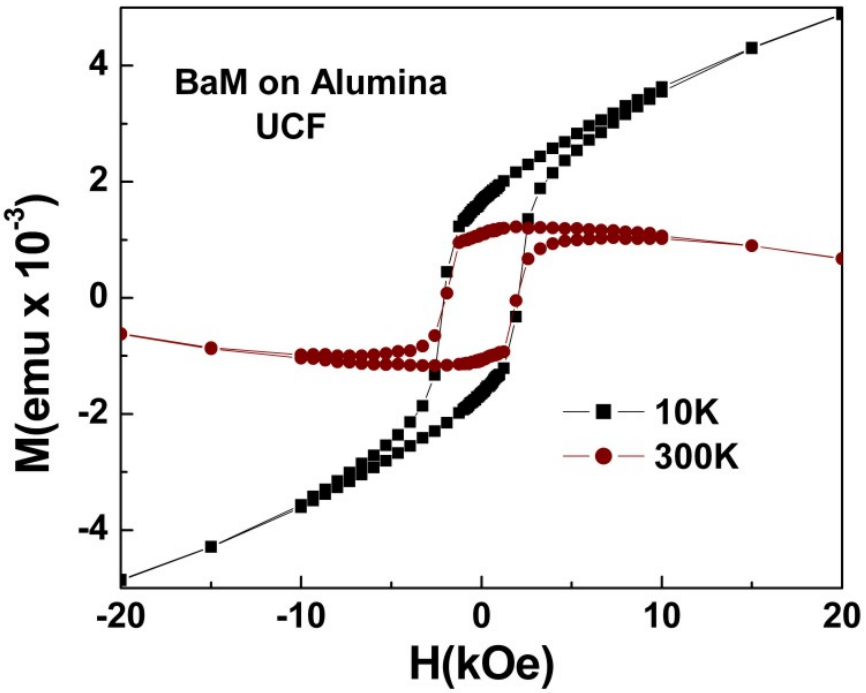

Figure 8.7. 10K and 300K hysteresis loops for BaM on Al_2O_3 grown at the University of Central Florida.

the film. In figures 8.9 and 8.10 the in-plane 10K and 300K hysteresis loops are presented for the multilayer films grown on Al_2O_3 (figure 8.9) and Si (figure 8.10. Once again it can be seen that the coercivity increases with increase in temperature (from 2600 Oe to 3900 Oe for the film on Al_2O_3, and from 1460 Oe to 2300 Oe for the film on Si). This is the same behavior that was observed for the multilayer films grown at the University of Central Florida and is opposite the traditional behavior seen for BaM alone, namely a decrease in coercivity with increase in temperature. This point will be further discussed in the next section. It is also apparent that for both temperatures, the H_C values for the films grown on Si are much lower than the H_C values for the films grown on Al_2O_3.

Figures 8.12 and 8.11 show the 10K in-plane and out-of-plane hysteresis loops for the multilayers grown on Al_2O_3 (figure 8.12) and Si (figure 8.11). For the multilayers grown on Si the perpendicular coercivity and the parallel coercivity at 10K are 1250 Oe and 1450 Oe and the squareness S (the ratio of the remanent magnetization to the saturation mag-

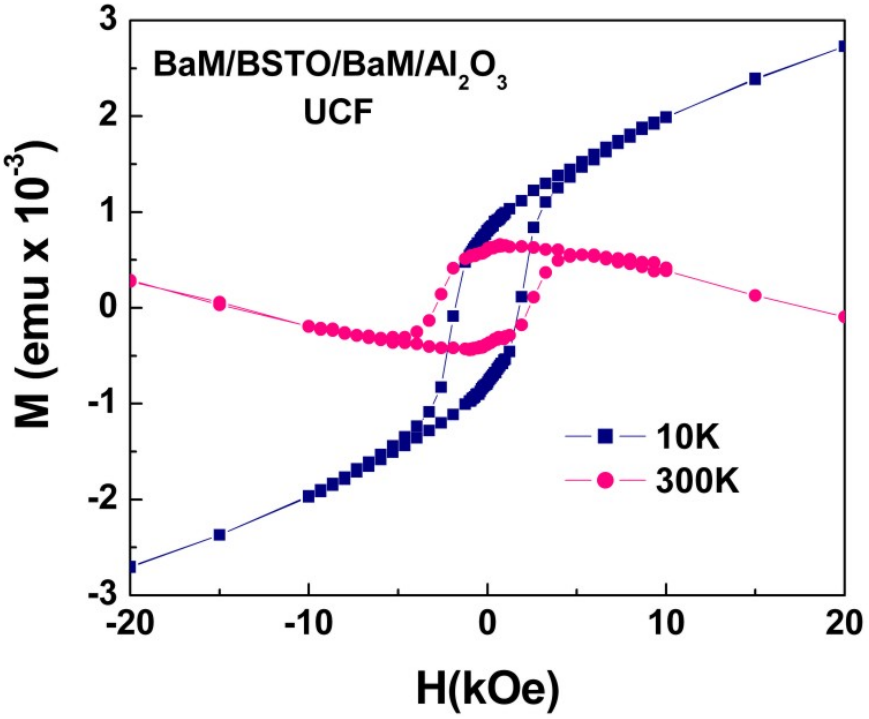

Figure 8.8. 10K and 300K hysteresis loops for multilayers on Al_2O_3 grown at the University of Central Florida.

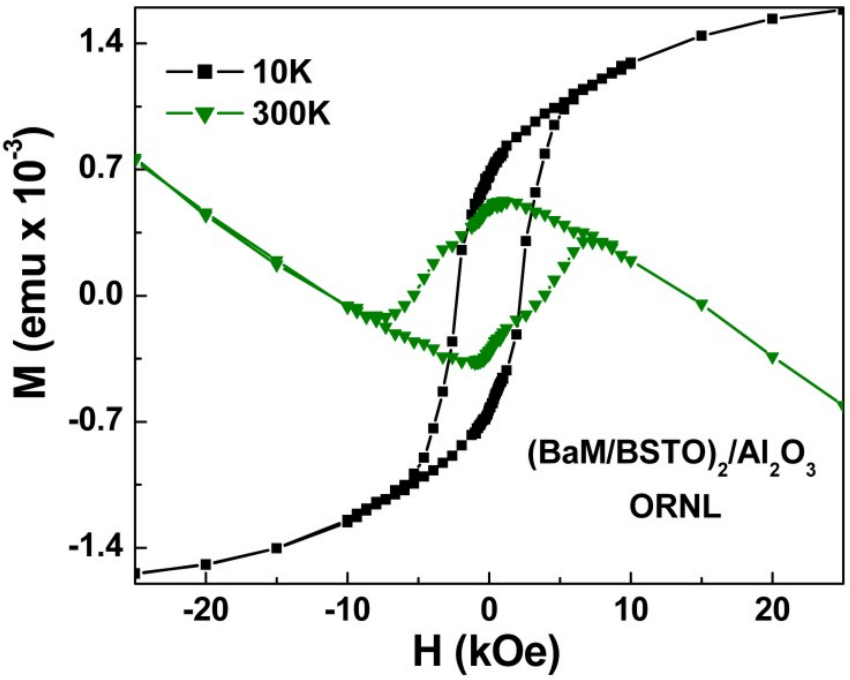

Figure 8.9. 10K and 300K hysteresis loops for multilayers on Al_2O_3 grown at Oak Ridge National Laboratory.

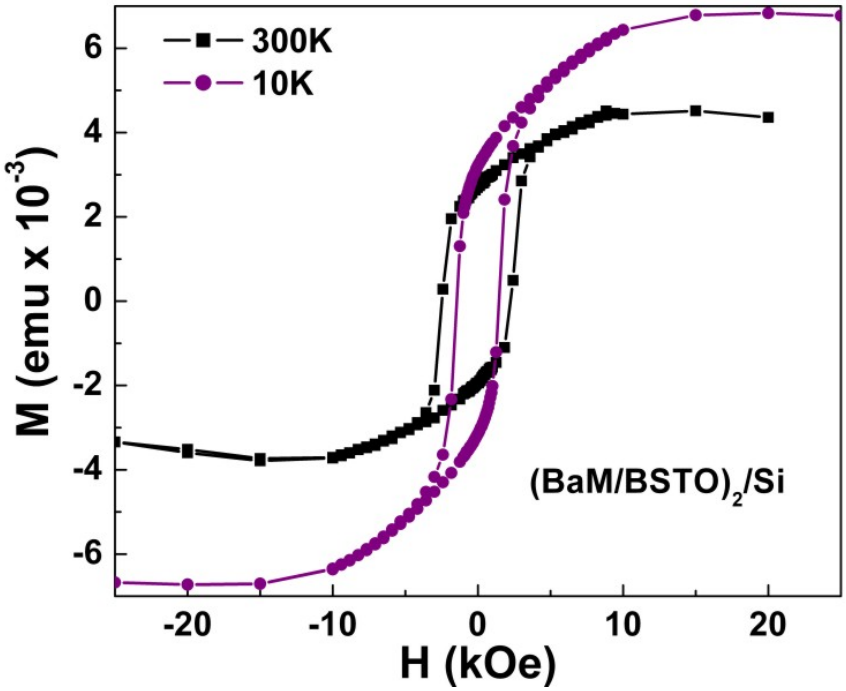

Figure 8.10. 10K and 300K hysteresis loops for multilayers on Si grown at Oak Ridge National Laboratory.

Sample Description	H_C (Oe) 10K in-plane	H_C (Oe) 10K out-of-plane	H_C (Oe) 300K in-plane	H_C (Oe) 300K out-of-plane
$(Bam/BSTO)_2/Al_2O_3$	2600	2600	3900	3900
$(BaM/BSTO)_2/Si$	1460	1250	2300	2200

Table 8.4. Coercivity values for multilayer films grown at Oak Ridge National Laboratory.

netization, M_R/M_S) of the perpendicular and parallel loops are 0.45 and 0.60 respectively. The difference in magnetization in two different directions of the multilayers plane indicates that there is a preferential orientation of magnetization along a favored direction, which is the easy axis of magnetization for the BaM grains. As can be seen in figure 8.6, the platelet-like grains in the BaM layer appear to have attained an in-plane texturing and the magnetic easy axis seems to be in the same direction.

In contrast, the multilayers grown on Al_2O_3 show no such deviation upon changing orientations of the magnetic field. The polycrystalline Al_2O_3 substrate does not allow grain orientation and the lack of texturing causes no change in coercivity with respect to applied field direction. The value of H_C 10K remains the same at 2600 Oe regardless of field orientation. In table 8.4 we present the in-plane and out-of-plane H_C values for multilayer films grown on each substrate at 10K and 300K. Note that the texturing exists to a lesser extent at room temperature for films grown on Si, and not at all for the films grown on Al_2O_3.

The room temperature results presented for the films grown at Oak Ridge National Laboratories on heated Si are consistent with those reported for pure BaM films deposited using pulsed Laser deposition heated *in situ* to 900°C on Si (001) substrates [45]. The in-plane and out-of-plane coercivities in our case is only slightly different from the reported values of Lu and Song [45]. While the different film growth techniques are expected to have some influence on the magnetic characteristics, substrate heating in their case was much higher and is likely the primary reason for them obtaining better texture. Also, while substrate material clearly has an effect on the texturing (an oriented substrate gives textured films, a polycrystalline substrate gives isotropic films), it is important to keep in

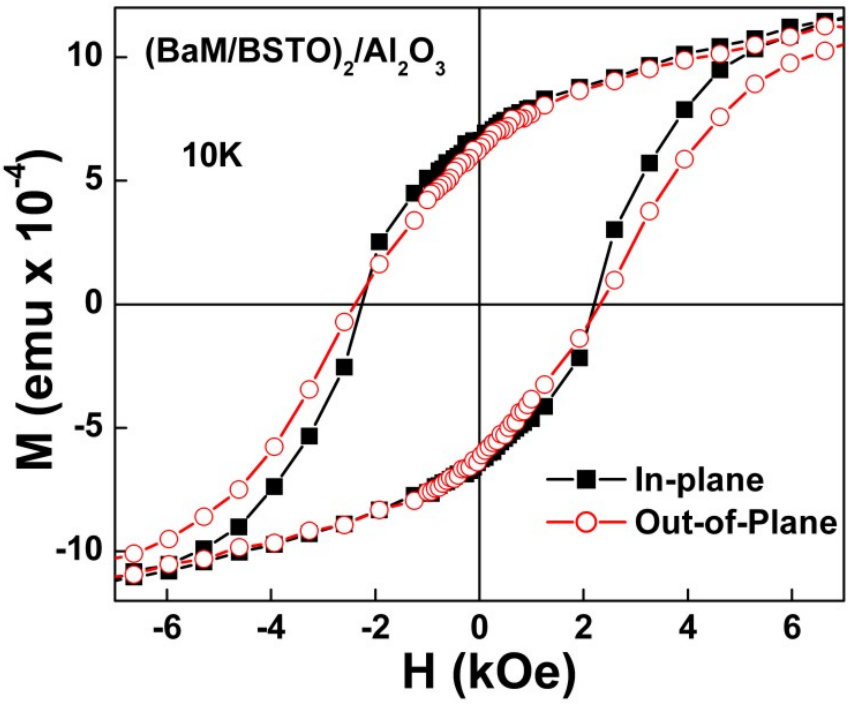

Figure 8.11. 10K hysteresis loops for multilayers on Si taken with H in-plane and out-of-plane.

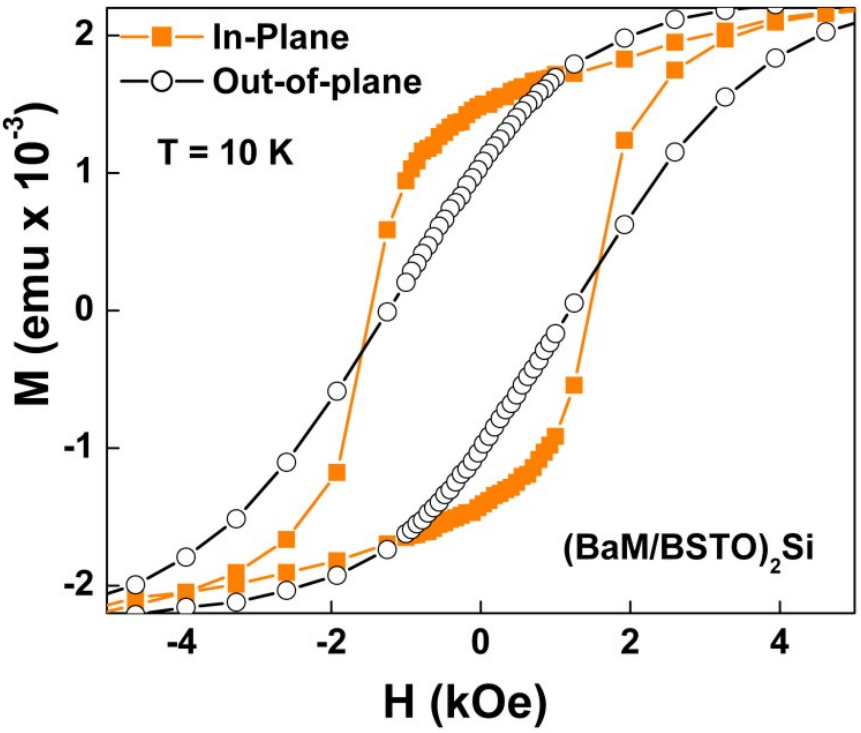

Figure 8.12. 10K hysteresis loops for multilayers on Al_2O_3 taken with H in-plane and out-of-plane.

mind that neither layer of BaM is in direct contact with the oriented Si. Thus the extent of the texturing that would usually be seen in BaM on Si (001) may be lost in this case due to the intermediate BSTO. Extensive studies of epitaxy and substrate influence in PLD-grown BaM/BSTO films have been done by a former graduate student (Ranko Heindl) and reported in his Ph.D. thesis [28].

8.5 Correlating the Coercivity with Microstructure in BaM and BaM/BSTO Multilayer Films

The most noticeable trend in the above data is that while the coercivity of the BaM decreases with increase in temperature (consistent with most other bulk magnetic materials), the multilayers behave in the opposite way with increasing coercivity as temperature increases. We believe this can be understood in terms of the competition between shape and magnetocrystalline anisotropies in BaM. The theoretical coercivity of a random array of BaM particles is given by Kubo *et al.* [39]

$$H_C = 0.48(2K_{\text{eff}}/M_S - NM_S) \tag{8.1}$$

where N is the demagnetizing factor. The first term ($2K_{\text{eff}}/M_S$) is the magnetocrystalline anisotropy and the second term (NM_S) is the shape anisotropy. As M_S decreases with increase in temperature, the first term dominates and H_C will increase with temperature. It is possible that the presence of the BSTO layers affect the grain growth of the BaM. It is known that the coercivity of BaM is inversely proportional to the grain size, with larger grains yielding a smaller coercivity [33]. In this case, if the grain growth is inhibited, the coercivity will increase, resulting in a smaller aspect ratio and thus a smaller shape anisotropy (NM_S). Indeed, all the coercivity values presented above for the multilayers show an increase in coercivity over the pure BaM.

In comparing the two sets of films, we can deduce that (1) the functional dependence of coercivity on temperature is altered by the presence of BSTO and that (2) heating the

substrate while depositing the multilayers enhances this effect since all the films grown on heated substrates display larger H_C values than all of those grown at room temperature. However it is important to remember that the multilayers grown at room temperature also had less BSTO present than the ones grown on heated substrates. Therefore, as mentioned in an earlier section, a more systematic study is needed to decouple these two effects, namely the number of BSTO layers and the substrate heating.

For many technological applications, the increase in H_C with increase in temperature (resulting in higher room temperature H_C), along with the overall increase in coercivity with BSTO present leads to greater functionality of the BaM in the multilayers than in BaM alone. While the ferroelectric properties of BSTO in multilayer form with BaM have not been explored extensively, Dr. Ranko Heindl, a former student showed in his doctoral thesis that dual tunability of the permittivity ϵ in BSTO and permeability μ in BaM for microwave applications is achievable in BSTO/BaM bilayer thin films [28].

8.6 Conclusion

We have grown BaM thin films and BSTO/BaM multilayer thin films and examined the structural as well as magnetic properties of both. The BaM films grown at room temperature on Al_2O_3 exhibited behavior consistent with other reports of BaM films grown under similar conditions. The multilayers, grown both at room temperature and 350^circC on Al_2O_3 and on heated (001) Si showed different behavior with much larger H_C values which increase with increasing temperature, contrary to what is expected in magnetic materials. The films grown on Si also show texturing with different H_C and squareness ratio depending upon the direction of applied magnetic field. We believe that all the described behavior can be attributed to the dependence of grain size and shape on the growth conditions, including the presence of BSTO in the multilayers. The trend can be explained by the temperature dependence on the competing magnetocrystalline and shape anisotropies.

CHAPTER 9

CONCLUSION AND FUTURE WORK

This work presented the magnetic properties of several multifunctional systems including core-shell Au-Fe_3O_4 nanoparticles, dumbbell- and flower-shaped Au-Fe_3O_4 nanoparticles, CrO_2 and CrO_2/Cr_2O_3 thin films and BaM/BSTO multilayer thin films. In these systems we were able to show how the magnetic anisotropy was influenced by key parameters from altering particle size, shape, surfaces and interfaces in Au-Fe_3O_4 particles to the effects of interfaces between substrates and functional layers in multilayer thin films. In several of these instances, we used transverse susceptibility in new ways to gain deeper insight into the physics of these complex systems.

9.1 Magnetic Nanoparticles for Biomedical Applications

For Fe_3O_4 and Au-Fe_3O_4 nanoparticles synthesized specifically for biomedical applications, we conclusively demonstrated how coating Fe_3O_4 particles with Au decreases interparticle interactions while increasing the functionality of the particles. The particular size chosen for the synthesis of the particles coincides with the size range that can be successfully taken up by human embryonic kidney cells. This particle diameter, about 70 nm, also proved to be advantageous for hyperthermia applications as we demonstrated that the particles were superparamagnetic in DC magnetic fields and ferromagnetic at the 12 MHz used in transverse susceptibility measurements. This indicates that hysteretic losses could also contribute to the heating ability of these particles. We were also able to show how the transverse susceptibility measurement could be used as a sensor for cells that have taken up magnetic nanoparticles. Due to its high sensitivity and the low external DC fields required, we described why this method could find use in cancer diagnostics.

Remaining questions with regards to this research are:

- What other core-shell configurations can be made which may display even better magnetic properties while maintaining biocompatibility?
- Since different bodily systems require different size nanoparticles to achieve uptake, can we tune the anisotropy in smaller/larger particles of different materials to display the same balance of DC superparamagnetism/AC ferromagnetism?
- Can a smaller, more compact biosensor be built based on the concept of transverse susceptibility and the results we obtained?

9.2 Au-Fe_3O_4 Composite Nanostructures

We also examined the magnetic properties of two new configurations of Au-Fe_3O_4. The dumbbell-shaped Au-Fe_3O_4 particles, which showed behavior similar to Fe_3O_4 and even core-shell Au-Fe_3O_4 nanoparticles, is an important system to explore for biomedical applications as two separate surfaces are available for functionalization. The flower-shaped nanoparticles proved to be a fascinating system from a fundamental physics point of view due to the combination of competing interactions giving rise to exchange bias and training effects in the low temperature regime, while maintaining an anomalously high anisotropy in the intermediate regime before blocking. An important feature of both of these systems is the fact that both the Au and the Fe_3O_4 sizes can be controlled for possible use in a broad range of applications.

There are numerous directions this research can take and several questions that remain unresolved. Most notably:

- Can we optimize the size combinations of Au and Fe_3O_4 to find which combination performs best for functionalization, cellular uptake, and magnetic manipulation while inside the cells?
- What is the nature of the low temperature negative magnetization?

- Can we change the sizes of the Au in the flower particles to determine the dependence of the interaction strength between Fe_3O_4 particles on the intra-particle distance?

- Similarly, can we change the size of the Fe_3O_4 as well as the number nucleated onto the Au? This could help form a better picture of the spin frustration likely involved between adjacent Fe_3O_4 particles.

9.3 CrO_2 Epitaxial Thin Films and Bilayer CrO_2/Cr_2O_3 Thin Films

The thickness and temperature dependence of CrO_2 epitaxial thin was explored using transverse susceptibility. We were able to confirm and track the easy axis switching due to the inhomogeneous strain at 200 nm. We have also presented strong case for exchange coupling of CrO_2/Cr_2O_3 bilayers through a uniaxial anisotropy rather than the unidirectional anisotropy normally associated with exchange coupled systems. This uniaxial anisotropy is manifest as a modest increase in H_C and a substantial increase in H_K measured with transverse susceptibility. We were successfully able to rule out a simple ferromagnetic thickness dependence by measuring several different thicknesses of CrO_2 films. We suggested that the lack of unidirectional anisotropy in the bilayers is likely due to perpendicular spin-flop coupling between the Cr_2O_3 and the CrO_2. Some questions that would be interesting to address for these systems are:

- All the films had the same total thickness which meant each component was varying. Can we form a better picture of the dependence of the anomalous anisotropy on thickness by varying the thicknesses of the ferromagnet and antiferromagnet independently?

- Can any of the anisotropic behavior of the CrO_2/Cr_2O_3 bilayers be explained by a magnetoelectric coupling of the CrO_2 to the Cr_2O_3?

- Similarly, could an experiment be done in the same vein as the one used by Borisov *et al.* to see if applied electric field changes the nature of the exchange coupling?

- A probe that measures impedance in a magnetic field currently being built for integration into the PPMS could help answer many of these questions.

9.4 BaM Thin Films and BaM/BSTO Multilayer Thin Films

BaM thin films and BSTO/BaM multilayer thin films have been grown and the structural as well as magnetic properties have been examined. BaM films exhibited behavior consistent with other reports of BaM films grown under similar conditions. The multilayers showed different behavior with H_C values which increase with increasing temperature, contrary to what is expected in magnetic materials. We believe that this behavior can be attributed to the dependence of grain size and shape on the growth conditions, including the presence of BSTO in the multilayers. The trend can be explained by the temperature dependence on the competing magnetocrystalline and shape anisotropies. Many of the questions that were posed at the time this research was completed have been answered as a result of the research performed by Dr. Ranko Heindl.

Manipulation of the magnetic anisotropy in nanoparticles and thin films will continue to be an important aspect in future technological applications. This work has shown that surface and interface magnetism can dramatically alter the overall magnetic response of a system in unexpected ways and technologically important ways.

REFERENCES

[1] A. Aharoni, *Introduction to the Theory of Ferromagnetism*, Oxford University Press, 1996.

[2] A. Aharoni, E. H. Frei, S. Shtrikman, and D. Treves, *The reversible susceptibility tensor of the Stoner-Wohlfarth model*, Bull. Res. Counc. of Israel A: Math., Phys. & Chem. **6A** (1957), 215–238.

[3] M. Albrecht, G. Hu., I. L. Guhr, T. C. Ulbrich, J. Boneberg, P. Leiderer, and G. Schatz, *Magnetic multilayers on nanospheres*, Nature Leters **4** (2005), 203–206.

[4] C. R. Alves, R. Aquino, J. Depeyrot, T. A. P. Cotta, M. H. Sousa, F. A. Tourinho, H. R. Rechenberg, and G. F. Goya, *Surface spin freezing of ferrite nanoparticles evidenced by magnetization measuremets*, J. Appl. Phys. **99** (2006), 08M905–1–08M905–3.

[5] I. Baker, Q. Zeng, W. Li, and C. Sullivan, *Heat deposition in iron oxide and iron nanoparticles for localized hyperthermia*, J. Appl. Phys. **99** (2006), 08H106–1–3.

[6] B. A. Baumert, L. H. Chang, A. T. Matsuda, T. L. Tsai, C. J. Tracy, R. B. Gregory, P. L. Fejes, N. G. Cave, W. Chen, D. J. Taylor, T. Otsuki, E. Fujii, S. Hayashi, and K. Suu, *Characterization of sputtered barium strontium titanate and strontium titanate-thin films*, J. Appl. Phys. **82** (1997), 2558–2566.

[7] C. C. Berry and A. S. G. Curtis, *Functionalisation of magnetic nanoparticles for applications in biomedicine*, J. Phys.: Appl. Phys. **36** (2003), R198–R206.

[8] F. Bødker, S. Mørup, and S. Linderoth, *Surface effects in metallic iron nanoparticles*, Phys. Rev. Lett. **72** (1994), 282–285.

[9] P. Borisov, A. Hochstrat, X. Chen, W. Kleemann, and C. Binek, *Magnetoelectric switching of exchange bias*, Phys. Rev. Lett. **94** (2005), 117203–1–117203–4.

[10] O. Cador, F. Grasset, H. Haneda, and J. Estourneau, *Memory effect and super-spin-glass ordering in an aggregated nanoparticle sample*, J. Magn. Magn. Mater. **268** (2004), 232–236.

[11] S. Capraro, J. P. Chatelon, H. Joisten, M. Le Berre, B. Bayard, D. Barbier, and J. J. Rousseau, *Magnetic properties of sputtered barium ferrite thick films*, J. Appl. Phys. **93** (2003), 9898–9901.

[12] E. E. Carpenter, A. Kumbhar, J. A. Wiemann, H. Srikanth, J. Wiggins, W. Zhou, and C. J. O'Connor, *Synthesis and magnetic properties of gold-iron-gold nanocomposites*, Mat. Sci. & Eng. A **A286** (2000), 81–86.

[13] R. W. Chantrell, A. Hoare, D. Melville, H. J. Lutke-Stetzkamp, and S. Methfessel, *Transverse susceptibility of a fine particle system*, IEEE Trans. Mag. **25** (1989), 4216–4218.

[14] R. Cheng, C. N. Borca, N. Pilet, B. Xu, L. Yuan, B. Doudi, S. H. Liou, and P. A. Dowben, *Oxidation of metals at the chromium oxide interface*, Appl. Phys. Lett. **81** (2002), 2109–2111.

[15] D. Cimpoesu, A. Stancu, I. Dumitru, and L. Spinu, *Micromagnetic simulation of the imaginary part of the transverse susceptibility*, IEEE Trans. Mag. **41** (2005), 3121–3123.

[16] D. Cimpoesu, A. Stancu, and L. Spinu, *Micromagnetic simulation of the complex transverse susceptibility in nanostructured particulate systems*, J. Appl. Phys. **99** (2006), 08G315–1–08G315–3.

[17] A. S. Eggeman, S. A. Majetich, D. Farrell, and Q. A. Pankhurst, *Size and concentration effects on high frequency hysteresis of iron oxide nanoparticles*, IEEE Trans. Mag. **43** (2007), 2451–2453.

[18] N. A. Frey, *Microstructure and Magnetism in Ferrite-Ferroelectric Multilayer Films*, Master's thesis, University of South Florida, 2004.

[19] N. A. Frey, R. Heindl, S. Srinath, H. Srikanth, and N. J. Dudney, *Microstructure and magnetism in barium strontium titanate (BSTO)- barium hexaferrite (BaM) multilayers*, Mat. Res. Bull. **40** (2005), 1286–1293.

[20] P. Gangopadhyay, S. Gallet, E. Franz, A. Persppms, and T. Verbiest, *Novel superparamagnetic core(shell) nanoparticles for magnetic targeted drug delivery and hyperthermia treatment*, IEEE Trans. Mag. **41** (2005), 4194–4196.

[21] J. Gass, N. A. Frey, M. B. Morales, M. J. Miner, S. Srinath, and H. Srikanth, *Magnetic anisotropy and magnetocaloric efect (MCE) in $NiFe_2O_4$ Nanoparticles*, Mater. Res. Soc. Symp. Proc. **962** (2007), 0962–P05–03–1–0962–P05–03–6.

[22] G. F. Goya, T. S. Berquó, F. C. Fonseca, and M. P. Morales, *Static and dynamic magnetic properties of spherical, magnetite nanoparticles*, J. Appl. Phys. **94** (2003), 3520–3528.

[23] M. Grimsditch, A. Hoffmann, P. Vavassori, H. Shi, and D. Lederman, *Exchange-induced anisotropies at ferromagnetic-antiferromagnetic interfaces above and below the Néel temperature*, Phys. Rev. Lett. **90** (2003), 257201–1–257201–4.

[24] A. K. Gupta and M. Gupta, *Synthesis and surface engineering of iron oxide nanoparticles for biomedical applications*, Biomaterials **26** (2005), 3995–4021.

[25] A. K. Gupta and S. Wells, *Surface-modified superparamagnetic nanoparticles for drug-delivery: preparation, characterization, and cytotoxicity studies*, IEEE Trans. Nanobioscience **3** (2004), 66–73.

[26] R. Hajndl, J. Sanders, H. Srikanth, and N. J. Dudney, *Growth and characterization of BSTO/hexaferrite composite thin films*, J. Appl. Phys. **93** (2003), 7999–8001.

[27] V. G. Harris, Z. Chen, Y. Chen, S. Yoon, T. Sakai, A. Gieler, A. Yang, Y. He, K. S. Ziemer, N. X. Sun, and C. Vittoria, *Ba-hexaferrite films for next generation microwave devices*, J. Appl. Phys. **99** (2006), 08M911–1–08M911–5.

[28] R. Heindl, *Ferrite-Ferroelectric Thin Films With Tunable Electrical and Magnetic Properties*, Ph.D. thesis, University of South Florida, 2006.

[29] R. Heindl, H. Srikanth, S. Witanachchi, P. Mukherjee, A. Heim, G. Matthews, S. Balachandran, S. Natarajan, and T. Weller, *Multifunctional ferrimagnetic-ferroelectric thin films for microwave applications*, Appl. Phys. Lett. **90** (2007), 252507–1–252507–3.

[30] N. A. Hill, *Density functional studies of multiferroic magnetoelectrics*, Annu. Rev. Mater. Res. **32** (2002), 1–37.

[31] A. Hoare, R. W. Chantrell, W. Schmitt, and A. Eiling, *The reversible transverse susceptibility of particulate recording media*, J. Phys. D **26** (1993), 461–468.

[32] P. Huang, L. J. Deng, J. X. Xie, D. F. Liang, and L. Chen, *Effect of BST additive on the complex permeability and permittivity of Z-type hexaferrite in the range of 1MHz-1GHz*, J. Magn. Magn. Mater. **271** (2004), 97–102.

[33] T. L. Hylton, M. A. Parker, K. R. Coffey, and J. K. Howard, *Properties of epitaxial Ba-hexaferrite thin films on A-, R-, and C-plane oriented sapphire substrates*, J. Appl. Phys. **73** (1993), 6257–6259.

[34] K. Jonason, E. Vincent, J. Hammann, J. P. Bouchard, and P. Nordblad, *Memory and chaos effects in spin glasses*, Phys. Rev. Lett. **81** (1998), 3243–3246.

[35] A. Jordan, P. Wust, R. Scholz, B. Tesche, H. Fahling, T. Mitrovics, T. Vogl, J. Cervos-Navarro, and R. Felix, *Cellular uptake of magnetic fluid particles and their effects on human adenocarcinoma cells exposed to AC magnetic field in vitro*, Int. J. Hyperthermia **12** (1996), 705–722.

[36] C. Papusoi Jr., *The complex transverse susceptibility*, Phys. Lett. A **265** (2000), 391–402.

[37] H. Kachkachi and M. Dimian, *Hysteretic properties of a mganetic particle with strong surface anisotropy*, Phys. Rev. B **66** (2002), 174419–1–174419–11.

[38] R. H. Kodam, A. E. Berkowitz, E. J. McNiff Jr., and S. Foner, *Surface spin disorder in $NiFe_2O_4$ nanoparticles*, Phys. Rev. Lett. **77** (1996), 394–397.

[39] O. Kubo, T. Ido, and H. Yokoyama, *Properties of Ba-ferrite particles for perpendicular magnetic recording media*, IEEE Trans. Mag. **18** (1982), 1122–1124.

[40] A. Kumar, S. Mohapatra, V. Fal-Miyar, A. Cerdeira, J. A. García, J. Gass H. Srikanth, and G. V. Kurlyandskaya, *Magnetoimpedance biosensor for Fe_3O_4 nanoparticle intracellular uptake evaluation*, Appl. Phys. Lett. **91** (2007), 143902–1–143902–3.

[41] C. Leighton, M. R. Fitzsimmons, A. Hoffmann, J. Dura, C. F. Majkrzak, M. S. Kund, and I. K. Schuller, *Thickness-dependent coercive mechanisms in exchange-biased bilayers*, Phys. Rev. B **65** (2002), 064403–1–064403–6.

[42] C. Leighton, H. Suhl, M. J. Pechan, R. Compton, J. Nogués, and I. K. Schuller, *Coercivity enhancement above the Néel temperature of an antiferromagneti/ferromagnet bilayer*, J. Appl. Phys. **92** (2002), 1483–1488.

[43] X. W. Li, A. Gupta, T. R. McGuire, and P. R. Duncombe, *Magnetoresistence and Hall effect of chromium dioxide epitaxial thin films*, J. Appl. Phys. **85** (1999), 5585–5587.

[44] Q. H. Lu, K. L. Yao, D. Xi, Z. L. Liu, X. P. Luo, and Q. Ning, *Synthesis and characterization of composite nanoparticles comprised of gold and magnetic core/cores*, J. Magn. Magn. Mater. **301** (2006), 44–49.

[45] Y. F. Lu and W. D. Song, *Properties of $BaFe_{12}O_{19}$ films prepared by laser deposition with in situ heating and post annealing*, Appl. Phys. Lett. **76** (2000), 490–492.

[46] Jennifer L. Lyon, David A. Fleming, Matthew B. Stone, Peter Schiffer, and Mary Elizabeth Williams, *Synthesis of Fe Oxide core/Au shell nanoparticles by iterative hydroxylamin seeding*, Nano Letters **4** (2004), 719–723.

[47] S. A. Majetich and M. Sachan, *Magnetostatic interactions in magnetic nanoparticle assemblies: energy, time and length scales*, J. Phys. D: Appl. Phys. **39** (2006), R407–R422.

[48] G. Malinowski, M. Albrecht, I. L. Guhr, J. M. D. Coey, and S. van Dijken, *Size-dependent scaling of perpendicular exchange bias in magnetic nanostructures*, Phys. Rev. B **75** (2007), 012413–1–01241304.

[49] M. Mandal, S. Kundu, S. K. Ghosh, S. Panigrahi, T. K. Sau, S. M. Yusuf, and T. Pal, *Magnetite nanoparticles with tunable gold or silver shell*, J. Colloid and Interface Sci. **286** (2005), 187–194.

[50] B. Martinez, X. Obradors, Ll. Balcells, A. Rouanet, and C. Monty, *Low temperature surface spin glass transition in γ-Fe_2O_3 nanoparticles*, Phys. Rev. Lett. **80** (1998), 181–184.

[51] R. Matarranz, M. C. Contreras, G. Pan, B. Presa, J. A. Corrales, and J. F. Calleja, *Transverse susceptibility of nanoparticle systems: the effect of interaction, dispersion, and texture*, J. Appl. Phys. **99** (2006), 08Q504–1–08Q504–3.

[52] R. A. McCurrie, *Ferromagnetic Materials: Structure and Properties*, Academic Press, 1994.

[53] W. H. Meiklejohn and C. P. Bean, *New magnetic anisotropy*, Phys. Rev. **102** (1956), 1413–1414.

[54] J. Mejía-López, P. Soto, and D. Altbir, *Asymmetric reversal of the hysteresis loop in exchange-biased nanodots*, Phys. Rev. B **71** (2005), 104422–1–104422–4.

[55] G. Miao, G. Xiao, and A. Gupta, *Variations in the magnetic anisotropy properties of epitaxial CrO_2 films as a function of thickness*, Phys. Rev. B **71** (2005), 094418–1–094418–7.

[56] C. A. Mirkin, R. L. Letsinger, R. C. Mucic, and J. J. Storhoff, *A DNA-based method for rationally assembling nanoparticles into macroscopic materials*, Nature **382** (1996), 607–609.

[57] M. Muto, Y. Tanabe, T. Iizuka-Sakano, and E. Hanamura, *Magnetoelectric and second-harmonic spectra in antiferromagnetic Cr_2O_3*, Phys. Rev. B **57** (1998), 9586–9607.

[58] T. Neuberger, B. Schöpf, H. Hofmann, M. Hofmann, and B. von Rechenberg, *Superparamagnetic nanoparticles for biomedical applications: Possibilities and limitations of a new drug delivery system*, J. Magn. Magn. Mater. **293** (2005), 483–496.

[59] J. Nogués and I. K. Schuller, *Exchange Bias*, J. Magn. Magn. Mater. **192** (1999), 203–232.

[60] J. Nogués, J. Sort, V. Langlais, V. Skumryev, S. Suri nach, J. S. Mu noz, and M. D. Baró, *Exchange bias in nanostructures*, Phys. Rep. **422** (2005), 65–117.

[61] K. Okawa, M Sekine, M. Maeda, M. Tada, M. Abe, N. Matsushita, K. Nishio, and H. Handa, *Heating ability of magnetite nanobeads with various sizes for magnetic hyperthermia at 120 kHz, a noninvasive frequency*, J. Appl. Phys. **99** (2006), 08H102–1–3.

[62] Q. A. Pankhurst, J. Connolly, S. K. Jones, and J. Dobson, *Applications of magnetic nanoparticles in biomedicine*, J. Phys.: Appl. Phys. **36** (2003), R167–R181.

[63] L. Pareti and G. Turilli, *Detection of singularities in the reversible transverse susceptibility of an uniaxial ferromagnet*, J. Appl. Phys. **61** (1987), 5098–5101.

[64] D. L. Peng, K. Sumiyama, T. Hihara, S. Yamamuro, and T. J. Konno, *Magnetic properties of monodispersed Co/CoO clusters* , Phys. Rev. B **61** (2000), 3103–3109.

[65] J. P. Pierce, M. A. Torija, Z. Gai, J. Shi, T. C. Shulthess, G. A. Farnan J. F. Wendelken, E. W. Plummer, and J. Shen, *Ferromagnetix stability in Fe nanodot assemblies on Cu(111) induced by indirect coupling through the substrate*, Phys. Rev. Lett. **92** (2004), 237201–1–237201–4.

[66] P. Poddar, H. Srikanth, S. A. Morrison, and E. E. Carpenter, *Inter-particle interactions and magnetism in manganese-zinc ferrit nanoparticles*, J. Magn. Magn. Mater. **288** (2005), 443–451.

[67] P. Poddar, J. L. Wilson, H. Srikanth, D. F. Farrell, and S. A. Majetich, *In-plane and out-of-plane transverse susceptibility in close-packed arrays of monodisperse Fe nanoparticles*, Phys. Rev. B **68** (2003), 214409–1–214409–8.

[68] G. T. Rado and V. J. Folen, *Observation of the magnetically induced magnetoelectric effect and evidence for ferromagnetic domains*, Phys. Rev. Lett. **7** (1961), 310–311.

[69] H. J. Richter, *Transverse susceptibility measurements of particulate media*, IEEE Trans. Mag. **26** (1990), 1882–1884.

[70] D. S. Rodbell, *Magnetocrystalline anisotropy of single crystal CrO_2*, J. Phys. Soc. Jpn. **21** (1966), 1224–1225.

[71] M. Sasaki, P. E. Jönsson, H. Takayama, and H. Mamiya, *Aging and memory effects in superparamagnets and superspin glasses*, Phys. Rev. B **71** (2005), 104405–1–104405–9.

[72] T. C. Schulthess and W. H. Butler, *Consequences of spin-flop coupling in exchange biased films*, Phys. Rev. Lett. **81** (1998), 4516–4519.

[73] H. Shim, A. Manivannanm, M. S. Seehra, K. M. Reddy, and A. Punnoose, *Effect of interparticle interaction on the magnetic relaxation in NiO nanorods*, J. Appl. Phys. **99** (2006), 08Q503–1–08Q503–3.

[74] S. R. Shinde, R. Ramesh, S. E. Lofland, S. M. Bhagat, S. B. Ogale, R. P. Sharma, and T. Venkatesan, *Effect of lattice mismatch strains on the structural and magnetic properties of barium ferrite films*, J. Appl. Phys. **72** (1998), 3443–3445.

[75] V. Skumryev, S. Stoyanov, Y. Zhang, G. Hadjipanayis, D. Givord, and J. Nogués, *Beating the superparamagnetic limit with exchange bias*, Nature (London) **423** (2003), 850–853.

[76] J. Smit and H. P. J. Wijn, *Ferrites*, John Willey & Sons, 1959.

[77] R. J. Soulen, J. M. Byer, M. S. Osofsky, B. Nadgorny, C. T. Tanaka, J. Nowak, J. S. Moodera, A. Barry, and J. M. Coey, *Measuring the spin polarization of a metal with a superconducting point contact*, Science **282** (1998), 85–88.

[78] L. Spinu, I. Dumitru, A. Stancu, and D. Cimpoesu, *Transverse susceptibility as the low-frequency limit of ferromagnetic resonance*, J. Magn. Magn. Mater. **296** (2006), 1–8.

[79] L. Spinu, H. Srikanth, A. Gupta, X. W. Li, and G. Xiao, *Probing magnetic anistropy effects in epitaxial CrO_2 thin film*, Phys. Rev. B **62** (2000), 8931–8934.

[80] L. Spinu, A. Stancu, Y. Kubota, G. Ju, and D. Weller, *Vectorial mapping of exchange anisotropy in IrMn/FeCo multilayers using the reversible susceptibility tensor*, Phys. Rev. B **68** (2003), 220401–1–220401–4.

[81] L. Spinu, A. Stancu, and C. J. O'Connor, *Micromagnetic study of reversible transverse susceptibility*, Physica B **306** (2001), 221–227.

[82] L. Spinu, A. Stancu, C. J. O'Connor, and H. Srikanth, *Effect of the second-order anisotropy constant on the transverse susceptibility of uniaxial ferromagnets*, Appl. Phys. Lett. **80** (2002), 276–278.

[83] H. Srikanth, J. Wiggins, and H. Rees, *Radio-frequency impedance measurements using a tunnel-diode oscillator technique*, Rev. Sci. Inst. **70** (1999), 3097–3101.

[84] S. Srinath, N. A. Frey, R. Heindl, H. Srikanth, K. Coffey, and N. J. Dudney, *Growth and characterization of sputtered BSTO/BaM multilayers*, J. Appl. Phys. **97** (2005), 10J115–1–10J115–3.

[85] A. Stancu and L. Spinu, *Transverse susceptibility for singe-domain particle with cubic anisotropy*, J. Magn. Magn. Mater. **266** (2003), 200–206.

[86] E. C. Stoner and E. P. Wohlfarth, *A mechanism of magnetic hysteresis in heterogeneous alloys*, Phil. Trans. of the Royal Society of London A: Math. and Phys. Sci. **240** (1948), 599–642.

[87] Y. Sun, M. B. Salamon, K. Garnier, and R. S. Averback, *Memory effects in an interacting magnetic nanoparticle system*, Phys. Rev. Lett. **91** (2003), 167206–1–167204–4.

[88] A. K. Tagantsev, V. O. Sherman, K. F. Astafiev, J. Venkatesh, and N. Setter, *Ferroelectric materials for microwave tunable applications*, J. Electroceramics **11** (2003), 5–66.

[89] K. N. Trohidou, M. Vasilakaki, L. Del Bianco, D. Fiorani, and A. M. Testa, *Exchange bias in a magnetic ordered/disordered nanoparticle system: A Monte Carlo simulation study*, J. Magn. Magn. Mater. **316** (2007), e82–e85.

[90] E. Tronc, D. Fiorani, M Noguès, A. M. Testa, F. Lucari, F. D'Orazio, J. M. Grenèche, W. Wernsdorfer, N. Galvez, C. Chanéac, D. Mailly, and J. P. Jolivet, *Surface effects in noninteracting and interacting γ-Fe_2O_3 nanoparticles*, J. Magn. Magn. Mater. **262** (2003), 6–14.

[91] W. H. von Aulock (ed.), *Handbook of Microwave Ferrite Materials*, Academic Press, 1965.

[92] H. Wang, T. Zhu, K. Zhao, W. N. Wang, C. S. Wang, Y. J. Wang, and W. S. Zhan, *Surface spin glass and exchange bias in Fe_3O_4 nanoparticles compacted under high pressure*, Phys. Rev. B **70** (2004), 092409–1–092409–4.

[93] H. Yu, M. Chen, P. M. Rice, S. X. Wang, R. L. White, and S. Sun, *Dumbbell-like bifunctional Au-Fe_3O_4 nanoparticles*, Nano Letters **5** (2005), 279–382.

[94] R. K. Zheng, H. Gu, B. Xu, and X. X. Zhang, *Memory effects in a nanoparticle system: Low-field magnetization and ac susceptibility measurements*, Phys. Rev. B **72** (2005), 014416–1–0114416–7.

[95] R. K. Zheng, H. Liu, and X. X. Zhang, *Cr_2O_3 surface layer and exchange bias in an acicular CrO_2 particle*, Appl. Phys. Lett. **84** (2004), 702–704.

[96] R. K. Zheng, G. H. Wen, K. K. Fung, and X. X. Zhang, *Training effect of exchange bias in γ-Fe_2O_3 coated Fe nanoparticles* , Phys. Rev. B **69** (2004), 214431–1–214431–4.

APPENDICES

Appendix A List of Publications

Journal Articles

- C. Leighton, D. D. Stauffer, Q. Huang, Y. Ren, B. Toby, M. A. Torija, S. El-Khatib, J.W. Lynn, J. Wu, L. Wang, **N. A. Frey**, H. Srikanth, J. E. Davies, K. Liu, and J.F. Mitchell. *Coupled structural / magnetocrystalline anisotropy transitions in the doped perovskite cobaltite* $Pr_{1-x}Sr_xCoO_3$. Manuscript in preparation.

- M. H. Phan, J. Gass, **N. A. Frey**, H. Srikanth, M. Angst, B. C. Sales, and D. Mandrus. *Enhanced refrigerant capacity in geometrically frustrated* $LuFe_2O_4$ *with multiple phase transitions.* Manuscript in preparation.

- P. Poddar, M. B. Morales, **N. A. Frey**, S. A. Morrison, E. E. Carpenter, and H. Srikanth. *Transverse susceptibility study of the effect of varying dipolar interactions on anisotropy peaks in a 3D assembly of soft ferrite nanoparticles.* Manuscript in preparation.

- M. H. Phan, M. B. Morales, **N. A. Frey**, and H. Srikanth. *Origin of magnetic anomalies in the frozen, mixed and liquid states of ferrofluids.* Submitted, Phys. Rev. Lett.

- S. Srinath, **N. A. Frey**, H. Srikanth, C. Wang, and S. Sun. *Magnetism and surface anisotropy in composite* Au-Fe_3O_4 *nanoparticles.* Submitted, Phys. Rev., B.

- **N. A. Frey**, S. Srinath, H. Srikanth, C. Wang, and S. Sun. *Static and dynamic magnetic properties of composite* Au-Fe_3O_4 *nanoparticles.* IEEE Trans. Mag., **43**, 3094-3096 (2007).

- **N. A. Frey**, S. Srinath, H. Srikanth, M. Varela , S. Pennycook, G. X. Miao, and A. Gupta. *Magnetic anisotropy in epitaxial* CrO_2 *and* CrO_2/Cr_2O_3 *bilayer thin films.* Phys. Rev., B, **74**, 024420-1–024420-8 (2006).

Appendix A (Continued)

- **N. A. Frey**, R. Heindl, S. Srinath, S. Srikanth, and N. J. Dudney, *Microstructure and magnetism in Barium Strontium Titanate (BSTO) - Barium Hexaferrite (BaM) multilayers*, Mat. Res. Bull. **40** (2005), 1286-1293.

- S. Srinath, **N. A. Frey**, R. Heindl, H. Srikanth, K. R. Coffey, and N. J. Dudney, *Growth and characterization of sputtered BSTO/BaM multilayers*, J. Appl. Phys. **97** (2005), 1-3.

- J. L. Wilson, P. Poddar, **N. A. Frey**, H. Srikanth, K. Mohomed, J. P. Harmon, S. Kotha, and J. Wachsmuth. *Synthesis and magnetic properties of polymer nanocomposites with embedded iron nanoparticles.* J. of App. Phys., **95**, 1439-1443 (2004).

- L. L. R. Williams and **N. Frey**. *Angular Distribution of Gamma-ray Bursts and Weak Lensing.* Astrophys. Jour., **583**, 594-605 (2003).

Conference Proceedings

- **N. A. Frey**, M. B. Morales, H. Srikanth, and S. Srinath. *Transverse susceptibility as a probe of interface magnetism in functional multilayers and nanostructures.* Encyclopedia of Advanced Materials: Science and Engineering (Pan Stanford Publishers, in press 2008).

- J.Gass, **N. A. Frey**, M. B. Morales, M. J. Miner, S. Srinath, and H. Srikanth. *Magnetic anisotropy and magnetocaloric effect (MCE) in $NiFe_2O_4$ nanoparticles.* Materials Research Society Symposium Proceedings, **962**, 0962-P05-03 (2007).

- S. Srinath, **N. A. Frey**, H. Srikanth, G. X. Miao, and A. Gupta. *Magnetic anisotropy and exchange coupling in epitaxial CrO_2 and CrO_2/Cr_2O_3 bilayer thin films.* Proceedings of DAE Solid State Symposium (2006).

Appendix A (Continued)

- S. Srinath, **N. A. Frey**, H. Srikanth, G. X. Miao, and A. Gupta. *Exchange Bias in CrO_2/Cr_2O_3 bilayer thin films.* Advances in Science and Technology, **45**, 2528 (2006).

Appendix B List of Conference Presentations

Conference Presentations

- **N. A. Frey**, H. Srikanth, D. D. Stauffer, and C. Leighton. *Magnetic anisotropy and switching in $Pr_{0.5}Sr_{0.5}CoO_3$ using RF transverse susceptibility.* Session B23.10, American Physical Society March Meeting, New Orleans, LA. (2008)

- **N. Frey-Huls**, H. Srikanth, D.D. Stauffer, and C. Leighton. *Unusual magnetic anisotropy and switching in $Pr_{0.5}Sr_{0.5}CoO_3$ probed by RF transverse susceptibility.* Session FR-01, 52nd Magnetism and Magnetic Materials Conference, Tampa, FL. (2007)

- **N. A. Frey**, S. Srinath, H. Srikanth, C. Wang, and S. Sun. *Static and dynamic magnetic properties of "dumbbell" and "flower" shaped Au-Fe_3O_4 nanoparticles.* Session P14.12 American Physical Society March Meeting, Denver, CO. (2007)

- **N. A. Frey**, S. Srinath, H. Srikanth, C. Wang, and S. Sun. *Static and dynamic magnetic properties of "dumbbell" and "flower" shaped Au-Fe_3O_4 nanoparticles.* Session BB-05. 10th Joint Magnetism and Magnetic Materials/Intermag Conference, Baltimore, MD. (2007)

- S. Srinath, **N. A. Frey**, H. Srikanth, G. X. Miao, and A. Gupta. *Magnetic anisotropy and exchange bias in epitaxial CrO_2/Cr_2O_3 bilayer thin films.* Session CP-13 10th Joint Magnetism and Magnetic Materials/Intermag Conference, Baltimore, MD. (2007)

- **N. A. Frey**, S. Srinath, H. Srikanth, G. X. Miao, and A. Gupta. *Magnetic anisotropy in CrO_2 and CrO_2/Cr_2O_3 bilayer thin films.* Session Y22.10 American Physical Society March Meeting, Baltimore, MD. (2006)

- **N. A. Frey**, R. Heindl, S. Srinath, H. Srikanth, K. R. Coffey, and N. J. Dudney. *Growth and Characterization of tunable BSTO/BaM multilayers as substrates for*

magnetic nanoparticles. Session S42.6 American Physical Society March Meeting, Los Angeles, CA. (2005)

- **N. A. Frey**, H. Hajndl, P. Poddar, H. Srikanth, and N. J. Dudney. *Growth and characterization of BSTO/Barium Hexaferrite multilayered films as tunable substrates for nanoparticles.* Session N23.12 American Physical Society March Meeting Montreal, Quebec, Canada. (2004)

Contributed Conference Presentations

- M. B. Morales, P. Poddar, **N. A. Frey**, H. Srikanth, S. A. Morrison, and E. E. Carpenter. *Probing the effect of interparticle interactions in ferrite nanoparticles using the reversible transverse susceptibility method.* Session D27.7 American Physical Society March Meeting, New Orleans, LA. (2008)

- H. Srikanth, **N. Frey-Huls**, C. Vasani, and J. Sanatamaria. *Magnetic anisotropy and vortex dynamics in LCMO/YBCO heterostructures.* Session ED-10 52nd Magnetism and Magnetic Materials Conference, Tampa, FL. (2007)

- H. Srikanth, **N. A. Frey**, C. Visani, and J. Santamaria. *Magnetic anisotropy and vortex dynamics in LCMO/YBCO heterostructures.* Session L13.5 American Physical Society March Meeting, Denver, CO. (2007)

- J. Gass, M. B. Morales, **N. A. Frey**, M. J. Miner, S. Srinath, and H. Srikanth. *Magnetocaloric effect (MCE) in Nickel Ferrite nanoparticles.* Session W14.8 American Physical Society March Meeting, Denver, CO. (2007)

- S. L. Morrow, **N. A. Frey**, S. Srinath, and H. Srikanth. *Synthesis of Barium Hexaferrite nanoparticles for functional multilayers.* Session W22.6 American Physical Society March Meeting, Baltimore, MD. (2006)

Appendix B (Continued)

- R. Hajndl, S. Srinath, **N. A. Frey**, H. Srikanth, S. Balachandran, and T. Weller. *Growth and Characterization of BSTO/Barium hexaferrite multilayers.* International Conference on Ferroelectrics, San Francisco, CA. (2004)

- S. Srinath, **N. A. Frey**, R. Hajndl, H. Srikanth, K. R. Coffey, and N. J. Dudney. *Growth of electrically and magnetically tunable BSTO/BaF multilayers.* 49th Magnetism and Magnetic Materials Conference Jacksonville, FL. (2004)

- **N. Frey**, R. Hajndl, P. Poddar, and H. Srikanth. *Microstructure and magnetism in BSTO/hexaferrite composite films.* 2nd International Conference on Materials for Advanced Technologies & IUMRS, Singapore. (2003)

ABOUT THE AUTHOR

Natalie Frey was born and raised in Minneapolis, Minnesota. She attended the University of Minnesota as an undergraduate where she double majored in physics and astrophysics. She joined the University of South Florida Physics Department in the fall of 2002 and the Functional Materials Laboratory the following spring. Besides her time spent doing research at USF she has spent two summers away as a visiting student. In 2003 she was the recipient of a SURA fellowship which brought her to Oak Ridge National Laboratory in Knoxville, Tennessee. In the summer of 2007, she was an intern in the Recording Systems Operations Group at Seagate Technologies in her hometown of Minneapolis. She has published several scientific papers on a wide range of magnetic systems focusing mainly on the use of transverse susceptibility to measure magnetic anisotropy. In 2006 she was awarded the NSF IGERT fellowship and has since broadened her research to include tuning the magnetic properties of nanoparticles for drug delivery and hyperthermia. She currently resides in Tampa with her husband, Dean and their three cats.